Universal wave phenomena in multiple scattering media

Universal wave phenomena in multiple scattering media

ACADEMISCH PROEFSCHRIFT

ter verkrijging van de graad van doctor
aan de Universiteit van Amsterdam
op gezag van de Rector Magnificus
prof. dr. D. C. van den Boom
ten overstaan van een door het college voor promoties
ingestelde commissie,
in het openbaar te verdedigen in de Agnietenkapel
op vrijdag 16 september 2011, te 12.00 uur

door

Sanli Ebrahimi Pour Faez

geboren te Teheran, Iran

Promotiecommissie

Promotor:	Prof. Dr. A. Lagendijk
Overige Leden:	Prof. Dr. V.E. Kravtsov Prof. Dr. B.A. van Tiggelen Prof. Dr. M.S. Golden Prof. Dr. K. Schoutens Dr. A.P. Mosk

Faculteit der Natuurwetenschappen, Wiskunde en Informatica

The work described in this thesis is part of the research program of the
“Stichting Fundamenteel Onderzoek der Materie (FOM)”
which is financially supported by the
“Nederlandse Organisatie voor Wetenschappelijk Onderzoek (NWO)”.

This work was carried out at the
Center for Nanophotonics, FOM Institute for Atomic and Molecular Physics AMOLF
Science Park 104, 1098XG Amsterdam, The Netherlands
where a limited number of copies of this dissertation is available.

Printed by: Ipskamp Drukkers, Enschede, The Netherlands (2011)
ISBN/EAN: 978-94-91211-79-9

to Bahar
my compassionate twin soul

and
to the future of Soline

Paranimfen: Ramy El-Dardiry and Timmo van der Beek
Cover: Hitchhikers' guide to the light cage, by Telli and Sanli Faez

The scientist is not a person who gives the right answers
he is one who asks the right questions.

Claude Lévi-Strauss

Contents

1 Introduction to waves in disordered media **1**
- 1.1 Why should we study disorder? . . . 1
- 1.2 Waves and scattering . . . 2
- 1.3 Anderson localization phase transition . . . 3
  - 1.3.1 Self-consistent theory . . . 4
  - 1.3.2 Random matrices . . . 4
  - 1.3.3 The critical state and its statistics . . . 5
  - 1.3.4 Fragmented research on a universal phenomenon . . . 6
- 1.4 Overview of this dissertation . . . 7

2 Multiple-scattering theory **9**
- 2.1 Building blocks . . . 9
  - 2.1.1 Wave equations . . . 10
  - 2.1.2 The t-matrix . . . 11
  - 2.1.3 Average Green function in the multiple scattering regime . . . 13
  - 2.1.4 Diffusion approximation . . . 14
- 2.2 Mesoscopic intensity correlations . . . 15
  - 2.2.1 Average amplitude correlator . . . 16
  - 2.2.2 Short-range intensity correlations . . . 18
  - 2.2.3 Non-universal C_0 correlations . . . 18
- 2.3 Nonlinear random media . . . 19
  - 2.3.1 Second-harmonic t-matrix . . . 21
  - 2.3.2 Diffusion approximation for the second-harmonic generation . . . 23
  - 2.3.3 Derivation of the C_0 vertex . . . 23

3 Random-matrix theory **25**
- 3.1 A short history of RMT . . . 25
- 3.2 Wigner-Dyson ensembles . . . 26
  - 3.2.1 Hamiltonians . . . 27
  - 3.2.2 Scattering matrices . . . 28
- 3.3 Unconventional ensembles . . . 28
  - 3.3.1 Banded matrices . . . 29

3.3.2 Complex-symmetric matrices . . . 31
3.4 Statistical probes in simulations and experiments . . . 31
3.4.1 Level-spacing distribution . . . 32
3.4.2 Open transmission channels . . . 33
3.4.3 Anderson localization in waveguide geometry . . . 34
3.4.4 Eigenfuntion statistics and Anderson localization . . . 36
3.5 Perturbation results for almost-diagonal Green matrices . . . 38
3.6 Concluding remarks . . . 41

4 Dipole chain **43**
4.1 The model . . . 44
4.1.1 Dipole chain model . . . 45
4.1.2 Resonant point scatterer . . . 46
4.1.3 Dimensionless formulation . . . 46
4.1.4 Hypothetic models . . . 47
4.2 Analytical probes . . . 47
4.2.1 Perturbation results for the weak-coupling regime . . . 48
4.3 Numerical results . . . 49
4.3.1 Spectrum of the homogeneous chain . . . 49
4.3.2 The effect of disorder . . . 50
4.3.3 Scaling behavior of PDF . . . 52
4.3.4 Multifractal analysis . . . 56
4.3.5 The singularity spectrum . . . 57
4.4 Summary and conclusion . . . 58

5 Multifractal ultrasound waves **61**
5.1 The experiment . . . 62
5.2 Scaling analysis . . . 62
5.3 Discussion . . . 64
5.3.1 Deviation from numerical results . . . 65
5.3.2 Final remarks . . . 65

6 Refractive index tuning **67**
6.1 Theoretical principles . . . 68
6.2 Samples . . . 69
6.3 Setup and measurements . . . 70
6.4 Results and discussion . . . 71
6.4.1 Diffusion constant of porous plastic . . . 71
6.4.2 Comparison with the time-resolved method . . . 72
6.4.3 Tuning response of a photonic crystal . . . 73
6.5 A test for effective-medium theories . . . 74
6.6 Further applications . . . 76
6.7 Conclusions . . . 76

7 Diffuse nonlinear interference **77**
7.1 Two classes of nonlinear random media . . . 78
7.2 Two-beam experiment . . . 79
7.2.1 Underlying theory . . . 79

7.2.2 Beyond the scalar approximation 80
7.3 Experimental settings 81
7.4 Results and discussion 82
7.4.1 Dependence on scattering strength 83
7.4.2 C_X measurement in a single shot 84
7.4.3 Applicability of the scalar model 85
7.5 Final remarks 87

Afterword **89**

Summary **94**

Samenvatting (Dutch summary) **97**

Bibliography **99**

CHAPTER 1

Introduction to waves in disordered media

> *"Only the uninitiated will be misled by the use of word "ill" to arrive at the possibly pejorative conclusions, especially as the use of such disparaging words (disorder, defects, amorphous, instabilities, noise, etc.) is rampant in the subject. However, since Galileo's discovery of the sunspots (malculae), much to the irritation of his contemporaries, scientists have revelled in their efforts to overcome prejudice, and this even in their choice of words."*
>
> preface to *ill-condensed matter*[1]

1.1 Why should we study disorder?

Studying the influence of disorder on the properties of many-body systems is perhaps as old as statistical physics itself. However, the title "disordered systems" is mostly attributed to the study of the collective behavior in a *randomly* arranged bunch of atoms and molecules in the condensed phase, in contrast to their crystalization. In the 1970's and 80's, "condensed-matter" physics, a term allegedly coined by Philip Anderson, won the race of attracting brains and funds overtaking the traditional stronghold of particle physics. Since the beginning, disorder has been a central subject in studying complex systems and constantly new applications in other emerging fields have been found. Major subjects of computer science, protein folding, neural networks, and evolutionary modeling are just a few examples, that have benefited from the formalism introduced by condensed-matter physicists to study disorder.

One can motivate the study of disorder by the mere fact of its omnipresence in artificial as well as natural structures. So to say, the physics of a system is only understood after one clearly describes the role of imperfections. This argument, however, may be refuted

---

[1] Lecture notes, Session XXXI of the Les Houches summer school, Edited by Roger Balian, Roger Maynard, and Gerard Toulouse, North-Holland / World Scientific (1979)

by those who believe that technology will at the end make it possible to make perfect structures.

Researchers of complex systems have discovered several physical phenomena that are solely present in disordered systems. Turbulence, emergence of chaos in dynamic systems, and disorder-induced phase transitions are just a few examples. Breakthroughs in describing natural, sociological and econometric mechanisms have been achieved after they were formulated in the language of physics for complex systems. Therefore, studying disorder can be interesting for its own sake. That is why we see, more and more, that researchers deliberately introduce "designed" disorder into their model systems to study there fundamental aspects.

1.2 Waves and scattering

Another fundamental and omnipresent subject in physics is the study of waves. Five of the seventeen iconic equations of physics[2] are related to a form of wave equation. Among these, the Schrödinger equation and the electromagnetic wave equation are perhaps the most prominent. This common aspect has resulted in the discovery of several analogies between classical and matter waves. It has also inspired the design of new systems and invention of new technologies. Photonics is one of these field that has initially emerged to bypass the shortcomings of semiconductor electronics in communication technologies but has later found important application of its own. Photonics is mainly governed by the Maxwell equations, but has become the ground to demonstrate the analogous to several quantum phenomena discovered in condensed matter physics, which were first formulated by using the Schrödinger equation.

It has been a long tradition in optics, and was inherited by photonics, to formulate the propagation of waves in terms of scattering and Green functions. This is perhaps because light is hardly ever bound, as opposed to other charge carriers. Light propagation in complex photonic structures can be described by a summation over many multiple-scattering processes. Colloidal particles in a suspension and Bragg planes in a three dimensional photonic crystals are two different but well-known examples of scattering entities. Photonic metamaterials can also be described as multiple-scattering systems in which the size and spacing between scatterers is much less than a wavelength. In biological applications, "turbid medium" is widely-encountered expression that refers to multiple scattering samples such as muscles, bones and skin or brain tissue.

What is less appreciated is the strength of using the scattering language for describing "plain" effects light propagation in homogeneous media, refraction, or absorption. With the miniaturization of photonic structures, which brings the typical length scales of the physical structure closer to or even smaller than the wavelength, the wave nature becomes more pronounced. The scattering formalism is much stronger in considering all the wave aspects. Formulating in the scattering language has inspired the discovery of phenomena that have been overlooked in the homogenized effective medium picture [137, 139].

Coming partly from the engineering tradition, photonics scientists resort to finite-element numerical methods to find system-specific solutions they need for a better design or understanding of their observations. As quoted from Sir Nevill Mott, when shown some computer simulation results on metallic conductivity, it is good to know that the computer

---

[2] As collected by Sander Bais in *The Equations, Icons of Knowledge*

understands the solutions but we scientists should also try to understand them. In this respect, the scattering theory can often provide accurate models for photonic phenomena with affordable analytical effort. In such a modelling, the concept of point-scatterer is certainly one of the most valuable assets available [36]. By piling up several point scatterers, one can simulate various ordered or random structures [27, 70]. This is the path we will follow in chapter 4 to model one of the most intriguing wave phenomena in complex media: Anderson localization.

1.3 Anderson localization phase transition

Anderson localization refers to the suppression of wave diffusion in random media due to interference effects. This conductor to insulator transition is named after Philip Anderson who predicted this phenomenon in his seminal theoretical paper: "Absence of Diffusion in Certain Random Lattices" back in 1957 [7]. Anderson was inspired by experiments performed in George Fehers group at Bell Labs [8]. Those experiments showed anomalously long relaxation times of electron spins in doped semiconductors, and meant that electrons where interacting less than expected with their surrounding. Anderson looked into this problem from the perspective of electric conductivity of metals. Later it was understood that Anderson localization is a general wave phenomenon that applies to the transport of electromagnetic waves, acoustic waves, Schrödinger waves and spin waves [76]. Very recently, it has been exhibited also in Bose-Einstein condensates [11].

Little was understood about the origin of localization in the first twenty years of its discovery. 1979 marked important breakthroughs: the scaling theories of localization was suggested by the gang of four (Abrahams, Anderson, Licciardello, and Ramakrishnan) [1], admittedly based on the ideas of Thouless, and in the same year by Oppermann and Wegner [101]. The mapping onto the nonlinear sigma model was conjectured by Efetov, Larkin, and Khmel'nitskii [68]. Götze, Vollhardt and Wölfle [59, 138] presented the self-consistent approximation. At the same time a numerical renormalization scheme by MacKinnon and Kramer [82] initiated a wave of computer simulations, which has provided most of the quantitative result on localization up to this day.

By then, it was realized by the condensed-matter physicists that Anderson localization is a true quantum phase transition with a lower critical dimension of two (for the conventional single particle model). In one- and two-dimensional disordered scattering potentials the states are always localized. Yet for a finite sample the localization length can be much larger than the system size, in which case the states appear to be extended and the conductance does not vanish. The localization length decreases at higher strength of randomness. In three dimensions, a critical point exists when crossing from the extended to the localized regime at a certain strength of disorder. A crude estimate for this threshold is given by the Ioffe-Regel criterion: when the mean free path equals a fraction of the wavelength. Decades after those breakthroughs, an analytical theory for localization transition in 3-d is still lacking. So is a conclusive experimental observation that can provide a value for the critical exponents. Just recently, considerable advances have been performed on the equivalent system of kicked rotors, which shows a localization transition in the momentum space [30, 78].

The year 2008 marked the 50th anniversary of the Anderson's celebrated paper, with several workshops and symposia dedicated to the topic. These activities resulted in the publication of a few special editions reviewing most of the historical and contemporary contributions to the study of this fascinating phenomenon.

1.3.1 Self-consistent theory

Despite the elegance of the Anderson's early prediction, experimental observation of localization in 3-d is still limited to a few cases. The omnipresence of electron-electron interactions makes it difficult to compare the experimental results for electronic systems with single-particle models. Repulsive interactions lead to another kind of a localization, called Mott localization. Most of the understanding of Anderson localization is thus made from the advances on the theoretical side, and more lately by performing computer simulations.

The self-consistent theory of localization is the most favorable theory for the experimentalist that often approach localization transition starting from the diffusive side. This theory starts with the diagramatic formalism developed for describing diffusion and then includes the interference effects to an extent that the classical diffusion breaks down. It has proven to be very successful in covering most of experimental transport measurements, even in a regime where the approximations are pushed to their limits [64, 78].

Interference effects can already be observed in system with weaker scattering strength than the Ioffe-Regel limit. This is called weak localization. Some people see it as a precursor effect to Anderson localization. However, in consideration of the critical aspects of localization transition, this connection is a bit loosely justified[3]. The introduction of self-consistent theory and the 1985 observation of the weak localization of light, set the stage for a search for Anderson localization using classical waves such as light and sound. Sajeev John predicted the existence of a frequency regime in which electromagnetic waves are fully localized [66].

Classical waves offer certain advantages for studying localization. Unlike electrons, photons do not interact with each other, and their coherence time is much longer typical experimental time-scales. For light, frequency takes over the role of electron energy. Finding structures with high-enough index contrast (disorder parameter) that shows localization at a desirable frequency (where light is not absorbed by the bulk of the material) has become a challenge. The self-consistent theory has successfully described the time-dependent diffusion observed with microwaves, light, ultrasound, and in kicked rotors. However, it stays short of describing the full statistics at the critical point and can not provide much information about the localized phase.

1.3.2 Random matrices

Another approach to studying waves in disordered media is to see the whole system as a matrix. This matrix can either be the Hamiltonian or the scattering matrix. For a disordered system, the entries of this matrix look like random. One can imagine that the statistical properties will not change if the entries are taken as truly random. This is the main concept behind random matrix theory (RMT). In contrast to the multiple-scattering formalism, which can be seen as the reductionist approach to studying waves in disordered media, random matrix theory is a holistic approach. In a RMT treatment, one often overlooks all the details of the system under investigation. Despite the apparently loose justification of RMT basic assumptions, the predictions are often generally applicable and

---

[3] In the same sense, liquid water is different from ice no matter how cold the water is above the melting point.

surprisingly successful in reproducing the experimental results, even for very complicated systems.

A major advancement was due to the work of Efetov [41], influenced by some earlier ideas of Wegner. He showed how to approximately map the problem of calculating disorder averages of products of amplitude Green functions for a single particle in a random potential on a supersymmetric nonlinear σ-model. The same nonlinear σ-models can be used to describe the conventional random matrix ensembles in the limit of large matrix sizes. By developing this formalism, he made a major step in relating RMT to the microscopic description of disorder. Efetov's method have since been applied to several transport problems and motivated condensed matter and high energy physicists to study each others calculations. This unprecedented proximity has lead to the solution of several long-standing problems that were outside the range of all previous methods.

Despite its generality and overlooking microscopic details, RMT has been influential in providing a digestible picture of localization. In a very recent opinion piece [8], Philip Anderson writes:

> "*... in the end I came to believe that the real nature of the localization phenomenon could be understood, by me at least, by Landauer's formula...*
> *But what might be of modern interest is the "channel" concept, which is so important in localization theory.*"

The Landauer's formula connects the conductance with the trace of the transmission matrix. The channels are simply the eigenvectors of this matrix. RMT simply provides the most straightforward description of transmission matrices for disordered structures. Just very recently, classical wave experiments have provided astonishing experimental evidence for the existence and recognition of these channels and the capacity of controlling them in parallel [136, 140].

1.3.3 The critical state and its statistics

An attractive aspect of performing experiments with light (at room temperature!) is in its visuality. One may start wondering how does a localizing sample look like? Is it sparkling like a photonic crystal or dark like soot? Such a picture of light localization has not been taken yet, but two recent experiments on have provided unprecedented hint. The first experiment was on ultrasound propagation in a collection of metallic beads [47, 64] and the second one on mapping the electronic wavefunction in 2-d electron gas using a scanning tunneling microscope [106].

Both experiments have succeeded in visualizing an amazing property of waves in the proximity of the Anderson transition. This universal phenomenon is described by multifractality, which can be pictured as a wildly fluctuating forked intensity-patterns close to the localization transition. This property was predicted in 1980 by Franz Wegner [142] and was boosted again in recent years due to more recent theoretical developments [43]. Chapter 5 of this dissertation is dedicated to the first observation of this phenomenon with ultrasound waves.

These observations are perhaps the closest one has ever get to the observation of critical states of the Anderson transition. Unfortunately they stay short of providing a clear picture of what happens exactly at the transition point. This deficiency is due to the finite size of the sample and yet unidentified transition threshold. Several questions are yet to be answered, but the venue has just opened for the observation of fascinating phenomena attributed to disorder-induced localization of waves.

1.3.4 Fragmented research on a universal phenomenon

Before finishing this introductory chapter, it is worth spending a few line on the social aspects of the research connected to the topic of this thesis. Physicists do their job, exploring the unknown, with different approaches. Theoreticians like to start from basic principles and make new predictions or describe the phenomena observed in nature. Experimentalist, enthusiastic about observing new phenomena, like to apply those theories and formulate their observations. In this respect, one expects that theoreticians and experimentalists are very much interested in each others' findings and seek a lot of interaction among themselves. But in reality, the scientific world is divided into several small communities separated by thick and tall, implicit or evident, walls. Each person who goes for a scientific career is pushed to select one of the communities and interact, compete and collaborate only with them, perhaps for many years. Sometimes they even do not realize the existence of other communities that work on the same subject from an slightly different perspective. This separation is often reflected in the creation of distinct sets of jargon and notation for identical concepts; scientists from different fields call different names to exactly the same quantities.

If some day, the scientific topics in physics are sorted by the number of separate communities that work on it, Anderson localization will appear somewhere on the top of that list. It is a fact that scientific research is getting more and more instrument-intensive and application-oriented. Meanwhile, research fields are getting more and more specialized and nobody can master a broad range in science, like it was possible at the 19th century for Rayleigh and Maxwell. It does not mean that scientists should communicate less and hide in their comfort zones. The main fascination of studying physics is still in being able to discover the truth in the nature. The key point is to be open to learn from others and avoid prejudice, even (and specifically) prejudice on your own findings.

Over the past fifty years, Anderson localization has attracted interest far outside its original scope of definition: as far as seismology and biomedical imaging. Most of the theoretical developments on the understanding of this phenomenon have been made by the condensed-matter physicists. Many important experimental achievement, however, have been provided by the research on classical waves. The communication between the two communities, however, have fallen extremely short of adequate. Unfortunately, some existing interpretations of Anderson localization, as reported next to experimental results, have been very mystified and sometimes superficial. Several claims have been made related to the observation of localization phenomena based on inadequate evidence or sometimes erroneous comprehension of the physics behind it. As a mild, but quite clear, indication to this discontent, Philip Anderson told the author in a workshop in Cambridge: "People from the classical wave community often make strong claims based on little evidence."

These strong and wrong claims, which have been made in more than one occasion, have been perhaps one of reasons that the much needed collaboration between the abovementioned communities is still weak. With all the recent theoretical and experimental developments in understanding localization, and all the expectable advanced ahead of us, it is perhaps a good time to provide a unified and demystified picture of this intriguing universal wave phenomenon.

1.4 Overview of this dissertation

Rather than reporting the successful achievement of one or more well-defined goals, that should be awarded by a doctorate degree, this text is a progress report by the author over his efforts to understand the goal. The original goal was to experimentally observe Anderson localization of visible light. This has not been achieved. The efforts that have been made to firstly uncover the suitable observables and secondly realize the experiments, have bore fruit in discovery of new methods, formation of rewarding collaborations, and unveiling valuable information hidden in the experiments performed by others.

The next two chapters are dedicated to introducing the basic foundations of multiple-scattering (chapter 2) and random matrix (chapter 3) theories. Books have been written about these subjects, and there is neither the intention nor the capacity of presenting a thorough introduction. Chapter 2 helps the reader to follow the derivation of two new theoretical results that are performed by us by using a multiple scattering approach and reported here. The first result is the equivalence of variations in frequency with variation in effective refractive index. This equivalence sets the basis for the method of Refractive Index Tuning, which is described in chapter 6 and supported by experimental results. The second theoretical result is the relation between so-called C_0 fluctuations and the efficiency of second harmonic generation in random media. This equivalence was the motivation behind the experiment that will be described in chapter 7. Both experiment were actually designed with the idea of analyzing samples in the localized regime, but the samples never became to existence.

In chapter 4, the intensity distribution of electromagnetic polar waves in a chain of near-resonant weakly-coupled scatterers is investigated theoretically and supported by numerical analysis. Critical scaling behavior is discovered for part of the eigenvalue spectrum due to the disorder-induced Anderson transition. This localization transition (in a formally one-dimensional system) is attributed to the long-range dipole-dipole interaction, which decays inverse linearly with distance for polarization perpendicular to the chain. For polarization parallel to the chain, with inverse-squared long-range coupling, all eigenmodes are shown to be localized. A comparison with the results for Hermitian power-law banded random matrices and other intermediate models is presented. This comparison reveals the significance of non-Hermiticity of the model and the periodic modulation of the coupling

The experimental observation of strong multifractality in wave functions close to the Anderson localization transition in open three-dimensional elastic networks is reported in chapter 5. The experimental observation of localization in these samples were reported in a prior publication [64]. Our second look at the measurements provided the first experimental indication of multifractal structure of waves near the localization threshold and confirmed the nontrivial symmetry of the multifractal exponents.

CHAPTER 2

Multiple-scattering theory of linear and nonlinear random media

The main purpose of presenting this chapter is to provide the necessary basic knowledge of the theory of multiple scattering. This brief introduction will help the reader to follow the derivation of two new theoretical results that are performed by us by using a multiple scattering approach and reported in this thesis. The first result is the equivalence of variations in frequency with variation in effective refractive index. This equivalence sets the basis for the method of Refractive Index Tuning, which will be described in chapter 6 in more details and alongside experimental results. The second theoretical result is the relation between so-called C_0 fluctuations and the efficiency of second harmonic generation in random media. This equivalence was the motivation behind the experiment that will be described in chapter 7.

The theory of multiple scattering has been extensively developed in the last seventy years. We do not have the intention, nor the capacity, to re-derive all the details. What presented here is just an attempt to introduce our notation in a logical way, and meanwhile lay down the basic information needed for understanding the theoretical and experimental results presented in this dissertation. Therefore, we have formulated most of our calculations for the simplest geometry and with minimal details. As long as these aspects do not fundamentally change the physical outcome, for example the discussion on boundary conditions or limitations of our simple approximation, they are skipped.

2.1 Building blocks

Multiple scattering formalism is the reductionist approach to studying transport of waves in a disordered medium. In this formalism, one needs to first divide the medium into the smallest relevant blocks and write down a microscopic theory for the interaction of wave and these material blocks. These are called scatterers and the the interaction is simply called scattering. The scattering can sometimes be linked to the fluctuations in density, which is usually formulated in the momentum coordinates. Thus, an scattering event is not necessarily local. The second step is to describe the propagation of waves between successive scattering events. The concept of effective medium emerges while taking this step. Unlike the collision between billiard balls, the propagation of waves are influenced by scatterers outside, as well as inside, their geometrical extent. Therefore, the propagation of waves nearby a collection of scatterers is not the same as in vacuum, even if the scatterers are not densely packed. This effect is generally known as diffraction. However, in a simplified picture, one can usually use effective medium parameters for certain length scales. Describing sound propagation in a rock (full of fractures) or light propagation in liquid water (a collection of water molecules) by only attributing a reduced value to the wave velocity is based on a similar effective medium approach.

The third, and often the most challenging, step for description of wave propagation in a multiple scattering environment is to distinguish the relevant observables and perform the proper averaging. Like many other many-body systems, this averaging is essential for providing a decent theoretical prediction, which can be used for explaining experimental results. Without proper averaging, one has to generate as many models as there are realizations of disorder. Whether or not the experimental data should also be averaged over several realizations depends on the specific transport quantity that needs to be measured. In the theoretical treatment of transport, however, some degree of averaging over realizations is always required.

The three steps mentioned above are usually sufficient to describe the wave propagation in bulk heterogeneous media. In presence of interfaces, which is unavoidable for any realistic experimental setting, further efforts should be made to properly incorporate the boundary effects.

2.1.1 Wave equations

In general, electromagnetic fields or elastic deformations have vectorial character. However, to be able to understand the underlying physics before sinking in the often intractable zoo of dyadic and tensorial equations, one can start with the scalar field approximation. In many cases, nature is nice to us and this approximation is sufficient for describing the observations. However, one shall be always careful with using scalar equations to simplify vectorial fields, since some phenomena can simply be overlooked. We shall discuss one such case in chapter 7. Some physical quantities like birefringence and depolarization do not fit into the scalar field picture, unless a clever treatment is employed [69].

In this chapter, we limit our discussions to the properties of scalar waves. The classical scalar wave equation in an inhomogeneous medium is

$$\nabla^2\psi(\mathbf{r},t) - \frac{\varepsilon(\mathbf{r})}{c^2}\frac{\partial^2\psi(\mathbf{r},t)}{\partial t^2} = j(\mathbf{r},t), \tag{2.1}$$

with c the speed of propagation in vacuum and $j(\mathbf{r},t)$ describing the distribution of sources or sinks. On mapping to the Maxwell equations, ψ usually represents the electric field. For this mapping to be correct, one has to consider slowly varying permittivity and permeability on the scale of wavelength, else other terms related to their derivatives should be included. In acoustics it is the local compression. The scalar wave equation can describe several types of waves with proper mapping of the oscillating fields and material parameters. In the rest of this chapter, for simplicity, we use the terminology of electromagnetic waves and light in specific. Most of the results presented here are generic to other types of classical waves, and in many cases even hold for quantum wavefunctions, which are answers to the Schrödinger equation.

The disorder in the medium is encoded in $\varepsilon(\mathbf{r})$, which represents the dielectric constant for the case of electromagnetic waves. The time dependence of the classical wave equation (2.1) can be separated by assuming monochromatic waves $\psi(\mathbf{r},t) = \mathrm{Re}\left[\psi(\mathbf{r})e^{\imath\omega t}\right]$, where ω is the internal frequency. For a single harmonic point source of strength j_0 located at origin, the wave equation is reduced to the following inhomogeneous Helmholtz equation:

$$-\nabla^2\psi(\mathbf{r}) - V(\mathbf{r})\psi(\mathbf{r}) \quad = \quad \frac{\omega^2}{c^2}\psi(\mathbf{r}) - j_0\delta(\mathbf{r}), \tag{2.2}$$

with $V(\mathbf{r}) = \frac{\omega^2}{c^2}[\varepsilon(\mathbf{r})-1]$. The equation is written in this form to emphasize the resemblance with the Schrödinger equation for a single particle (for example electron) in a disordered potential:

$$-\frac{\hbar^2}{2m}\nabla^2\psi(\mathbf{r}) - V(\mathbf{r})\psi(\mathbf{r}) \quad = \quad E\psi(\mathbf{r}). \tag{2.3}$$

Note that the scattering potential for light depends on the frequency of the wave. This dependence is absent in the non-relativistic Schrödinger equation. Furthermore, electrons are hardly created inside an electronic system, but rather injected into the system through an electrode.

Green function in vacuum

In absence of the disorder potential, the solution to Eq. (2.2) for a unit source $j_0 = 1$ is the free space propagator or Green function $g_0(\mathbf{r})$. This solution is found by a Fourier transform to the momentum space,

$$\int e^{\imath\mathbf{p}\cdot\mathbf{r}}\left(\nabla^2 g_0(\mathbf{r}) - \frac{\omega^2}{c^2}g_0(\mathbf{r}) - \delta(\mathbf{r})\right)d\mathbf{r} = 0, \tag{2.4}$$

which results in

$$g_0(\mathbf{p}) = \frac{1}{\frac{\omega^2}{c^2} - p^2 + \imath 0}. \tag{2.5}$$

The small imaginary term in the denominator is put for the convergence of the inverse Fourier tranform. Transforming back to the position coordinates reads,

$$g_0(\mathbf{r}) = -\frac{e^{\imath\frac{\omega}{c}r}}{4\pi r}, \tag{2.6}$$

with $r = |\mathbf{r}|$. Note that the Green function is in general dependent on the frequency, but we have dropped the index since we are considering only monochromatic waves.

2.1.2 The t-matrix

Having the free space propagator in hand, one can write an iterating solution for the wave function in presence of one scatterer,

$$\psi(\mathbf{r}) = \psi_0(\mathbf{r}) + \int g_0(\mathbf{r}-\mathbf{x})V_i(\mathbf{x})\psi(\mathbf{x})d\mathbf{x}, \tag{2.7}$$

where $\psi_0(\mathbf{r})$ is a homogeneous solution to the Helmholtz equation (2.2) and $V_i(\mathbf{x})$ is the potential of the scatterer with index i. Iteration of Eq. (2.7) gives an explicit sum of scattering events. Each term in the series represents a higher-order scattering contribution of the same scatterer. This summation allows for the inhomogeneous wave function to be written as an integral of the homogeneous solution. The solution can be written as,

$$\psi(\mathbf{r}) = \psi_0(\mathbf{r}) + \int g_0(\mathbf{r} - \mathbf{x}_1) t_i(\mathbf{x}_1, \mathbf{x}_2) \psi_0(\mathbf{x}_2) d\mathbf{x}_1 d\mathbf{x}_2, \tag{2.8}$$

with the scattering matrix $t_i(\mathbf{x}_1, \mathbf{x}_2)$ representing the series,

$$\begin{aligned} t_i(\mathbf{x}_1, \mathbf{x}_2) &= V_i(\mathbf{x}_1)\delta(\mathbf{x}_1 - \mathbf{x}_2) + V_i(\mathbf{x}_1) g_0(\mathbf{x}_1 - \mathbf{x}_2) V_i(\mathbf{x}_2) + \\ & \int V_i(\mathbf{x}_1) g_0(\mathbf{x}_1 - \mathbf{x}_3) V_i(\mathbf{x}_3) g_0(\mathbf{x}_3 - \mathbf{x}_2) V_i(\mathbf{x}_2) d\mathbf{x}_3 + \cdots, \end{aligned} \tag{2.9}$$

known as the Born series. The t-matrix depends on frequency with contributions from the scattering potential and the vacuum Green function. This dependence can even describe a geometrical resonance, leading to a large value for the norm of the t-matrix, while the dielectric constant (and hence the potential) is not especially large. Describing resonances for a photonic scatterer is one of the main advantages of using the t-matrix formalism over the scattering potential description. However, the explicit forms of the t-matrices are only known for a few objects including planes, wires, point scatterers, and dielectric spheres [36].

There are two commonly used short hand notations for the Born series:

$$t_i = V_i + V_i g_0 V_i + V_i g_0 V_i g_0 V_i + \cdots, \quad \text{or} \tag{2.10}$$

$$\bullet = \circ + \overset{\cdots\cdots}{\circ\!\!-\!\!\!-\!\!\circ} + \overset{\cdots\cdots}{\circ\!\!-\!\!\!-\!\!\circ}\!\!\overset{\cdots\cdots}{-\!\!\!-\!\!\circ} + \cdots, \tag{2.11}$$

where the full lines in the diagram are the free space Green functions and dotted lines connecting the scattering potential symbols denote recurrent scattering from the same scatterer. The diagrammatic notation (2.11) is based on the Feynman diagrams used for standard quantum field theory.

Since light has negligible mass and no charge, the scattering potential and hence the t-matrix is only nonzero inside the physical support of the scatterer. This fact makes a point scatterer such a realistic picture for any object that is justifiably smaller than the wavelength. For a point scatterer at position $\mathbf{r}_i$ the t-matrix is

$$t_i(\mathbf{x}_1, \mathbf{x}_2) = t\delta(\mathbf{x}_1 - \mathbf{r}_i)\delta(\mathbf{x}_2 - \mathbf{r}_i), \tag{2.12}$$

where t is generally a complex number that depends on frequency.

In principle, there is no restriction on the domain over which the scattering potential is defined. More specificly, there is no need that this domain should be a singly connected region in space. Therefore any object with whatever complicated geometry can be assumed a single scatterer. However, the concept of t-matrix for a single scatterer with finite support or definite shape is very useful in describing a particulate medium. Using the t-matrices of individual scatterers, instead of the scattering potential, makes it possible to distinguish between the recurrent scattering contributions within individual scatterers and the inter-particle scattering. In this approach, the resonances inside the scatterers survive the averaging over the position of scatterers. In reality, this is a more relevant picture for describing systems like a dilute atomic vapor or a colloidal suspension. Other approaches such as assuming a white noise potential can hardly describe a regime of resonant scattering.

2.1.3 Average Green function in the multiple scattering regime

After introducing the free space Green function and the t-matrix of a single scatterer, we are prepared to derive an expression for the full (unaveraged amplitude) Green function in presence of many scatterers. This Green function $g(\mathbf{r}, \mathbf{r}')$ is the answer to wave equation (2.2) in presence of a unit source at position $\mathbf{r}'$. Note that due to the inhomogeneities, the full Green function is no more translationally invariant. Similar to the previous section and with the help of t-matrices of individual scatterers, this solution can be written as a series of scattering from particles

$$\begin{aligned} g(\mathbf{r}, \mathbf{r}') &= g_0(\mathbf{r} - \mathbf{r}') + \sum_i \int g_0(\mathbf{r} - \mathbf{x}_1) t_i(\mathbf{x}_1, \mathbf{x}_2) g_0(\mathbf{x}_2 - \mathbf{r}') d\mathbf{x}_1 d\mathbf{x}_2 + \qquad (2.13) \\ & \sum_{i \neq j} \int g_0(\mathbf{r} - \mathbf{x}_1) t_i(\mathbf{x}_1, \mathbf{x}_2) g_0(\mathbf{x}_2 - \mathbf{x}_3) t_j(\mathbf{x}_3, \mathbf{x}_4) g_0(\mathbf{x}_4 - \mathbf{r}') d\mathbf{x}_1 d\mathbf{x}_2 d\mathbf{x}_3 d\mathbf{x}_4 + \cdots . \end{aligned}$$

This equation can be written as an iteration by introducing the self-energy (or mass) operator, $\Sigma(\mathbf{x}_1, \mathbf{x}_2)$, which is the sum of all irreducible diagrams:

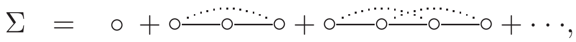

(2.14)

These are the diagrams that cannot be split in smaller scattering sequences without disrupting the recurrent scattering from a single particle. The iterative equation reads

$$g(\mathbf{r}, \mathbf{r}') = g_0(\mathbf{r} - \mathbf{r}') + \int g_0(\mathbf{r} - \mathbf{x}_1) \Sigma(\mathbf{x}_1, \mathbf{x}_2) g(\mathbf{x}_2, \mathbf{r}') d\mathbf{x}_1 d\mathbf{x}_2, \qquad (2.15)$$

The full Green function g is a useful tool for describing the propagation of waves in well parameterized heterogeneous structures such as periodic photonic arrays or metamaterials. However, it is seldom useful for describing experimental results on fully random structures, since it describes just a single realization. In these cases, one needs to average over realizations of disorder. The *average* Green function is given by

$$\langle g(\mathbf{r}, \mathbf{r}') \rangle \equiv G(\mathbf{r} - \mathbf{r}') = g_0(\mathbf{r} - \mathbf{r}') + \int g_0(\mathbf{r} - \mathbf{x}_1) \langle \Sigma(\mathbf{x}_1, \mathbf{x}_2) \rangle G(\mathbf{x}_2 - \mathbf{r}') d\mathbf{x}_1 d\mathbf{x}_2, \qquad (2.16)$$

which is called the Dyson equation and has the following diagrammatic notation:

(2.17)

Averaging, denoted by angular brackets, is performed by integrating over the positions of all scatterers and dividing by the volume once for every integration. The average (dressed) Green function is again translationally invariant in an statistically homogeneous infinite medium.

In the Fourier domain the Dyson equation is given by

$$G(\mathbf{p}) = g_0(\mathbf{p}) + g_0(\mathbf{p}) \Sigma(\mathbf{p}) G(\mathbf{p}), \qquad (2.18)$$

which leads to the result

$$G(\mathbf{p}) = \frac{g_0(\mathbf{p})}{1 - g_0(\mathbf{p}) \Sigma(\mathbf{p})} = \frac{1}{\frac{\omega^2}{c^2} - p^2 - \Sigma(\mathbf{p})}. \qquad (2.19)$$

If $\Sigma(\mathbf{p})$ has a mild dependence on $\mathbf{p}$, the following compact form can be obtained after transforming back to the space coordinates:

$$G(\mathbf{r}) = -\frac{e^{\imath K r}}{4\pi r}, \tag{2.20}$$

with K the effective (complex-valued) wave number.

Estimation of the average mass operator is not a trivial task in general. For a low density of scatterers, the independent scattering approximation applies. In this approximation, contributions from recurrent scattering are neglected because they are of higher order in density. Applying this approximation to scattering from a collection of identical point scatterers leads to the following average mass operator

$$\langle \Sigma(\mathbf{x}_1, \mathbf{x}_2) \rangle \approx \int \left(\sum_i t\delta(\mathbf{x}_1 - \mathbf{r}_i)\delta(\mathbf{x}_2 - \mathbf{r}_i) \right) \prod_i \frac{d\mathbf{r}_i}{V} = \rho t \delta(\mathbf{x}_1 - \mathbf{x}_2), \tag{2.21}$$

where V is the integration volume ρ is the density of scatterers. In this approximation, the effective wave number reads

$$K = \sqrt{\frac{\omega^2}{c^2} + \rho t} = \frac{n_e \omega}{c} + \frac{\imath}{2\ell_s} \tag{2.22}$$

The effective refractive index n_e determines the phase velocity and is connected to the real part of the t-matrix . The exponential decay in the coherent amplitude of the propagating wave is caused by the scattering out of the propagation direction and therefore ℓ_s is called the scattering mean free path. The amplitude Green function has a short range. It only describes the decay of impinging coherent beam, known as the Lambert-Beer law. To describe the long range transport of intensity in disordered media, one has to develop a theory of multiple scattering on the intensity level.

2.1.4 Diffusion approximation

The exponential spatial decay in the average Green function G is caused by the reduction of coherent amplitude due to scattering. This light can scatter back in the initial propagation direction but with a scrambled phase, and therefore just adds to the "diffuse" background. This makes the detection of the coherent part very difficult since in most experiments one measures the intensity at a location irrespective to its in-flow direction.

Intensity of a monochromatic wave at each point in space is proportional to the absolute value squared of its total amplitude, considering a slowly varying envelope on the scale of wavelength. To obtain the average intensity, one has to add up all the amplitude contributions that reach the detection point from various paths, and multiply the sum by its complex conjugate. The average intensity propagator in a statistically homogenous medium is defined as:

$$R(\mathbf{r} - \mathbf{r}') \equiv \langle g(\mathbf{r}, \mathbf{r}') \bar{g}(\mathbf{r}, \mathbf{r}') \rangle, \tag{2.23}$$

with the bar on the symbol denoting the complex conjugate. This path information is indeed in the full Green function g but is lost in the average Green function G. Therefore, the norm above must be taken before the averaging is performed.

Similar to the construction of the Dyson equation, it is possible to separate the contribution of the irreducible diagrams and write an iterative equation for the average intensity propagator with the following symbolic construction

$$R \;=\; G\bar{G} + G\bar{G}UR, \tag{2.24}$$

where U denotes the irreducible vertex. This equation is called the Bethe-Salpeter equation. The actual form of U is not local and can connect scatterers at different positions. In the lowest order with respect to the scatterer density, U is approximated by a local object given by the t-matrix ,

$$U \approx \langle \ell \rangle \approx n t \bar{t} \delta(\mathbf{x}_1 - \mathbf{r}_i)\delta(\mathbf{x}_2 - \mathbf{r}_i). \tag{2.25}$$

Within the same approximation, the average intensity propagator can now be built by consequently connecting the irreducible vertices by a pair of average Green function and its complex conjugate. This diagrma is called the ladder vertex (because of its shape). All the diagrams where these pairs differ in their starting or end points are thus neglected. This treatment is called the diffusion approximation. The ladder vertex is denoted by the following diagram

$$\mathcal{L} \equiv \boxed{\mathrm{L}} =$$

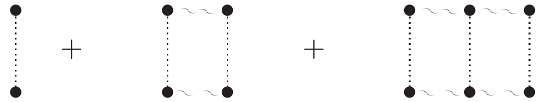

$$+ \cdots, \tag{2.26}$$

were the connected curly lines (top) are average Green functions and the broken ones are their complex conjugates. Note that, unlike R, there is no incoming or outgoing amplitude propagators connected to $\mathcal{L}$ and it ends on the scatterer. The equivalent of Bethe-Salpeter equation for $\mathcal{L}$ is given by

$$\mathcal{L} \;=\; \langle \ell \rangle + \langle \ell \rangle G \bar{G} \mathcal{L}. \tag{2.27}$$

At this point, we are just a few derivation steps short of having the explicit form of the diffusion equation for classical waves. We shall skip these derivation, since it can be found in several textbooks and review articles with more details [116, 132], and only present the final expression for an infinite medium:

$$\mathcal{L}(\mathbf{r}) \;=\; \frac{4\pi}{\ell_s}\delta(\mathbf{r}) + \frac{3}{\ell_s^3 r}, \tag{2.28}$$

where absorption has been neglected. The derivation of a more general form of the ladder diagram will be presented in section 2.2.1. That calculation will be used to describe the new experimental results, which are reported in chapter 7.

2.2 Mesoscopic intensity correlations

Beside intensity distribution and average transport, correlations are perhaps the most commonly measured quantities for describing wave propagation in disordered media. Multiple scattering of waves produces a complicated and strongly varying intensity pattern. This intensity structure, albeit looking very irregular, is correlated in time and space, or correspondingly in frequency and momentum. The theoretical developments in describing these correlation functions has been much stimulated by the exchange of ideas between the fields of condensed matter physics (electrical conductance) and optics (speckle). For transmission through a waveguide with disorder Feng et al. [49] showed, in a pioneering paper, that one can distinguish three different types of correlations in the transmitted intensity,

$$C_{aba'b'} \equiv \langle T_{ab} T_{a'b'} \rangle - \langle T_{ab} \rangle \langle T_{a'b'} \rangle = C^{(1)} + C^{(2)} + C^{(3)}, \tag{2.29}$$

where T_{ab} is the fraction of intensity transmitted from incoming mode a to outgoing mode b. This fraction depends on the disorder realization , but the identified correlations are universal. The first term in Eq. (2.29), $C^{(1)}$, is of order unity. The second term, $C^{(2)}$, is of order g_D^{-1}, the last term, $C^{(3)}$, is of order g_D^{-2}, with g_D the dimensionless (Thouless) conductance, is defined as $\sum_{a,b} T_{ab}$ based on the Landauer formula. The three contributions are subject to different selection rules on the momenta of the incoming and outgoing channels. Making use of these selection rules allows for experimental observation of the (generally much) smaller $C^{(2)}$ and $C^{(3)}$ contributions. Given these selection rules, higher-order terms like $C^{(4)}$ can be incorporated in a renormalization of the previous three contributions. The $C^{(1)}$-contribution is short range, so decays exponentially with the difference in momenta (or in frequency) of the incoming and outgoing channels. The $C^{(2)}$ and $C^{(3)}$ are long range in angular coordinates. In samples which are not so strongly scattering, the lower order term dominates. It is difficult to reach an experimental situation in turbid samples where the higher-order correlations become observable. These three types of correlations have been measured before in microwave and also at optical frequencies [29, 54, 109, 129].

With proper modifications to definition (2.29), an equivalent $(C^{(1)} + C^{(2)} + C^{(3)})$ classification is also possible for an infinite medium. In such an unbound medium the expansion parameter is given by $(k\ell)^{-1}$ instead of g_D^{-1}, where k is the wave-number and ℓ is the (scattering) mean free path (we have dropped the subscript s). When $k\ell \gg 1$, $C^{(1)} \sim 1$, $C^{(2)} \sim (k\ell)^{-2}$, and $C^{(3)} \sim (k\ell)^{-4}$ [119].

For the experimental work presented in chapter 7, we need to compare the dependence of intensity correlations on frequency variation with that of the refractive index changes. A typical intensity correlation function that we use, is defined as

$$\begin{aligned} C_{\omega,\omega+\Delta\omega}(n_h, n_h + \Delta n_h) \equiv N\, [&\langle I_\omega(\hat{s}; n_h) I_{\omega+\Delta\omega}(\hat{s}; n_h + \Delta n_h)\rangle \\ &- \langle I_\omega(\hat{s}; n_h)\rangle \langle I_{\omega+\Delta\omega}(\hat{s}; n_h + \Delta n_h)\rangle] \,, \end{aligned} \tag{2.30}$$

where $I_\omega(\hat{s})$ is the far-field specific intensity at direction $\hat{s}$. The normalization constant N is fixed by requiring $C_{\omega,\omega}(n_h, n_h) = 1$. In the conventional definitions of similar correlation functions the variation of n_a has not been considered.

The calculation of correlation function (2.30) for the case of $\Delta n_h = 0$ is by now standard and can be found in many papers and textbooks. The actual expressions depends on the geometry and closed forms have been presented for the case of an infinite medium [115], a semi-infinite medium [52], a slab [132] and a sphere [75]. By using the generalization presented in this section, all these formula's can easily be mapped to the case of $\Delta n_h \neq 0$.

2.2.1 Average amplitude correlator

The most encountered object for describing the intensity transport properties in the diffusion approximation is perhaps the so-called ladder vertex. In the stationary regime, the averaged intensity propagator is approximated by connecting two incoming and two outgoing average Green functions to the ladder vertex. The slowly varying time-dependent intensity propagation can also be approximated by a modified ladder vertex in which the two legs of the ladder are carried at slightly different frequencies. This latter object can also describe the amplitude correlations at two different frequencies and is a building block in calculating mesoscopic correlations. Here we present the derivation of a generalized ladder vertex, which can incorporate the correlations in change of effective refractive index as well as frequency correlations.

The averaged amplitude correlator for changes in both frequency and refractive index is defined as

$$R_{\omega,\omega+\Delta\omega}(\mathbf{r}-\mathbf{r}'; n_e, n_e+\Delta n_e) \equiv \langle g_\omega(\mathbf{r},\mathbf{r}'; n_e)\bar{g}_{\omega+\Delta\omega}(\mathbf{r},\mathbf{r}'; n_e+\Delta n_e)\rangle, \tag{2.31}$$

where the frequency subscript is added to the symbol for Green function to point out the difference in the frequency of the two amplitude propagators. The reader may have noted the similarities between the definition of this amplitude correlator (2.31) and the average intensity propagator (2.23).

It is now easy to guess the next step: to use the diffusion approximation. The ladder propagator is, as usual, defined by considering only the same sequence of scatterers along the two legs. Note that all the changes in the realization of disorder has been contracted in the change of the effective refractive index. Such a system can be realized by placing a solid backbone of scatterers (quenched disorder) in a a liquid or gaseous host medium. Any change in the refractive index of the host medium can then be translated to the change in the effective refractive index. This approximation has some limitations. For instance it cannot describe the evolving disordered media with constant effective index. An example for such a medium is a colloidal suspension. For these type of samples, a very similar formalism has been introduced some time ago under the title of diffusing wave spectroscopy [85, 104]. This technique has since found several applications for the characterization of turbid media.

In accordance with section 2.1.4, in the diffusion approximation, the amplitude correlator is approximated by a generalized ladder diagram. The calculation of this ladder vertex is easier in the momentum space. It follows the following Bethe-Salpeter equation

$$\begin{aligned}\mathcal{L}_{\omega,\omega+\Delta\omega}(\mathbf{p}; n_e, \Delta n_e) = \langle\ell\rangle \quad + \quad & \langle\ell\rangle\mathcal{L}_{\omega,\omega+\Delta\omega}(\mathbf{p}; n_e, \Delta n_e) \\ & \times \int G_\omega(\mathbf{p}'; n_e)\bar{G}_{\omega+\Delta\omega}(\mathbf{p}'-\mathbf{p}; n_e+\Delta n_e)\frac{d\mathbf{p}'}{(2\pi)^3},\end{aligned} \tag{2.32}$$

where G_ω is the average Green function given by Eq. (2.20). The single scattering vertex $\langle\ell\rangle = nt(\mathbf{p}; \omega, n_e)\bar{t}(\mathbf{p}; \omega+\Delta\omega, n_e+\Delta n_e) \approx 4\pi/\ell_s$ is assumed to be independent of $\Delta\omega$, Δn_e and $\mathbf{p}$ (nonresonant isotropic scattering). This approximation needs

$$\frac{\partial \mathrm{Im}\, t}{\partial\omega}, \frac{1}{\omega}\frac{\partial \mathrm{Im}\, t}{\partial n_e} \ll \frac{\sqrt{\ell_s}}{c} \tag{2.33}$$

to hold, which is generally the case if the individual resonances of separate scatterers are inhomogeneously broadened.

The solution to the recursive equation (2.32) is

$$\mathcal{L}_{\omega,\omega+\Delta\omega}(\mathbf{p}; n_e, n_e+\Delta n_e) = \frac{4\pi}{\ell_s(1-M)}, \tag{2.34}$$

with

$$M = \frac{4\pi}{\ell_s}\int G_\omega(\mathbf{p}'; n_e)\bar{G}_{\omega+\Delta\omega}(\mathbf{p}'-\mathbf{p}; n_e+\Delta n_e)\frac{d\mathbf{p}'}{(2\pi)^3}. \tag{2.35}$$

This integral can be evaluated by a Fourier transform to the position coordinates:

$$M = \int G_\omega(\mathbf{r}; n_e)\bar{G}_{\omega+\Delta\omega}(\mathbf{r}; n_e+\Delta n_e)e^{\imath\mathbf{p}\cdot\mathbf{r}}d\mathbf{r}. \tag{2.36}$$

We assume Δn_e to be small and real-valued, and thus terms including $\Delta\omega\Delta n_e$ can be neglected. Using the expressions (2.20) and (2.22) for average Green functions, and expanding the integral M in spherical coordinates reads

$$\begin{aligned}
M &= \int_0^\pi \int_0^\infty \int_0^{2\pi} \frac{e^{\imath n_e \frac{\omega}{c} r - \frac{r}{2\ell_s}} e^{-\imath n_e \frac{\omega}{c} r - \imath(n_e\Delta\omega + \omega\Delta n_e) r - \frac{r}{2\ell_s}} e^{\imath p r \cos\theta}}{(4\pi r)^2} r^2 \sin\theta d\phi dr d\theta \\
&= \frac{1}{8\pi} \int_{-1}^{1} \int_0^\infty e^{-[\ell_s^{-1} + \imath(n_e\Delta\omega + \omega\Delta n_e - \mu p)]r} dr d\mu \\
&= \frac{1}{8\pi} \int_{-1}^{1} \frac{d\mu}{\ell_s^{-1} + \imath(n_e\Delta\omega + \omega\Delta n_e - \mu p)} \\
&= \frac{\imath}{8\pi p} \int_{\imath p}^{-\imath p} \frac{dz}{\ell_s^{-1} + \imath(n_e\Delta\omega + \omega\Delta n_e) + z} \\
&= \frac{\imath}{8\pi p} \ln \frac{\ell_s^{-1} + \imath(n_e\Delta\omega + \omega\Delta n_e) - \imath p}{\ell_s^{-1} + \imath(n_e\Delta\omega + \omega\Delta n_e) + \imath p} \\
&= \frac{1}{4\pi p} \arctan\left[\frac{p\ell_s}{1 + \imath\ell_s(n_e\Delta\omega + \omega\Delta n_e)}\right] \qquad (2.37)
\end{aligned}$$

The result for M is then expanded relative to small parameters $p\ell_s$ and $\ell_s(n_e\Delta\omega + \omega\Delta n_e)$. The first nonzero orders of p, $n_e\Delta\omega$, and $\omega\Delta n_e$ are kept and the $p(n_e\Delta\omega + \omega\Delta n_e)$ term is neglected. The final result for the generalized ladder vertex reads

$$\mathcal{L}_{\omega,\omega+\Delta\omega}(\mathbf{p}; n_e, n_e + \Delta n_e) = \frac{12\pi}{\ell_s^3} \frac{1}{p^2 + 3\imath(n_e\Delta\omega + \omega\Delta n_e)/\ell_s}. \qquad (2.38)$$

We have just proved that $\mathcal{L}$ depends on Δn_e and $\Delta\omega$ only in terms of the variation of their product $n_e\Delta\omega + \omega\Delta n_e \equiv \Delta(n_e\omega)$.

Note that in order to express Eq. (2.38) in terms of the conventional diffusion constant, phase velocity and the energy velocity should be equal; $v_e = v_p$.

2.2.2 Short-range intensity correlations

The amplitude correlator (2.31) is sufficient for describing the short range intensity correlations in the diffusion approximation. In principle, the intensity correlator diagram connects four intensities or eight amplitudes. However, in the lowest order with respect to the scattering strength, this diagram splits into two disjoint ladder diagrams, as was shown by Feng et al. [49]. Based on the last result of the previous section, to describe the short range part of the intensity correlation (2.30) for any geometry, we can just use the its counterpart for the frequency correlation and replace $\Delta(n_e\omega)$ for $n_e\Delta\omega$.

For the higher order correlations, $C^{(2)}$, and $C^{(3)}$, one should prove that the Hikami vertex has also this symmetry. In the Hikami vertex two ladder diagrams switch one of their legs. We conjecture that the Hikami vertex has also the same symmetry of the ladder vertex for change of effective refractive index. This is the case since we are just replacing a real-valued small variable $n_e\Delta\omega$ with another real-valued small variable $n_e\Delta\omega + \omega\Delta n_e$. No dissipative term is expected to emerge from this replacement.

2.2.3 Non-universal C_0 correlations

A different contribution to the intensity correlation in random media has been identified by Shapiro [113] and has been called C_0. In an infinite random medium with Guassian white noise disorder the C_0-correlations is of the order of $(k\ell)^{-1}$. This correlation is suggested to be of infinite range for any type of disorder. One may wonder why this correlation was not discovered earlier. In our opinion this could be explained by the fact that the C_0-correlations only show up if a *source* is involved. When dealing with electrons in condensed matter physics one hardly ever has to take into account sources of electrons. In such an experiment charge is conserved and never created or destroyed. In contrast to the case of electrons, sources of light can easily be embedded inside a random medium. This fundamental difference makes C_0 a property specific to classical (electromagnetic) waves, which does not have a counterpart in phenomena related to multiple scattering of electron wave functions in a random potential.

So far, there has been only one report on the experimental observation of a mesoscopic C_0-signature and that has been in the polarization correlation of multiple-scattered microwaves [29]. A very interesting development has been the derivation by van Tiggelen and Skipetrov [133]. They showed that the spatial C_0-correlations is exactly equal to the fluctuations in the local density of (radiative) states (LDOS). This equivalence have been numerically exploited [27]. Very large LDOS fluctuations have been observed decades ago by Weaver in ultrasound experiments. He did not find it very interesting and saw them rather annoying. Another opinion is that C_0-correlations is just a trivial consequence of considering a constant amplitude source, for which the emitted power always depends on LDOS in any environment [42].

The fluctuation of LDOS in bulk random media have been measured in samples with moderate scattering strength by Birowosuto et. al [20], but their analysis shows that it is mainly influenced by the single nearest scatterer to the source. A similar measurement for planar plasmonic aggregates is performed more recently [71]. Both these measurements are based on the decay lifetime of dye molecules embedded inside the medium. Direct measurement of the C_0-correlations and their range is still amenable to experimental verification.

In the next section we will identify a macroscopic, experimentally observable, property that would be directly connected to C_0-correlations . We show that C_0-correlations increase the amount of second-harmonic generation relative to the theoretical predictions that use just the Rayleigh-distribution of speckle intensities. This additional signal can be extracted from a two beam experiment, which we will discuss in the experimental chapter 7. In our proposed experiment, it is also possible to measure the range of these correlations as well. Before presenting this relation, we have to first prepare a theoretical foundation that describes nonlinearities in multiple scattering media.

2.3 Nonlinear random media

An opaque medium may also be optically nonlinear. This nonlinearity can be an intrinsic property of the bulk material or a result of the enormous interfacial area present in porous objects. The second-order nonlinearity is absent in many non-crystalline materials or crystal structures because of the presence of inversion symmetry. However, relatively large nonlinearities may arise at the interfaces due to crystal symmetry breaking.

The scientific understanding of optical nonlinear processes in strongly-scattering materials is still very limited. Some models have been developed [73, 83] based on the diffusion approximation, in which interference effects are assumed to be averaged out and the sample size L is taken much larger than the transport mean free path. In these diffusion models the incident wave at the fundamental frequency 1ω experiences several scattering events before leaving the random medium. Light at the second-harmonic frequency is generated during the multiple-scattering process. The propagation direction of the second-harmonic light is scrambled within one transport mean free path $\ell_{2\omega}$, thus becoming an isotropic source of diffusive photons at the second-harmonic frequency. The net effect of phase-mismatch between the fundamental and the second-harmonic light is washed out when the transport mean free path is much smaller than the coherence length $L_c(\omega) \equiv \pi/|2k_{1\omega} - k_{2\omega}|$, where $k_{1\omega}$ and $k_{2\omega}$ are the wave-vector magnitudes at the fundamental and the second-harmonic frequencies. Therefore, in a nonlinear random medium that consists of crystalline grains, the effect of constructive interference can be overcome by selecting the grain size to be shorter than the coherence length. It has been experimentally shown that the second-harmonic yield from equal amount of material increases with grain size until the grain size approaches the coherence length [12].

Overcoming the destructive interference due to phase-mismatch is also possible by introducing scatterers inside a homogeneous nonlinear crystal. In such a medium the fundamental and second-harmonic waves scatter differently, therefore the destructive interference of the otherwise co-propagating waves does not occur, provided $\ell_{1\omega}, \ell_{2\omega} \ll L_c$.

Second-harmonic signals from multiple scattering media have been used before to study experimentally the angular, spatial and temporal correlations, however all experiments were of the short range $C^{(1)}$ type [34, 65].

In theoretical treatments, some interference effects such as the effect of weak localization or the enhanced forward scattering have been discussed [2, 63, 84, 143]. Recently, observations of diffusive second-harmonic generation in porous materials [45, 90, 128], semiconductor powders [12], plasmonic structures [17, 124] and colloidal suspensions [147], have extended the scope of the applications this research topic.

In previous theoretical treatments the mean free path was always assumed to be much larger than the wavelength. In this weakly-scattering regime the diffusion approximation was used to computed the second-harmonic yield based on the lowest-order non-zero contribution in the diffusion theory. The resulting second-harmonic yield was shown to be independent of the mean free path in a medium without optical dispersion, except for the trivial part given by the density of nonlinear scatterers. In none of these models the C_0-correlations were taken into account. Here we demonstrate that a new "mesoscopic" contribution arises by considering the presence of scatterers in vicinity of the conversion center. A similar contribution is responsible for the C_0-correlations . The link with C_0 is related to the fact that second-harmonic photons are generated "inside" the scattering medium and constitute a genuine source. The C_0-correlation constitutes the leading term in the $k\ell$-dependence of the optical second-harmonic generation in a random colloidal suspension. This dependence on the scattering strength can be extracted from a measurement of the second-harmonic yield as a function of the mean free path. Since C_0-correlations is known to be dependent on the microscopic structure of disorder, this equivalence may be useful for non-invasive characterization of disorder in turbid media. In chapter 7 we will draw a very general relation between this type of correlation with an observable macroscopic quantity related to second-harmonic generation. This quantity can be inferred when from the total second-harmonic yield in a two-beam illumination setting.

Our calculation is also applicable to the other nonlinear processes, which can be incoherent and inelastic. For example, the same theory describes the two-photon excitation process of emitters embedded in strongly-scattering media. The two-photon excitation and luminescence of gold nanorods and other flourophores has recently attracted attention for optical data storage [148] and high-resolution imaging [25, 130] inside living biological structures. The effect of multiple-scattering on this excitation process has not been reported yet. In such a system measuring the radiation lifetime of the emitters will provides the extra opportunity of measuring fluctuations in local density of states. It is then possible to compare the C_0-correlation with the fluctuation of local density of states, in connection with the equivalence suggested by van Tiggelen and Skiperov.

In the following section we illustrate different contributions to the second-harmonic generation process. A stationary scalar model is used in accordance with earlier works on second-harmonic generation and earlier work on the C_0-correlations . In chapter 7, we will show see how a scalar approximation fails for describing certain nonlinear systems, but is applicable to some others. However, for the current discussion the scalar model is sufficient to show the C_0 contribution to second-harmonic yield.

2.3.1 Second-harmonic t-matrix

The first step is to describe an individual nonlinear conversion center that is embedded inside a multiple-scattering medium. Considering the wide application of multi-photon processes in modern photonics, we would like to introduce the concept of the t-matrix for a nonlinear single scatterer. To our knowledge, this is the first time that such a concept is used for nonlinear scattering. We should not forget that the application of this concept is much more general than the simplified version we need in this dissertation. Therefore, it is worthwhile if we spend a few lines on describing the concept in its most general form and then simplify it to a degree that can be handled in our model.

The second-harmonic generation and scattering is fully described by the nonlinear t-matrix $\tilde{t}_i(\mathbf{x}_1, \mathbf{x}_2, \mathbf{x}_3)$, where the curly hat is used to differentiate between this object and the linear t-matrix of Eq. 2.9. The index i is the scatterer index. We envisage a situation for the conversion process that either occurs once or does not occur at all. Hence the repetitive nonlinear conversion processes are excluded. Taking this condition into account, the most general form of describing the generation of a second-harmonic field amplitude $\psi_{2\omega}(\mathbf{y})$ from this individual scatterer is

$$\psi_{2\omega,i}(\mathbf{y}) = \int g_{2\omega}(\mathbf{y}, \mathbf{x}_3)\tilde{t}_i(\mathbf{x}_3; \mathbf{x}_1, \mathbf{x}_2)\psi_{1\omega}(\mathbf{x}_1)\psi_{1\omega}(\mathbf{x}_2)d\mathbf{x}_1 d\mathbf{x}_2 d\mathbf{x}_3, \tag{2.39}$$

where the indices 1ω and 2ω next to each quantity denote whether it is referring to the fundamental or the second harmonic frequency. The integration is performed over the support of the scatterer. The fundamental field amplitude at point $\mathbf{x}$, $\psi_{1\omega}(\mathbf{x})$, is given by the linear amplitude Green function connected to the source and is not influenced by the nonlinear processes. The second-harmonic scattering process is schematically drawn in Fig. 2.1. We assume that the two-wave mixing process has a microscopic (molecular) origin, so that it only occurs if the three amplitudes meet at the same point in space.

Equation (2.39) can be simplified in the following steps. If the conversion center is transparent or weakly scattering for the fundamental light, there will be no transport of the fundamental light inside the conversion center:

$$\tilde{t}_i(\mathbf{x}_3; \mathbf{x}_1, \mathbf{x}_2) \approx \tilde{t}_i(\mathbf{x}_3; \mathbf{x}_1)\delta(\mathbf{x}_1 - \mathbf{x}_2). \tag{2.40}$$

If the conversion center is also assumed to be weakly scattering for the second-harmonic light, then the second harmonic light leaves the conversion center after its generation,

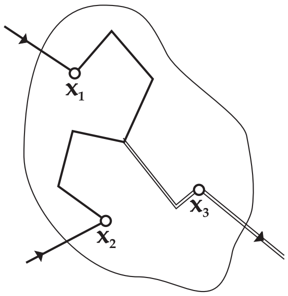

Figure 2.1: The schematic drawing of the second-order t-matrix block for one individual scatterer. The lines and the double-lines represent the amplitude Green functions at the fundamental and the second-harmonic frequencies.

without further scattering inside this object. Therefore, we can write

$$\tilde{t}_i(\mathbf{x}_3; \mathbf{x}_1, \mathbf{x}_2) \approx \tilde{t}_i(\mathbf{x}_1)\delta(\mathbf{x}_1 - \mathbf{x}_2)\delta(\mathbf{x}_1 - \mathbf{x}_3). \tag{2.41}$$

Finally, considering the size of the source to be much smaller than the wavelength, the nonlinear transfer matrix can be replaced by the following zero-range object:

$$\tilde{t}_i(\mathbf{x}_1, \mathbf{x}_2; \mathbf{x}_3) \approx \tilde{t}_i\delta(\mathbf{x}_1 - \mathbf{x}_2)\delta(\mathbf{x}_1 - \mathbf{x}_3)\delta(\mathbf{x}_1 - \mathbf{r}_i), \tag{2.42}$$

where $\mathbf{r}_i$ indicates to the position of the i-th scatterer and $\tilde{t}_i$ is a (complex-valued) scalar that depends on the physical parameters of the point scatterer. The value of this scalar is determined by the shape, volume and intrinsic material properties of the scattering object that is mimicked as a point conversion center. (As an example for spherical particles see Ref. [83]). After inserting approximation (2.42) in Eq. (2.39), the generated second-harmonic field due to an individual nonlinear scatterer reads

$$\psi_{2\omega,i}(\mathbf{y}) = \tilde{t}_i g_{2\omega}(\mathbf{r}_i, \mathbf{y})\psi^2_{1\omega}(\mathbf{r}_i). \tag{2.43}$$

For a collection of conversion centers embedded in the random medium, the generated field at the second harmonic frequency is given by

$$\psi_{2\omega}(\mathbf{y}) = \sum_i \tilde{t}_i g_{2\omega}(\mathbf{r}_i, \mathbf{y})\psi^2_{1\omega}(\mathbf{r}_i), \tag{2.44}$$

where the summation is taken over all the conversion centers, and as before repetitive conversion events have been excluded. To find the second-harmonic intensity distribution inside the medium, Eq. (2.44) must be multiplied by its complex conjugate. We now perform the ensemble averaging over several realizations of the disorder (generated by changing positions and orientations of scatterers).

$$\begin{aligned}
\langle I_{2\omega}(\mathbf{y})\rangle &\equiv \langle \psi_{2\omega}(\mathbf{y})\bar{\psi}_{2\omega}(\mathbf{y})\rangle \\
&= \sum_{i,j}\langle g_{2\omega}(\mathbf{r}_i, \mathbf{y})\bar{g}_{2\omega}(\mathbf{r}_i, \mathbf{y})\tilde{t}_i\bar{\tilde{t}}_j\psi^2_{1\omega}(\mathbf{r}_i)\bar{\psi}^2_{1\omega}(\mathbf{r}_j)\rangle. \\
&= \sum_{i}\langle g_{2\omega}(\mathbf{r}_i, \mathbf{y})\bar{g}_{2\omega}(\mathbf{r}_i, \mathbf{y})\tilde{t}_i\bar{\tilde{t}}_i\psi^2_{1\omega}(\mathbf{r}_i)\bar{\psi}^2_{1\omega}(\mathbf{r}_i)\rangle \\
&\quad + \sum_{i\neq j}\langle g_{2\omega}(\mathbf{r}, \mathbf{r}_i)\bar{g}_{2\omega}(\mathbf{r}, \mathbf{r}_j)\tilde{t}_i\bar{\tilde{t}}_j\psi^2_{1\omega}(\mathbf{r}_i)\bar{\psi}^2_{1\omega}(\mathbf{r}_j)\rangle \qquad (2.45) \\
&\approx \sum_{i}\langle g_{2\omega}(\mathbf{r}_i, \mathbf{y})\bar{g}_{2\omega}(\mathbf{r}_i, \mathbf{y})\tilde{t}_i\bar{\tilde{t}}_i\psi^2_{1\omega}(\mathbf{r}_i)\bar{\psi}^2_{1\omega}(\mathbf{r}_i)\rangle \\
&\approx \sum_{i}\langle g_{2\omega}(\mathbf{r}_i, \mathbf{y})\bar{g}_{2\omega}(\mathbf{r}_i, \mathbf{y})\rangle\, \tilde{t}_i\bar{\tilde{t}}_i\, \langle\psi^2_{1\omega}(\mathbf{r}_i)\bar{\psi}^2_{1\omega}(\mathbf{r}_i)\rangle \qquad (2.46)
\end{aligned}$$

The second summation in Eq. (2.45) contains rapidly varying complex numbers that will not survive the ensemble averaging. The remaining diagonal part contains the product of field amplitudes at the fundamental frequency and the amplitude Green function at the second harmonic frequency. This averaging can be safely decoupled if one neglects the reverse up-conversion process. The final result, equation (2.46), shows the local nature of the conversion process but also emphasizes the importance of local intensity fluctuations at the fundamental frequency. This result has a fascinating property that an average intensity (l.h.s.) is determined by a quantity (r.h.s.) that contains intensity *fluctuations*. If the fundamental intensity fluctuation contains the C_0-correlations so will be for the second harmonic (average) intensity.

2.3.2 Diffusion approximation for the second-harmonic generation

In the diffusive regime, the calculation of the averages in Eq. (2.46) is straightforward, and has been presented previously in different contexts. The $\langle g_{2\omega}\bar{g}_{2\omega}\rangle$ part can be approximated by the ladder diagram, as discussed in section 2.1.4. This term propagates the second-harmonic intensity generated inside the medium to the point of observation.

The last average in Eq. (2.46) is the second moment of the intensity at the fundamental frequency and can be written in terms of the mesoscopic correlations:

$$\langle \psi_{1\omega}^2(\mathbf{r})\psi_{1\omega}^{*2}(\mathbf{r})\rangle = \langle I_{1\omega}(\mathbf{r})\rangle^2\left[2 + C_0 + \mathcal{O}(k\ell^{-2})\right], \tag{2.47}$$

where $\langle I_{1\omega}(\mathbf{r})\rangle$ is the average intensity that is propagated to the conversion center from the source and can be written in terms of the intensity propagator (2.23)

$$\langle I_{1\omega}(\mathbf{r})\rangle = \int R_{1\omega}(\mathbf{r}-\mathbf{r}')|\psi_{\mathrm{in}}(\mathbf{r}')|^2 d\mathbf{r}', \tag{2.48}$$

which in its turn will be estimated by another diffusion propagator at the fundamental frequency. The factor two in the brackets in Eq. (2.47) is the well-known interference effect in the speckle field, which also leads to the Rayleigh distribution for the intensity. It generally appears for any coherent interference pattern. The C_0 term has to be considered since the sink of fundamental light (the conversion center) is inside the scattering medium. These contributions are given by the diagrams plotted in Fig. 2.2. In the following section we will present the explicit form of these diagrams and their value for a specific type of disorder.

Before digging into the algebraic derivation of the C_0 contribution to second-harmonic generation, one point is worth mentioning. The relation between second-harmonic intensity and the second moment of intensity fluctuations at the fundamental frequency is more general than its expansion in terms of mesoscopic correlations. This relation holds in any multiple-scattering system, even if the scattering is so strong that the diffusion approximation does not hold anymore. For example near the transition to localization strong mesoscopic spatial fluctuations and two wavefunction correlations are predicted [32]. Both these effect will strongly effect the nonlinear conversion processes. Measuring nonlinear effects may thus be essential for probing certain properties on the verge of localization, which are not measureable otherwise.

2.3.3 Derivation of the C_0 vertex

For the sake of completeness, we briefly review here the derivation of the C_0 vertex, as was first introduced and derived by Shapiro [113]. It is diagrammatically represented in the left

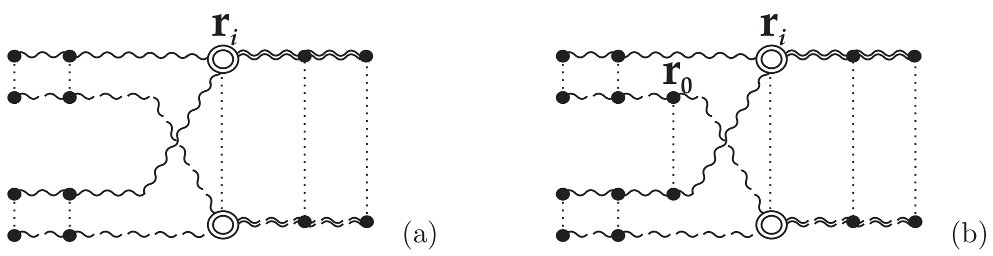

Figure 2.2: The diagrammatic representation of second-harmonic generation and propagation processes in the diffusion approximation. The full circle is the t-matrix of a scatterer. The connected curly lines are the dressed Green functions at the fundamental frequency and the broken lines represent their complex conjugates. The thin dotted lines connect identical scatterers. The double circle is the second-order t-matrix of a conversion center. The double-lines are dressed Green functions at the second-harmonic frequency. The plotted diagrams represent: (a) the lowest order contribution to the second-harmonic generation that survives ensemble averaging and (b) a higher order diagram for the second-harmonic generation that includes the C_0-correlation.

half of Fig. 2.2 and can be explicitly written as

$$C_0 = 2 \times \frac{4\pi}{\ell_{1\omega}} \int \mathcal{F}_{1\omega}(\mathbf{r},\mathbf{r}_0)\bar{G}_{2\omega}(\mathbf{r}_0-\mathbf{r})\mathcal{F}_{1\omega}(\mathbf{r}_0,\mathbf{r})G_{2\omega}(\mathbf{r}-\mathbf{r}_0)d\mathbf{r}_0, \tag{2.49}$$

where the spatial amplitude correlator [112] is used.

$$\begin{aligned} \mathcal{F}_{1\omega}(\mathbf{r}_1,\mathbf{r}_2) &\equiv \langle \psi_{1\omega}(\mathbf{r}_1) bar\psi_{1\omega}(\mathbf{r}_2)\rangle \\ &= \langle I_{1\omega}(\frac{\mathbf{r}_1+\mathbf{r}_2}{2})\rangle \exp\left(-\frac{|\mathbf{r}_1-\mathbf{r}_2|}{2\ell_{1\omega}}\right)\frac{\sin k_{1\omega}|\mathbf{r}_1-\mathbf{r}_2|}{k_{1\omega}|\mathbf{r}_1-\mathbf{r}_2|}. \end{aligned} \tag{2.50}$$

The pre-factor two at the right hand side of Eq. (2.49) originates from the degeneracy in linking the ladder diagrams to the extra scatterer at $\mathbf{r}_0$. Note that in this derivation we are considering all the scatterers and the conversion center to be point-like. The derivation of C_0 in a media with correlated disorder has been presented in Ref. [119]. With the information provided above the integral can be readily evaluated. The integrand is consisted of exponential and sinc functions. It is dominated by the region of small $|\mathbf{r}_i - \mathbf{r}_0|$ and decays rapidly within one mean free path. The present calculation is accurate up to the order of $\frac{1}{k_{1\omega}\ell_{1\omega}}$ so the higher orders can be neglected. The final result takes the following simple form:

$$\begin{aligned} C_0 &= \frac{2}{k_{1\omega}\ell_{1\omega}}\int_0^\infty \frac{\sin^2(s)}{s^2}\exp(-\frac{2s}{k_{1\omega}\ell_{1\omega}})ds. \\ &= \frac{\pi}{k_{1\omega}\ell_{1\omega}} \end{aligned} \tag{2.51}$$

Result (2.51) also holds for semi-infinite media and slab geometry. The reason is that the sources or sinks are spread all-over the scattering medium. If the medium is optically thick, the contribution of the bulk outweighs the surface effects. Inside the bulk of the medium (further than few mean free paths from the interfaces) the above calculation for the C_0 effect holds because its origin is local (decaying in the scale of one mean free path) and does not sense the presence of interfaces.

CHAPTER 3

Essentials of random-matrix theory for the Anderson transition

The goal of this chapter is to introduce the basics of random matrix theory to the general audience, with an emphasis on experimental observations. It is not possible to assess the strengths and shortcomings of a formalism without understanding its basic assumptions. To be able to describe what general and specific assumptions are made in this framework, we derive some of its elementary, yet far-reaching, statistical predictions. Despite the apparently loose justification of these assumptions, the predictions are often generally applicable and surprisingly successful in reproducing the experimental results, even for very complicated systems. Similar to the previous chapter, our intension is to overview the basic concepts as much as needed for the new derivations that are presented in the final sections of this chapter. Our final results are based on the perturbation method for almost diagonal matrices. The outcome of these calculations will be compared in chapter 4 with direct numerical diagonalization of related matrices. The rest of the statistical predictions or statement will be, here and there, referred to when experimental results are discussed.

For most of the introductory material in this chapter, the author is highly indebted to the course of Random Matrix Theory [13] instructed by professor Carlo Beenakker in the framework of Delta Institute for Theoretical Physics (DITP).

3.1 A short history of RMT

In contrast to the multiple-scattering formalism, which was said to be the reductionist approach to studying waves in disordered media, random matrix theory (RMT) is a holistic approach. In a RMT treatment, one often overlooks all the details of the system under investigation. These matrices are either representing the Hamiltonian of a (mesoscopic) quantum system or the scattering matrix[1] of a disordered barrier. These matrices con-

---

[1] Since their introduction by John Archibald Wheeler and Werner Heisenberg the concept of scattering matrices or S-matrices have been used by various disciplines other than high-energy particle physics. These matrices are closely related, but not identical, to transition matrices. When adapted to the monochromatic scattering theory the concepts of scattering and transition matrices become a bit confusing and the subject

tain all the information for describing one specific realization, but as we mentioned in the previous chapter, only averages or statistical distributions are really useful results. The main assumption of RMT is the invariance of these statistical properties under continuous transformation of the matrix if the "background features" are conserved. These background features include matrix symmetries and domain of definition. This assumption rarely fails if the investigated system is disordered enough. The transformed matrix can well be one with random entries, with just a few constraints imposed. The main body of the calculus in Random Matrix Theory deals with extracting diverse properties (most notably, statistics or correlations of matrix eigenvalues) of matrices with entries drawn randomly from various probability distributions. All these various disordered systems are classified into few corresponding random matrix ensembles.

The original proposal of this approach goes back to the works by Wigner, Dyson, Mehta and Guadin in the 1960s. A historical overview can be found in the book of Mehta [88]. Random matrix theory has since developed into a powerful quantitative tool for several fields of physics and a source of inspiration for mathematicians. The start of the field is usually attributed to highly influential papers by Eugene Wigner [145, 146], motivated by applications in nuclear Physics. Wigner suggested that fluctuations in spacing between compound nuclei resonances can be described in terms of statistical properties of eigenvalues of very large real symmetric matrices with independent, identically distributed entries. The rational behind such a proposal was to look at the corresponding systems as "black boxes" and adopt a kind of statistical description, not unlike thermodynamics approach to classical matter. This idea was justifiably the single resolution in the situation when it is hardly possible to understand individual spectra associated with any given nucleus composed of many strongly interacting quantum particles. In section 3.4.1 we shall see the simplest derivation of this level-spacing distribution, which leads to the celebrated Wigner's surmise.

Despite the surprising success of RMT in predicting quantitative results, its application is sometimes criticized because of the lacking connection with the microscopic description of the system. The interest in RMT saw a revival in 1990's after the connection was made with quantum chaotic systems, and conductance fluctuations in disordered metals. This connection is used for describing several experimental results in mesoscopic quantum transport, which has become measurable amid the advances in nanoscience. Meanwhile, it has also inspired several experiments on classical waves like sound, light, and microwaves. The advantage of classical wave experiments is in their unsurpassable precision, high degree of control and versatile design opportunities, in comparison with low temperature electronic transport measurement. On this path, original ideas have merged in describing purely optical phenomena such as random lasers and grey body radiation [15]. Furthermore, RMT has become closest than ever to real life applications by the advances in opaque lenses [135] and the emergence of information age for optics [131].

3.2 Wigner-Dyson ensembles

The omnipotence of random matrix theory lies on two fundamental assumptions, which will be discussed in the following two paragraphs. There assumptions are not easily acceptable for a critical mind, but once swallowed will pave the way for the unexpect success in

---

of interesting discussions. In this dissertation, we use the scattering matrix term for a unitary matrix that connects the scattering channels connected to an elastic scatterer, but does not explicitly contain a delta function in frequency (or energy).

providing a series of quantitative prediction. Like any other statistical formalism, one has to start with the probability distribution. For the moment, we consider the space of all Hermitian matrices of equal size and common background features, the definition of which should become clear in a few lines. These matrices can be diagonalized by a controlled (unitary) transformation. The first assumption states that the probability of picking a specific matrix in this space is just a function of its spectrum, $\{E_i\}$,

$$P(H) = f(\{E_i\}). \tag{3.1}$$

It means that the eigenvectors (which constitute the transformation matrix to the diagonal representation) are irrelevant for the probability of picking H. This probability can now be transformed from the matrix space to the eigenvalue space by inserting the correct Jacobian

$$P(\{E_i\}) = f(\{E_i\}) \prod_{i<j} |E_j - E_i|^{\beta}, \tag{3.2}$$

where β is an integer number signifying the symmetry of the random matrix ensemble. This joint probability distribution describes the eigenvalue repulsion. The second central assumption of RMT requires that all the correlations between the eigenvalues are due to the Jacobian and $f(\{E_i\})$ induced no correlation:

$$f(\{E_i\}) = \prod f(E_i). \tag{3.3}$$

A widely used example is the Gaussian ensemble where

$$f(E) = e^{-cE^2}. \tag{3.4}$$

The choice of Gaussian distribution is not at all a fundamental requirement for RMT, but becomes very handy since the matrix elements become independently distributed. By using the property $\mathrm{Tr}H^2 = \sum_{ij} H_{ij}^2$ for any Hermitian matrix, the probability of picking matrix H reads

$$P(H) \propto e^{-c\mathrm{Tr}H^2} = \prod_{ij} e^{-cH_{ij}^2}. \tag{3.5}$$

This characteristic is often recalled as independent identical distribution (IID) of the matrix elements. As an important example where such a constraint cannot be imposed, we will later discuss the ensemble of unitary matrices.

3.2.1 Hamiltonians

One broad category of systems, which is studied using RMT, consists of non-dissipative closed systems. Examples are electronic wavefunctions in small metal grains or trajectories in chaotic billiards. In quantum mechanics such a system is characterized by a self-adjoint linear operator in the Hilbert space; its Hamiltonian. This Hamiltonian is often represented as a Hermitian matrix, which may even be infinitely large. The only important parameters for RMT are background features such as the matrix entries being real or complex values, the time-inversion invariance, or other symmetries a Hamiltonian may hold.

Aimed at describing the resonance energies of heavy nuclei, which are the eigenvalues of its Hamiltonian, three random matrix ensembles were defined by Dyson, based on Wigner's proposal. The classical Wigner-Dyson ensembles are the Gaussian Orthogonal Ensemble (GOE), the Gaussian Unitary Ensemble (GUE) and the Gaussian Symplectic Ensemble

(GSE). They are composed, respectively, of real symmetric, complex Hermitian and complex self-adjoint quaternion matrices. The matrix entries are IID with zero mean, and their variances are adjusted to ensure the invariance of their joint probability density with respect to Orthogonal (respectively, Unitary or Symplectic) similarity transformations. Note that the name of the ensemble is chosen after the characteristic of the transformation matrix rather than the Hamiltonian itself. The values of exponent β, which appeared in the Jacobian in Eq. (3.2) are 1, 2, and 4 for these three ensembles, In physics, GUE corresponds to Hamiltonians with broken time-reversal and GSE describes those with no spin-rotation symmetry.

3.2.2 Scattering matrices

Another category of matrices often used to describe a physical system consists of scattering matrices. They connect the incoming and outgoing propagation channels connected to a scatterer. Experimentally, these are even more relevant than Hamiltonians. A Hamiltonian generally describes a disconnected and closed system. In experiments, one is often probing the system from outside. In fact, Hamiltonians as rarely used to describe multiple scattering of classical waves because in practice it is very difficult to realize a fully closed system. The scattering picture is also very relevant for quantum transport measurements where the wiring plays the role of input and output channels. In general terms the scattering matrix is defined as

$$\psi^{\text{out}} = S\psi^{\text{in}} \tag{3.6}$$

where the upper indices indicate to the incoming or outgoing directions in a relevant complete basis. For waveguide and slab geometries or two-contact transport measurements, for which front and back of the sample are clearly distinguished, it is customary to write the scattering matrix in the following block format

$$\begin{pmatrix} \psi_a^- \\ \psi_b^+ \end{pmatrix} = \begin{pmatrix} r & t \\ t' & r' \end{pmatrix} \begin{pmatrix} \psi_a^+ \\ \psi_b^- \end{pmatrix}, \tag{3.7}$$

where the lower indices denote the front or back of the sample or label the electrodes. The plus or minus indices indicate to the direction of current or energy flow. Each block is a square matrix and the t block is usually called the transmission matrix.

Elastic scattering is described by a unitary matrix. The ensemble of unitary random matrices was suggested by Dyson, long before they were really used to describe scattering. He introduced these ensembles to relax the statistical independence constraint on matrix elements in Gaussian ensembles. As was mentioned before, statistical independence is a handy by generally unnecessary restriction for random matrix arguments. These ensembles were called circular because their eigenvalues are confined to the unit circle in the complex plane. By imposing the similar constraints as their Gaussian counterparts, these ensembles are coded as the Circular Orthogonal Ensemble (COE), the Circular Unitary Ensemble (CUE) and the Circular Symplectic Ensemble (CSE).

3.3 Unconventional ensembles

Real physical systems are rarely described by matrices that are consisted of statistically independent entries. On the contrary, they are often strongly correlated. However, for most physical observables of interest, only the symmetries matter. This is the major success factor for RMT. The successful implication of RMT methods in condensed matter physics motivated a fundamental revision of the conventional classification. This revision was also meant to include some of the widely applied Hamiltonians in the formalism. For example those describing superconductors or quarks do not have the symmetries of any classical Wigner-Dyson ensemble.

A major advancement was due to the work of Efetov [41] built upon the earlier ideas of Wegner. He showed how to approximately map the problem of calculating disorder averages of products of amplitude Green functions for a single particle in a random potential on a supersymmetric nonlinear σ-model. The same nonlinear σ-models can be used to describe the conventional random matrix ensembles in the limit of large matrix sizes. By developing this formalism, he made a major step in relating RMT to the microscopic description of disorder. Efetov's method have since been applied to several transport problems and motivated condensed matter and high energy physicists to study each others calculations. This unprecedented proximity has lead to the solution of several long-standing problems that were outside the range of all previous methods.

The successes of nonlinear supersymmetric σ-model has also inspired mathematicians in their rigorous treatment of ergodic operators in spectral theory. Zirnbauer has diagnosed the method in the perspective of Cartan's symmetric spaces defined in the representation theory [149]. He presented an extended classification of random matrix theories based on the symmetric spaces. Several physical systems are then classified in this scheme, which is conjectured to exhaust all possible universality classes in disordered single particle (non-interacting) systems and none else will be found [3, 110].

Another advancing front for using the concept of RMT in modeling physical systems has been set by defining specific matrices for describing "toy models". Although, these models are sometimes too specific to be classified in the universal scope of RMT, this front has also reached outstanding successes in recent years [21]. One example is the non-Hermitian disordered tight-binding model by Hatano and Nelson [62], which shows a delocalization transition. Their model was motivated by its application to a special mapping of flux lines in certain superconductors to a bosonic system with a random potential.

In the rest of this section we review some properties of the ensemble of banded random Hermitian matrices, which has recently attracted a lot of attention due to its success in describing several phenomena related to Anderson localization. Then, we introduce a new class of non-Hermitian random matrices that fully describe the propagation of polarization waves on a chain of scatterers with dipole interactions. The mapping of this model on the real physical system is exact and it can hardly be called a toy model. The scaling properties of the latter model is exploited in chapter 4, using numerical analysis.

3.3.1 Banded matrices

A lot of recent developments in RMT has been motivated by the efforts for understanding Anderson localization transition in disordered medium. Anderson localization in electronic systems is extensively studied in the form of the Anderson tight-binding Hamiltonian with on-site disorder [72].

$$H_{ij} = \sum_i E_i \left|i\right\rangle \left\langle i\right| + \sum_{<ij>} \left|i\right\rangle \left\langle j\right| , \tag{3.8}$$

where the index i points to the isolated energy states and the second summation goes over the nearest neighboring energy sites on a lattice. The on-site energies are randomly selected from a box distribution in $[-\frac{W}{2}, \frac{W}{2}]$ For this model all states are exponentially-localized in one and two dimensions. In three-dimensional space there exists a metal-insulator transition at $W = 16.5$. This behavior is in accordance with the single parameter scaling theory [1, 101]. Despite the success of applying statistical physics methods to the 2-d problem, no analytical treatment has been put forward for solving the Anderson model in 3-d. All the current theoretical understanding is based on the perturbation expansion for $2 + \epsilon$ dimension built upon the 2-d solution. Information for the 3-d system has been extracted mostly from numerical analysis. The localization behavior of the Anderson model changes by introducing long range interaction between sites. Anderson points out to this fact already in his original "absense of diffusion" article by restricting the potential (coupling between energy sites) to decay faster than $1/r^3$ [7].

Numerous models with long-range hoping have been built on top of the Anderson model to study delocaliztion transition. Among the most successful efforts was the introduction of the ensemble of power-law banded random matrices (PLBRM). It was introduced and systematically studied by Mirlin et. al. [93].

The introduction of PLBRM allowed for the effects of the Anderson localization to be correctly incorporated at the level of random matrix theory. Transition from localized to extended eigenstates has been analytically proven in the PLBRM ensemble for both weak and strong coupling. In these Hermitian random matrices the off-diagonal elements decay as $\langle |H_{ij}|^2 \rangle = (b/|i-j|)^{2\mu}$ for $|i-j| > b$, where b is called the bandwidth. All eigenvectors are localized for $\mu > 1$, the tight-binding limit, and are extended (metallic) for $\mu < 1$, as in the conventional Wigner-Dyson random matrices. At $\mu = 1$, eigenstates show critical statistics for any width of the band. Because of the common characteristic behavior between this ensemble and 3-d Anderson model, PLBRM has attracted a lot of attention in recent years.

A closely related Hamiltonian was previously suggested by Levitov [79] to describe localization of vibrational modes in a disordered lattice in presence of dipole-dipole interactions. The interaction potential was annexed in the form of $D_{ij} \propto |\mathbf{r}_i - \mathbf{r}_j|^{-\mu}$ to the Anderson model. He showed that for $\mu > d$, where d is the dimensionality of space, all states remain localized. For $\mu < d$ all states escape localization due to a diverging number of resonances between spectrally apart energy levels. For $\mu = d$, delocalization is weak and states are critical. An ingenious mapping on this model was used by Al'tshuler and Levitov [5] to solve the scattering of charged particle from a disordered target of charged atoms considering the Coloumb interactions. They have adopted the creative title of "Weak chaos in a quantum Kepler problem" for their article, in contrast to a Sinai billiard that is fully chaotic. In their model, localization is shown to prevail in the momentum space instead of position, which means that the particle momentum will stay bounded in certain limits instead of diffusing. This was a clear illustration that the spatial extent of wavefunction is not always a good indicator of Anderson localization.

The modern treatment of PLBRM model in the weak-coupling regime is partly based on the Levitov's method. A mathematically rigorous foundation has been laid by Kravtsov and Yevtushenko, upon which on can now apply this method to a variety of almost diagonal matrices. It has been dubbed the method of Virial expansion, since the influence of coupled resonances is ordered by the number of involved states. This method has been since applied to several matrix ensembles [53, 74, 96]. We have used the method to solve a new class of non-Hermitian matrices, which are important for describing the collective excitation modes in a chain of scatterers coupled by dipole-dipole interactions.

3.3.2 Complex-symmetric matrices

Most of the models in condensed matter physics concentrate on Hamiltonians or unitary scattering matrices. Meanwhile, Green matrices emerge as a new class of random matrices, which deal with several problems in atomic physics and optics. The entries of these Euclidean matrices are the pairwise Green functions that connect a collection of points in space, hence the name Euclidean. This collection forms an ordered or disordered cloud in space after putting a point-like polarizable scatterer on each point. Examples for such a system are atom gases on resonance [9] or collections of metallic nanoparticles [123]. Motivated by the advances in nano-fabrication, this models have also become relevant for describing many artificially made systems like plasmonic metamaterial structures or antenna arrays [6, 70, 141]. Despite this wide range of applications, these matrices have not yet been well studied in the mathematical framework of RMT. The only relevant available system is the Gnibre ensemble of complex matrices, which removes the restriction of Hermiticity from the convensional Wigner-Dyson classes. However, the conditions of Green matrices being complex-symmetric and Euclidean, are both relaxed in the Gnibre ensemble. Very recently, Green matrix ensembles have been systematically studied by analytic tools such as self-consistent analysis of the resolvent [58] in ordered to describe physical phenomena such as Dicke supperradiance and random lasers [118].

Since Green matrices are non-Hermitian, their eigenvalues are complex. The eigenvectors form a complete (bi-orthogonal) basis, unless the matrix is defective. Defective matrices form a subset of measure zero for a randomly generated ensemble. The orthogonality condition is set by the quasi-scalar product of each two distinct eigenvectors:

$$\langle \bar{\psi}_m | \, \psi_n \rangle \equiv \sum_i \psi_m(x_i) \psi_n(x_i) = 0, \tag{3.9}$$

where $|\psi_n\rangle$ is a right eigenvector of $\mathcal{M}$; $\mathcal{M}\,|\psi_n\rangle = \varepsilon_n\,|\psi_n\rangle$. Because of the symmetry in the Green matrix, there is a one-to-one relation between the left and right eigenvectors. As a choice, the eigenvectors are normalized to unity: $\langle \psi_n | \, \psi_n \rangle = 1$. The quasi-scalar product of an eigenvector with itself is a non-zero complex number for non-defective matrices.

3.4 Statistical probes in simulations and experiments

As we have emphasized several times in the previous pages, any quantitative analysis of a disordered medium has a statistical side to it. That is why in the mathematical treatments of this sort, all results are probabilistic and often accompanied by the phrase “almost surely”. In this respect, RMT is an ideal tool for providing quantitative predictions and suggesting certain experimental or numerical measures. Most of the possible RMT calculations are on the eigenvalues and their correlations. However, in certain cases, eigenfunctions have also been studied for example to investigate their critical scaling behavior.

In the rest of this section, we review a few of these probes and predictions that are more relevant to the study of classical waves in disordered systems. We present some basic derivation of these quantities just to give a flavor of how a random matrix treatment looks like. These derivations are among the simplest examples and yet are very insightful as they can cover several experimental situations.

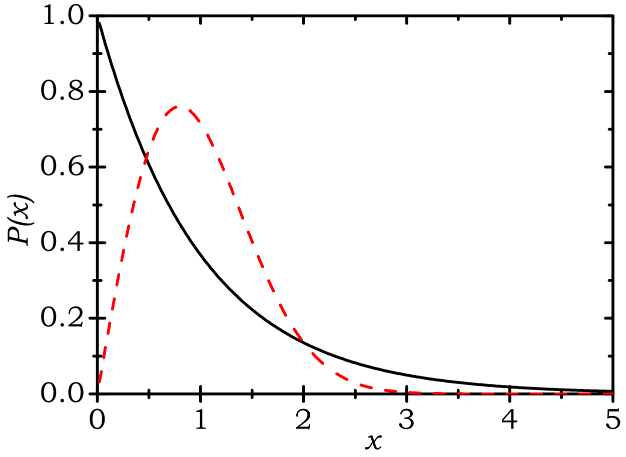

Figure 3.1: The distribution of eigenvalue spacing for the GOE ensemble of random matrices is very close to the Wigner surmise (dashed line). In the localized regime the eigenvalues are not interacting and their spacing follows the Poisson distribution (full line).

3.4.1 Level-spacing distribution

The distribution of separations between successive eigenvalues is perhaps one of the first and yet very outreaching predictions of RMT. The huge datasets available from neutron scattering experiments in the 1950's made it possible to draw the precise distribution of energy level spacings. However, theoretical predictions were missing at the time. It was Wigner who guessed the following distribution, nowadays known as Wigner's surmise:

$$P(x) = \frac{\pi x}{2} e^{-\frac{1}{4}\pi x^2}, \tag{3.10}$$

with $x = \frac{|s|}{\Delta}$ the level spacing divided by its average. It turned out to be a remarkably good description for the observed data. Later, it was found out that Wigner's formula is not exact for any random matrix from GOE but the variation from the exact calculation is merely around 2%. Similar forms can describe GUE and GSE level spacing distributions, with the prefactor proportional to s^β. Equation (3.10) is exact for an ensemble of 2×2 real symmetric matrices H with a Gaussian distribution of the independent matrix elements:

$$P(H) \propto e^{-c(H_{11}^2 + H_{22}^2 + 2H_{12}^2)}, \tag{3.11}$$

where c is an arbitrary constant. Hereby we shall go through this derivation just to present a simple example for a RMT computation.

Since H is real and symmetric, it can be diagonalized by an orthogonal transformation:

$$\begin{pmatrix} H_{11} & H_{12} \\ H_{21} & H_{22} \end{pmatrix} = \begin{pmatrix} \cos\theta & \sin\theta \\ -\sin\theta & \cos\theta \end{pmatrix} \begin{pmatrix} E + \frac{s}{2} & 0 \\ 0 & E - \frac{s}{2} \end{pmatrix} \begin{pmatrix} \cos\theta & -\sin\theta \\ \sin\theta & \cos\theta \end{pmatrix}, \tag{3.12}$$

with the transformation Jacobian

$$J(E, s, \theta) \equiv \frac{\partial(H_{11}, H_{12}, H_{22})}{\partial(E, s, \theta)} = s, \tag{3.13}$$

By using this Jacobian and the invariance of $\sum H_{ij}^2$ under orthogonal transformation, we can now write the joint probability distribution

$$P(E, s, \theta) = A|s|e^{-c(2E^2+\frac{s^2}{2})}, \tag{3.14}$$

with A the normalization factor. The dependence on E and θ can be integrated out. The resulting probability for the level spacing reads

$$P(s) = c|s|e^{-c\frac{s^2}{2}}, \tag{3.15}$$

with mean value $\Delta \equiv \langle |s| \rangle = \sqrt{\frac{\pi}{2c}}$. After putting back this average in Eq. (3.15), we read out the Wigner surmise of Eq. (3.10).

The experimental significance of the Wigner's distribution becomes more evident when it is contrasted with the distribution of level spacing in a localized system. In such a system, eigenfunctions have negligible overlap and pose no correlation (repulsion) between the adjacent eigenvalues. Thereby, eigenenergies are randomly distributed. In the case of random distribution of eigenvalues with a mean spacing of Δ, one can write the probability of having a spacing s as

$$P(s)ds = \lim_{m\to\infty} \left(1 - \frac{s}{m\Delta}\right)^m \frac{ds}{\Delta} = e^{-\frac{s}{\Delta}} \frac{ds}{\Delta}. \tag{3.16}$$

This construction can be pictured as sectioning the spacing s into m equal parts, multiplying the probabilities of *not* finding a level in any of those intervals with the probability of finding one in the last interval with a size of ds, and taking the limit of m to infinity. This is the usual path for deriving the so-called Poisson distribution

$$P(x) = e^{-x}. \tag{3.17}$$

The poisson distribution is compared with the Wigner's surmise for GOE in Fig. 3.1. The evident difference can be a very convincing experimental probe for the delocalization transition. However, as said before, measuring the isolated energy levels of a closed system with proper resolution is often an insurmountable challenge for the experiments. Therefor, many observations have focused on studying the properties of scattering matrices, which is the topic of the following section.

3.4.2 Open transmission channels

Scattering matrices for elastic scatterers are unitary by definition. In a transport configuration, the eigenvalues of the matrix product $t^\dagger t$ are taken as the transmission coefficients T_i of the eigenmodes of the system. These "modes" are the columns or rows of the matrices that result from a singular value decomposition of the full scattering matrix, and can be used as a basis for describing any scattering event. Once again, the fundamental assumption of RMT implies that the correlation between the eigenvalues is solely due to the Jacobian $\prod_{i<j} |T_j - T_i|^\beta$ from matrix elements to eigenvalues. This "geometric" correlation leads to the eigenvalue repulsion. The probability distribution of the transmission coefficients $P(\{T_i\})$ can be pictures in the form of a partition function for a Gibbs gas at temperature β^{-1} on a line with a logarithmic repulsion $u(T_i, T_j) = -\ln|T_i - T_j|$ between the classical particles at positions $x_i = T_i$.

For the eigenvalues of transmission matrices, unlike the energy levels of a Hamiltonian, there is the extra constraint $0 \leq T_i \leq 1$ imposed by the unitarity. Due to the eigenvalue repulsion, they are pushed against these bounds and the final distribution has a bimodal form. For the CUE ensemble, which for example describes the transport of electrons through a quantum dot in presence of magnetic field, this bimodal distribution in symmetric around $\frac{1}{2}$ and has the form

$$\rho(T) = \frac{N}{\pi}\frac{1}{\sqrt{T}\sqrt{1-T}}, \tag{3.18}$$

with N the total number of channels. The easy way to prove this result is to take this distribution as an ansatz, integrate the interaction potential $u(T-T')$ weighted by this density at point T' and show the result is invariant with respect to T. This distribution is slightly different from the other bimodal distribution of eigenvalues for a quasi one-dimensional system such as a wire:

$$\rho(T) = \frac{N\ell}{2L}\frac{1}{T\sqrt{1-T}}, \tag{3.19}$$

with length L and mean free path ℓ. The latter result is obtained from the Dorokhov-Mello-Pereyra-Kumar (DMPK) equation [37, 89], which takes into account the evolution of the eigenvalue distribution with the increasing wire length. This equation will be presented in the following section.

The bimodal distribution of transmission eigenvalues is rather surprising and has far reaching consequences. Of special interest are those eigenmodes with almost unity transmission. Their mere existence means that given enough control on the incident channels, one can completely circumvent the disordered structure and transport the whole wave energy without any backscattering. Evidence for this counter-intuitive phenomenon has been recently shown by Vellekoop and Mosk [136], using their invention of wave-front shaping.

3.4.3 Anderson localization in waveguide geometry

Picking the scattering matrix from the CUE ensemble is an over-simplified picture for describing the wave transport through a disordered wire or waveguide. In such a system, one has to take into account the dependence of the transmission probability distribution on the increasing length of the system. This can be done either by using the supersymmetric σ-model approach [40, 92] or by using the DMPK equation [14]. In the latter method, the evolution of the probability distribution with the increasing length of the wire is written in the form of a multi-variate advection-diffusion equation, with the length L playing the role of time. The drift is caused by the added randomness in the incremental length and the interaction is due to the Jacobian. In its derivation, only up to the second moment of correlation between transmission eigenvalues is considered to be important. It is more convenient to write the equation in terms of $\{x_i\}$, which are called the Lyapunov exponents and are related to $\{T_i\}$ by $T_i = \cosh^{-2} x_i$. For the conventional Wigner-Dyson classes, the DMPK is given by

$$\frac{\partial}{\partial L}P(\{x_i\};L) = \frac{1}{2\gamma\ell}\sum_{i=1}^{N}\frac{\partial}{\partial x_i}\left(\frac{\partial P}{\partial x_i} + \beta P\frac{\partial \Omega}{\partial x_i}\right), \tag{3.20}$$

$$\Omega = -\sum_{j=1}^{N}\sum_{k=j+1}^{N}\ln|\sinh^2 x_j - \sinh^2 x_k| - \frac{1}{\beta}\sum_{j=1}^{N}\ln|\sinh^2 2x_j| \tag{3.21}$$

with $\gamma = \beta N + 2 - \beta$ and N the number of modes propagating in the wire or in the waveguide. The DMPK method provides detailed information about the eigenvalue distribution for arbitrary number of channels, unlike the diffusive σ-model that requires $N \gg 1$.

Although, the solution to the DMPK equation has been found for any arbitrary length [16], it is more straightforward to start from the long-wire limit. In this case, the wire becomes insulating. The x_i's have then diffused far apart with a separation much larger than unity; $1 \ll x_1 \ll x_2 \ll \cdots \ll x_N$. One can thus approximate the hyperbolic sine function in Eq. (3.20) by an exponential. As a result, all the variables in the DMPK equation decouple and each of them can be found by solving the following Fokker-Planck equation:

$$\frac{\partial P(x_i, L)}{\partial L} = \frac{1}{2\gamma\ell}\frac{\partial^2 P}{\partial x_i^2} - \frac{1}{\xi_i}\frac{\partial P}{\partial x_i}, \tag{3.22}$$

with $\xi_i = [1 + \beta(i-1)]/\gamma\ell$ the localization length of the i-th mode. The solutions have the following Gaussian form

$$P(x_i) \propto e^{-\frac{\gamma\ell}{2L}\left(x_i - \frac{L}{\xi_b}\right)^2}, \tag{3.23}$$

In the limit of a long wire, the conductance is given by the smallest Lyapunov exponent and decreases exponentially with the length $g_D \propto e^{-L/\xi_1}$ with ξ_1 the localization length. Distribution (3.23) means that the dimensionless conductance of the long wire follows a log-normal distribution with the following average and variance:

$$\langle \ln g_D \rangle = -\frac{2L}{\gamma\ell}, \tag{3.24}$$

$$\mathrm{var}(\ln g_D) = \frac{4L}{\gamma\ell}. \tag{3.25}$$

The equidistance distribution of the Lyapunov exponents in the long and localizing wires persists in the metallic regime as well, for $L < \xi$. Therefore, the Lyapunov exponents have always a uniform density $\rho(x) = NL/l$ for $0 < x < L/l$. Transforming this result to the eigenvalue distribution will result in the bimodal form of Eq. (3.19).

Equation (3.24) has a very important consequence for experiments, which is often overlooked. The variance of log-conductance is twice its average. The distribution of the conductance itself will be then much broader in shape, which means that one should expect largely fluctuating conductances in the localized regime when the realization is changes. As a result, larger statistics must be collected in comparison with usual Gaussian distributed parameters. Furthermore, the Thouless criterion $g_D = 1$ is a blurred indicator for the localization threshold. Relying on the dimensionless conductance for determination of the localization transition threshold can be misleading if the collected statistics is not large enough.

For circumventing this restriction, Garcia and Genack has suggested to use another statistical measure for the transition threshold. Their parameter $\mathrm{var}(S_a)$ is in average equal to the Thouless conductance g_D but is self-averaging at the same time: has a Gaussian distribution. S_a the total transmission of the disordered waveguide normalized by its average. The average and variance are taken over several realizations. As a second advantage, this parameter relaxes the condition of measuring the conductance in absolute terms. By using this parameter, Chabanov et. al were able to put a conclusive, practical and quantitative criterion for the localization crossover in a disordered microwave waveguide [28].

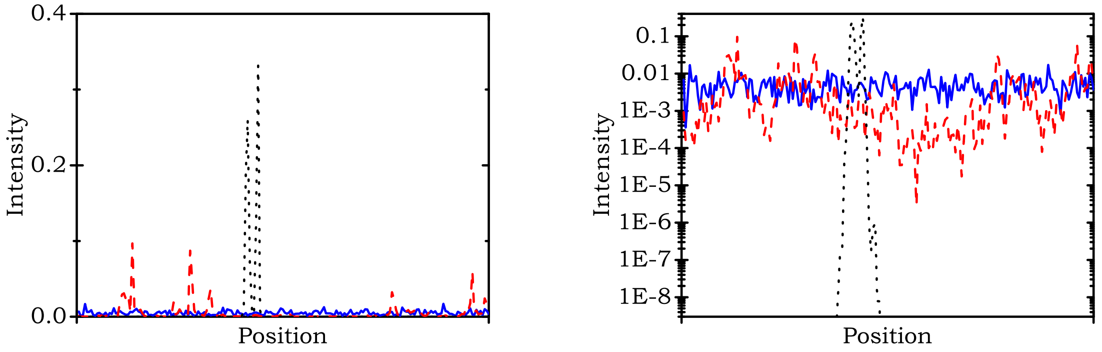

Figure 3.2: Typical intensity distribution of eigenfunctions in metallic (solid line), insulating (dotted line) and critical (dashed line) regimes. Left: linear scale, Right: semi-logarithmic scale. The critical wavefunctions are recognized by their large fluctuations and non-localized spread.

3.4.4 Eigenfuntion statistics and Anderson localization

In three-dimensional disordered systems the transition from the insulating to the the metallic regimes emerges as a true phase transition. The phase transition also occurs for other dimensionalities when certain symmetries are broken or long range interactions and disorder correlations are present [43]. Close to the Anderson transition, wavefunctions show critical statistical behavior. These critical states are peculiar for their spatial structure that is multifractal [10, 43, 142]. A typical eigenfunction in the critical regime is plotted in Fig. 3.2 and compared with eigenfunctions in localized or extended regimes. The illustrated examples are generated using Levitov matrices with different decay exponents μ.

Here, we briefly review some general aspects of MF and their implications in the context of the Anderson transition. Multifractality quantifies the strong fluctuations of the wave function. It shows the non-trivial length-scale dependence of the moments of the intensity distribution. The dependence can be investigated by varying the system size L, or alternatively if the system size is fixed, by dividing the system into small boxes of linear size b and varying the box size. This property is quantified by using the generalized Inverse Participation Ratios (GIPR)

$$P_q = \sum_{i=1}^{n} (I_{B_i})^q = \sum_{i=1}^{n} \left[\int_{B_i} I(\mathbf{r}) d^d\mathbf{r} \right]^q , \tag{3.26}$$

where $I(\mathbf{r})$ is the normalized intensity (equal to $|\psi^2(\mathbf{r})|/\int |\psi^2(\mathbf{r})| d^d r$ where $\psi(\mathbf{r})$ is the wave function) and I_{B_i} is the integrated probability inside a box B_i of linear size b, with $\lambda \ll b \ll L$ where λ is the wavelength. The summation is performed on the whole sample, which consists of $n = (L/b)^d$ boxes, and d is the space dimension. By definition $P_1 \equiv 1$ and $P_0 \equiv n$.

At criticality, the ensemble averaged GIPR, $\langle P_q \rangle$, scales anomalously with the dimensionless scaling length L/b as

$$\langle P_q \rangle \sim (L/b)^{-d(q-1)-\Delta_q} \equiv (L/b)^{-\tau(q)} , \tag{3.27}$$

where $d(q-1)$ and Δ_q are called the normal (Euclidean) dimension and the anomalous exponent, respectively. For a normal (extended) wavefunction, $\Delta_q = 0$ for every q. A (single-) fractal wavefunction with fractal dimension D is described by $\tau(q) = D(q-1)$. For critical states $\tau(q)$ is a continuous function of q that fully describes the MF.

Multifractality can also be derived from the probability density function (PDF) of the logarithm of eigenfunction intensities, for which the GIPR are proportional to its moments. This is easy to check using definition (3.26). In fact, the PDF and GIPR are analogous descriptions of the eigenfunction statistics. Each of them may become handy, dependent on the specific numerical or experimental investigation. This equivalence together with Eq. (3.27) implies the following scaling relation for the PDF:

$$\mathcal{P}(\tilde{\alpha}) \sim (L/b)^{-d+f(\tilde{\alpha})}\,, \text{with } \tilde{\alpha} \equiv \frac{\ln I_B}{\ln \frac{b}{L}}. \tag{3.28}$$

The second term in the exponent, $f(\alpha)$, is called the singularity spectrum, and is related to the set of anomalous exponents $\tau(q)$ by a Legendre transform

$$\tau(q) = q\alpha - f(\alpha), \quad q = f'(\alpha), \quad \alpha = \tau'(q). \tag{3.29}$$

The quantity α introduced here is proportional by an irrelevant scaling prefactor to $\tilde{\alpha}$, which is used in the construction of PDF. However, especially for a skewed PDF, this prefactor can significantly deviate from unity and therefore α and $\tilde{\alpha}$ are not exactly equivalent quantities. This difference is generally not so important for scaling arguments, but one has to deal with it when extracting the singularity spectrum from the numerical or experimental data.

The singularity spectrum $f(\alpha)$ is the fractal dimension of the set of those points $\mathbf{r}$ where the wave-function intensity, $I(\mathbf{r})$, scales as $L^{-\alpha}$. In mathematical terms, it shows the coexistence of several populations of singularities in the measure, which is the wave-function intensity for this specific case. In the field-theoretical treatment of random-Schrödinger Hamiltonians, MF implies the presence of infinitely many relevant operators [38, 98]. The functional dependence of $f(\alpha)$ is an important and unique property of each universality class. In the extended regime, $\mathcal{P}(\ln I_B)$ is strongly peaked near $\alpha = d$, since the short-range fluctuations are washed out in the box integration. First order perturbation theory for an Anderson transition in $2+\epsilon$ dimensions [142] results in the "parabolic approximation" for the MF wave functions [10, 26]. This result, $\Delta_q = \gamma q(1-q)$, corresponds to $f(\alpha) = d - (\alpha - d - \gamma)^2/4\gamma$, where γ is a constant in the order of ϵ. A similar approximation applies to metallic (diffusive) states in three dimensions [4, 48] due to weak localization, although with $\gamma \ll 1$. This is sometimes called weak MF.

Recently, an exact symmetry relation

$$\Delta_q = \Delta_{1-q}, \tag{3.30}$$

was theoretically predicted for the set of anomalous exponents [94]. This symmetry is not trivial at all and has directly observable consequences in the measurement of the eigenfunctions. It relates the probability of finding bright points to the one for dark points. For example, as a result of this symmetry, the eigenfunction intensity cannot be lower than a certain threshold in a finite sample (finding such points has an exponentially vanishing probability). This threshold is set by the size of the sample and the fact that the eigenfunction intensity at one point cannot be larger than one due to normalization. In chapter 5 we will present the experimental verification of this symmetry for ultrasound measurements.

The numerical and analytical investigations of the 3-d Anderson model and certain random matrices suggest that MF may exhibit itself also for off-criticial states on both sides of the transition [32]. The MF concept was extended to the boundaries where it behaves differently with respect to the bulk [126].

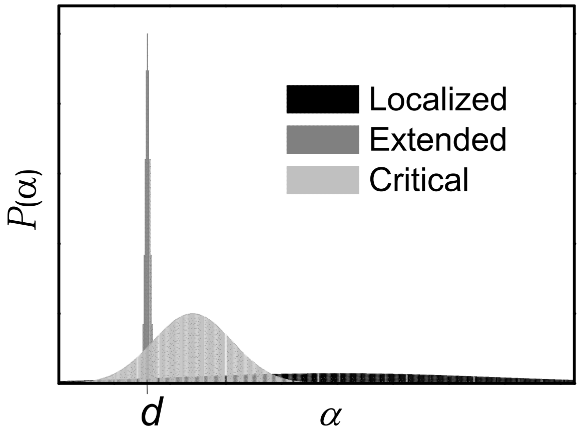

Figure 3.3: The schematic probability distribution function of the log-intensity parameter α for the three regimes of metallic, insulating, and critical.

3.5 Perturbation results for almost-diagonal Green matrices

Finally, after the long introductory review, we will here present our results on the critical behavior in a class of Green matrices. The general properties of these matrices were introduced in Sec. 3.3.2. We now analyze a special case of collective excitation of electromagnetic waves on a periodic chain of dipolar scatterers with site disorder induced due to varying polarizability. The $L \times L$ matrix (with L the number of sites) that fully describes this system has the following form

$$D_{ij} = \delta_{ij} E_i + (\delta_{ij} - 1) g_{ij}, \tag{3.31}$$

with g_{ij} the Green function connecting the points x_i and x_j on the lattice. Here, we consider the linearly decaying Green function, which has the same asymptotic behavior as the full Dyadic Green function for dipole-dipole interaction. The simplification does not change the statistical behavior of interest. The off-diagonal elements are thus given by

$$g_{ij} = \frac{1}{Wk} e^{\imath k|i-j|}, \tag{3.32}$$

with k describing the free-space wavenumber normalized by the periodicity of the lattice and W a measure for the diagonal disorder. Larger value of W means higher degree of disorder and thus smaller coupling. The diagonal elements are distributed uniformly in $[-\frac{1}{2}, \frac{1}{2}]$.

We will show that the eigenvectors of these matrices scale critically with increasing matrix size. The MF properties of the eigenfunctions in the weak coupling regime will be derived by using the perturbation method. Large disorder or weak coupling corresponds to $Wk \gg 1$. In this regime, the density of states is determined only by the distribution of the diagonal elements and hence is uniform. Therefore, we assume that all eigenvectors are characterized by the same scaling exponents and we define the ensemble average GIPR as

$$\langle P_q \rangle \quad = \quad \frac{1}{L} \sum_{n=1}^{L} \sum_{i=1}^{L} |\psi_n(x_i)|^{2q}. \tag{3.33}$$

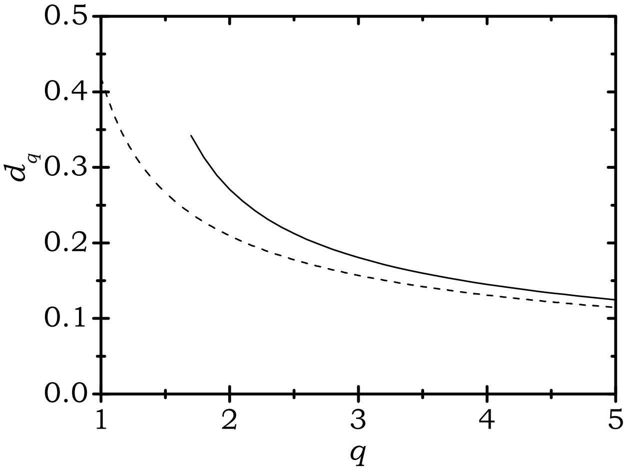

Figure 3.4: Comparison between the singularity spectrum for complex-symmetric Green matrices (solid line) given by Eq. (3.45) and their orthogonal counterpart (dashed line) given by Eq. (3.47).

The moments of the eigenvectors can be extracted from the powers of the diagonal elements of the Green functions and therefore can be computed using the method of virial expansion.

In the lowest order of virial expansion, which corresponds to a pure diagonal matrix, the eigenvectors consists of only one non-zero component and therefore all moments are equal to one due to normalization: $\langle P_q \rangle^{(1)} = 1$.

In the next order of the virial expansion, the contribution to the eigenvectors moments from all possible pairs of two levels of the unperturbed system should be taken into account. Thus we need to calculate the moments of the eigenvectors of the following 2×2 matrices:

$$M(i,j) \quad = \quad \begin{pmatrix} E_i & g_{ij} \\ g_{ji} & E_j \end{pmatrix}, \tag{3.34}$$

Denoting the moments of the second component of the corresponding eigenvectors by $P_q(i,j)$, we have

$$\langle P_q \rangle^{(2)} = \frac{1}{L} \sum_{i \neq j}^{L} (P_q(i,j) - 1) \tag{3.35}$$

The subtraction of 1 in the equation above eliminates the contribution already taken into account in the diagonal approximation.

The off-diagonal element is generally a complex number; $g_{ij} = g_{ji} = h_{ij} e^{\imath \phi_{ij}}$ By the assumption of weak coupling $|h| \ll 1$ and writing the eigenvectors of $M(i,j)$ explicitly, we obtain:

$$\begin{aligned} P_q(i,j) \quad &= \quad \int_{-1/2}^{1/2} dE_1 \int_{-1/2}^{1/2} dE_2 (Q((E_1 - E_2)/h) + Q((E_2 - E_1)/h)), \\ Q(x) \quad &= \quad \left(\frac{4}{4 + \left(x - \sqrt{(x^2 + 4e^{-2\imath\phi}} \right) \left(x - \sqrt{(x^2 + 4e^{2\imath\phi}} \right)} \right)^q . \end{aligned} \tag{3.36}$$

where we have dropped the ij subscripts for simplicity. In the limit $h \to 0$ one can show that $Q(r) = \theta(r)$ and thus $P_q = 1$. This result corresponds to the diagonal approximation and is cancelled by -1 in Eq. (3.35). In order to find first non-trivial contribution, we need to compute a term that is linear in h. To this end, we first differentiate Eq. (3.36) with respect to h, then change the integration variables $\{E_1, E_2\} \to \{E_1, x = (E_1 - E_2)/h\}$ and consider the limit $h \to 0$:

$$\lim_{h\to 0} \frac{dP_q}{dh} = -2\int_{-\infty}^{\infty} dx\, xQ'(x) \equiv -F(q,\phi), \tag{3.37}$$

The expansion of P_q then takes the form:

$$P_q = 1 - |h|F(q,\phi) + O(h^2). \tag{3.38}$$

Collecting the contributions from all the off-diagonal elements we obtain

$$\langle P_q \rangle = 1 - \frac{1}{Wk}\frac{1}{L}\sum_{i\neq j} \frac{F(q, k|i-j|)}{|i-j|}. \tag{3.39}$$

After expanding $F(q,\phi)$ in the Fourier series $F(q,\phi) = \sum_p c_p(q) e^{\imath p\phi}$ we find

$$\begin{aligned} \frac{1}{L}\sum_{i\neq j} \frac{F(q,k|i-j|)}{|i-j|} &= \frac{1}{L}\sum_{i\neq j}\frac{c_0(q)}{|i-j|} + \frac{1}{L}\sum_{i\neq j}\sum_{p\neq 0}\frac{c_p(q)e^{\imath pk|i-j|}}{|i-j|} \\ &= 2c_0(q)\ln L + O(1), \end{aligned} \tag{3.40}$$

The final result for GIPR reads:

$$\langle P_q \rangle = 1 - \frac{2c_0(q)}{Wk}\ln L, \tag{3.41}$$

with

$$c_0(q) = \frac{1}{\pi}\int_0^{2\pi} d\phi \int_{-\infty}^{\infty} dx\, xQ'_x(x,q,\phi), \tag{3.42}$$

and Q defined in Eq. (3.36), which can be written as

$$Q(x,q,\phi) = \left(\frac{4}{4 + \left| x - \sqrt{x^2 + 4e^{-2i\phi}} \right|^2} \right)^q. \tag{3.43}$$

Comparing this result with the scaling of the moments by changing the system size

$$\langle P_q \rangle \propto L^{-d_q(q-1)}, \tag{3.44}$$

we find the expressions for the fractal dimensions

$$d_q = \frac{2c_0(q)}{Wk(q-1)}. \tag{3.45}$$

One can check that in the case of the orthogonal matrices, i.e. when $\phi = 0$, the old result can be reproduced after the change of the variable $x = (2w-1)/\sqrt{w(1-w)}$:

$$\begin{aligned} c_0(q) &= 2\int_{-\infty}^{\infty} dx\, x Q'_x(x,q,0) \\ &= 2\int_0^1 dw\, \frac{q w^{q-3/2}(2w-1)}{\sqrt{1-w}} \\ &= 2\sqrt{\pi}\frac{\Gamma(q-1/2)}{\Gamma(q-1)} \qquad (3.46) \\ d_q(\phi=0) &= \frac{4\sqrt{\pi}}{Wk}\frac{\Gamma(q-1/2)}{\Gamma(q)} \qquad (3.47) \end{aligned}$$

The result for complex-symmetric matrices deviates only slightly from the one for the orthogonal case as can be seen in Fig. 3.4.

3.6 Concluding remarks

In this chapter, we tried to present a brief overview of some the statistical measures that can be useful in studying localization of waves in classical or quantum systems. We also showed some basic examples of how these results are derived in the scope of random matrix theory. The major reason for presenting these results was to emphasize the importance of statistical analysis in the experimental investigation of random media, especially in the context of Anderson localization.

In the following two chapters, we will present two cases were these statistical measures are applied to recognize the presence of localization. In chapter 4, polarization waves on a chain of scatterers are studied by numerical diagonalization of the describing scattering matrices and a regime of critical scaling is revealed. In chapter 5, experimental data on localization of ultrasound have been analyzed in the context of multifractality. This investigation has resulted in the first experimental observation of strong multifractality near the Anderson localization transition [47].

CHAPTER 4

Critical scaling of polarization waves on a heterogeneous chain of scatterers with dipole-dipole interaction

In this chapter, the intensity distribution of electromagnetic polar waves in a chain of near-resonant weakly-coupled scatterers is investigated theoretically and supported by numerical analysis. Critical scaling behavior is discovered for part of the eigenvalue spectrum due to the disorder-induced Anderson transition. This localization transition (in a formally one-dimensional system) is attributed to the long-range dipole-dipole interaction, which decays inverse linearly with distance for polarization perpendicular to the chain. For polarization parallel to the chain, with inverse-squared long-range coupling, all eigenmodes are shown to be localized. A comparison with the results for Hermitian power-law banded random matrices and other intermediate models is presented. This comparison reveals the significance of non-Hermiticity of the model and the periodic modulation of the coupling [46].

Collective excitations of nanoparticle composites have shown promising applications for sensing, nonlinear spectroscopy, and photonic circuits. Among these applications, transport of electromagnetic signal along an assembly of metallic nanoparticles has been the subject of intensive research in recent years. It has shown promising applications in integrated photonics [6], sensing [105], and transfer of quantum information [33] . By the nature of their fabrication, disorder is inevitable in these artificial structures and therefore must be considered accordingly.

In this chapter, we make a connection between the photonic transport in these novel physical structures and the Anderson localization transition. Anderson localization has been investigated in various fields such as condensed matter physics [43], cold gases in optical lattices [11], and classical waves in random media [76]. We argue how the polar excitations in a chain of resonators can show *critical* scaling behavior. This criticality plays a major role in understanding the underlying phase transition phenomena when the system becomes large enough to be considered in the thermodynamic limit. However, one should be careful when trying to link the artificially fabricated model systems with a phase transition since the real structures are always finite in size.

Our model system is fully described by a class of complex-symmetric Euclidean coupling matrices. The eigenvectors of these matrices describe the excitation "modes" of the chain of point-like scatterers. These scatterers are driven close to resonance and are coupled to each other through long-range dipole-dipole interaction.

Using direct numerical diagonalization of the matrices, we have studied this system in two cases of weak and strong coupling. By studying the scaling behavior of eigenstates in the weak coupling regime, we show that for transverse magnetic (TM) polarization parallel to the chain direction, all the states are localized. For the transverse electromagnetic (TEM) polarization in this regime, some of the states are critically extended and their scaling is described by a multifractal spectrum. We analytically derive a perturbation expression for this multifractal spectrum in the limit of weak coupling corresponding to large disorder. In the strong coupling regime, we show some numerical evidence that the intensity distribution follows a mixed phase of localized and extended statistics.

We have extensively compared the scaling behavior of this physical system with several hypothetic Hermitian and non-Hermitian matrix ensembles. This comparison proves the strong influence of the phase periodicity in the coupling terms. As a test, we study an ensemble similar to the Levitov matrices with $\mu = 1$, which were introduced in the previous chapter, Sec. 3.3.1. While we keep the Hermiticity, the main difference we impose is for the off-diagonal terms that are considered to be non-random and have a periodic phase relation. We show that the eigenvector of these matrices are no longer critical, but localized. On the other hand, the critical behavior of TEM polar eigenmodes, which we report for the complex-symmetric ensemble, disappears if the interaction phase factor is chosen randomly.

Our findings provide a clear and universal framework for excitation properties of an important building block in modern photonics. On a broader perspective our model has significant resemblance with the other important classes of Hamiltonians, which are used for describing several transport phenomena in mesoscopic systems. Since our model has an exact correspondence to a real physical system, it will pave the way for experimental investigation of several theoretical findings, which up to now were bound to the limitations of numerical simulation.

4.1 The model

For describing the chain of resonators, we use the dipole approximation for each of the scatterers and the full dyadic on-shell Green function for their interaction. This model is previously used for describing collective plasmon excitations of metallic nanoparticles on a line or a plane for periodic [70, 141], aperiodic [51] and disordered configurations [86]. In particular, Markel and Sarychev have reported signatures of localization in a chain of point-like scatterers [87].

The presence of an Anderson transition, its critical behavior, and the detailed statistics of localized or delocalized modes in such a system has not yet been studied. In the following, we will argue and show analytically that a disorder-mediated delocalization transition can happen for polarization perpendicular to the chain direction (TEM modes), while for polarization parallel to the chain direction (TM modes), all eigenstates are localized in a long enough chain. We will present our results using a well-established statistical framework of probability density function (PDF) of eigenmode intensities and the scaling of generalized inverse participation ratios (GIPR).

4.1.1 Dipole chain model

We consider a linear array of L equally spaced polarizable isotropic particles with an inter-particle distance of s. The size of the particles are considered small enough, relative to both s and the excitation wavelength $\lambda \equiv 2\pi c/\omega$, for a point-dipole approximation to be valid. With these considerations, TEM and TM modes are decoupled from each other. For the stationary response, oscillating with constant frequency ω, the dipole moments of particles $p_i \equiv \hat{\mathbf{u}}.\mathbf{p}_i$ projected on each mode, are the solutions to the following homogeneous set of linear equations

$$p_i(x_i) = a_i(\omega)\left[E^{\mathrm{in}}(x_i) + \sum_{j\neq i} g_\omega\left(|x_i - x_j|\right) p_j(x_j)\right], \tag{4.1}$$

where a_i is the polarizability of the ith particle and $e^{\imath\omega t}E^{\mathrm{in}}(x_i)$ is the incident electric field at its position projected on the specific Cartesian coordinate of the mode, $\hat{\mathbf{u}}$. The free space Green function g_ω should be replaced by the proper expressions for TEM($\perp$) and TM($\|$) modes, which are given by

$$\begin{aligned} g_\omega^{\perp}(x) &= \frac{1}{4\pi\epsilon}\left(\frac{\omega^2}{c^2 x} + \frac{\imath\omega}{c x^2} - \frac{1}{x^3}\right) e^{\imath\omega x/c}, \qquad (4.2)\\ g_\omega^{\|}(x) &= \frac{-1}{2\pi\epsilon}\left(\frac{\imath\omega}{c x^2} - \frac{1}{x^3}\right) e^{\imath\omega x/c}, \qquad (4.3)\end{aligned}$$

Equation (4.1) can be represented in its matrix form $\mathcal{M}\left|p\right\rangle = \left|E^{\mathrm{in}}\right\rangle$ where

$$\mathcal{M}_{ij} = \delta_{ij} a_i^{-1} + (\delta_{ij} - 1) g_\omega(|x_i - x_j|). \tag{4.4}$$

The explicit frequency dependence of a_i is dropped, since we consider only monochromatic excitations in this work. The matrix $\mathcal{M}$ is a complex and symmetric matrix, the inverse of which gives the polarization response of the system to an arbitrary excitation; $\left|p\right\rangle = \mathcal{M}^{-1}\left|E^{\mathrm{in}}\right\rangle$. In fact $\mathcal{M}^{-1}$ is the t-matrix of the chain specified on the lattice points. Since $\mathcal{M}$ is non-Hermitian, its eigenvalues are complex. The properties of complex-symmetric matrices was reviewed in section 3.3.2. The orthogonality condition is set by the quasi-scalar product of each two eigenvectors:

$$\left\langle \bar{\psi}_m \middle| \psi_n \right\rangle \equiv \sum_i \psi_m(x_i)\psi_n(x_i) = 0, \tag{4.5}$$

where $\left|\psi_n\right\rangle$ is a right eigenvector of $\mathcal{M}$; $\mathcal{M}\left|\psi_n\right\rangle = \varepsilon_n \left|\psi_n\right\rangle$. The eigenvectors are normalized to unity: $\left\langle \psi_n \middle| \psi_n \right\rangle = 1$.

Under the stated assumptions, the polarization response to an incident field can be obtained from the decomposition

$$\left|p\right\rangle = \sum_n \frac{\left|\psi_n\right\rangle \left\langle \bar{\psi}_n \middle| E^{\mathrm{in}} \right\rangle}{\varepsilon_n \left\langle \bar{\psi}_n \middle| \psi_n \right\rangle}. \tag{4.6}$$

A null eigenvalue points to a collective resonance of the system and the corresponding eigenvector is the most bound (guided) mode with the highest polarizability.

4.1.2 Resonant point scatterer

A simple and yet general model for the dipolar polarizability of a point scatterer that conserves energy [36] is given by

$$\frac{1}{a} = \frac{1}{4\pi\epsilon}\left(\frac{1}{a^{\mathrm{D}}} - \frac{2\imath\omega^3}{3c^3}\right), \tag{4.7}$$

where the last term in Eq. (4.7) is the first non-vanishing radiative correction that fulfils the optical theorem. The quasi-static polarizability a^{D} depends on the particle shape and its material properties. For a Lorentzian resonance around ω_R

$$\frac{1}{a^{\mathrm{D}}} = \frac{A}{V}\left(1 - \frac{\omega^2 + \imath\gamma\omega}{\omega_R^2}\right), \tag{4.8}$$

where V is the volume of the scatterer, γ is the Ohmic damping factor, and A is a constant that depends only on the geometry of the scatterer. For elastic scatterers, a^{D} is real-valued and diverges on resonance.

4.1.3 Dimensionless formulation

To study the properties of the coupling matrix (4.4) both theoretically and numerically, we rewrite it in terms of dimensionless quantities by dividing all the length dimensions by the interparticle distance s and multiplying the unit of polarizability by $4\pi\epsilon k^3$, where $k = \omega/c$. For the cases considered in this chapter, we also neglect the Ohmic damping of scatterers and hence the imaginary part on the diagonal of the matrix is given by the radiative damping term in Eq. (4.7).

Based on definition (4.4), two distinct types of disorder can be considered for the system under investigation. Pure off-diagonal disorder is caused by the variation in the interparticle spacing considering identical scatterers. The contrary case of diagonal disorder applies when the particles are positioned periodically but have inhomogeneous shapes or different resonance frequencies. For the sake of brevity, we limit our discussion to the case of pure diagonal disorder. All the techniques used in this chapter are also applicable in presence of off-diagonal disorder.

In the units described before, the off-diagonal elements of $\mathcal{M}$ are written as

$$D^{\perp}_{i\neq j} \equiv \left(-\frac{1}{k|i-j|} - \frac{\imath}{(k|i-j|)^2} + \frac{1}{(k|i-j|)^3}\right)e^{\imath k|i-j|}, \tag{4.9}$$

$$D^{\parallel}_{i\neq j} \equiv 2\left(\frac{\imath}{(k|i-j|)^2} - \frac{1}{(k|i-j|)^3}\right)e^{\imath k|i-j|}, \tag{4.10}$$

for TEM and TM excitations, respectively.

Since the Ohmic damping is taken out and the lowest order radiation damping is independent of the particle geometry, the diagonal elements are inhomogeneous only in their real parts. We choose the real part from the the set of random numbers $U(-W/2, W/2)$, which has a box probability distribution around zero with a width W. The imaginary part of the diagonal elements is constant in these units and equals $-2\imath/3$. Considering the linear dependence of the inverse of polarizability (4.8) on the particle volume and detuning from resonance frequency, realizing a uniform distribution is practical.

4.1.4 Hypothetic models

The results of the perturbation approximation disagrees with some of the trends observed in our numerical results for weakly coupled systems. To shed light on the origin of these observations, we have performed similar statistical analysis on extra hypothetical models. In these four models, step by step, we transform our model for TEM excitation to an ensemble of orthogonal random matrices, for which extensive results have been reported in the literature (see Ref. [43] for a recent review). In all these ensembles the diagonal elements are real random numbers selected from the set $U(-W/2, W/2)$. The distinction is in the off-diagonal elements which are defined as follows:

H0, The matrices in this model are orthogonal and they are the closest to the frequently used PLRBM ensemble. The offdiagonal elements are random real numbers given by

$$D^{\mathrm{H0}}_{i\neq j} \equiv \frac{h_{ij}}{k|i-j|}, \tag{4.11}$$

where h_{ij} is a randomly chosen from $U(-1,1)$; i.e. uniformly distributed in [-1,1].

H1, These matrices are the Hermitian counterpart of the TEM coupling matrix with a randomized phase factor for each element:

$$\begin{aligned} D^{\mathrm{H1}}_{i<j} &\equiv D^{\perp}_{ij} e^{\imath\phi_{ij}}, \\ D^{\mathrm{H1}}_{i>j} &\equiv \bar{D}^{\perp}_{ij} e^{-\imath\phi_{ji}}, \end{aligned} \tag{4.12}$$

where $\phi_{i<j}$ is a random number from $U(-\pi,\pi)$.

C1, This ensemble of complex-symmetric matrices resembles the TEM model with a randomized coupling phase.

$$D^{\mathrm{C1}}_{ij} \equiv D^{\perp}_{ij} e^{\imath\phi_{ij}}, \tag{4.13}$$

where $\phi_{ij} \equiv \phi_{ji}$ are random numbers from $U(-\pi,\pi)$.

H2, This model is based on the Hermitian form of TEM interaction and the phase factor is kept periodically varying.

$$\begin{aligned} D^{\mathrm{H2}}_{i<j} &\equiv D^{\perp}_{ij}, \\ D^{\mathrm{H2}}_{i>j} &\equiv \bar{D}^{\perp}_{ij}. \end{aligned} \tag{4.14}$$

4.2 Analytical probes

Decomposition (4.6) relates the overall statistical behavior of the system to the properties of the eigenmodes and their corresponding eigenvalues. The dipole chain is an open system and the excitations are subject to radiation losses, which lead to the exponential decay of a mode. Therefor it is not possible to distinguish between disorder and loss origins of localization only based on the spatial extent of a mode. For these types of systems, statistical analysis has shown to be the only unambiguous method of studying Anderson transition. Therefor we study the scaling behavior. For this analysis, based on the eigenvectors in the position basis, two important indicators are considered: 1-the probability distribution function (PDF) of the wavefunction intensities and 2-the generalized inverse participation ratios (GIPR).

The PDF is more easily accessible in experiments [71]. For numerical analysis, it has proven to be an accurate tool for measuring the scaling exponent in a finite size system [107] and extracting the critical exponent from finite size scaling analysis [108]. With the parametrization $\mathcal{P}(\tilde{\alpha}; W, L, b)$, the PDF is sufficient for characterizing an Anderson transition. Here, $\tilde{\alpha} \equiv \ln I_B / \ln(b/L)$ with $I_B \equiv \sum_{i=1}^{b} |\psi_n(x_i)|^2$ the integrated intensity over any box selection of length b. The effective disorder strength is parameterized by W, but the exact definition depends on the model. Criticality of eigenfunctions demands the scale invariance of the PDF. It means that the functional form of $\mathcal{P}$ does not change with system size for a fixed b/L. Away from the transition point, the maximum of the PDF, $\tilde{\alpha}_m$, exhibits finite size scaling behavior [108]. This maximum shifts to higher(lower) values at the localized(extended) side of the transition.

Another widely used set of quantities for evaluating the scaling exponents is the set of GIPR, which are proportional to the moments of the PDF. For each wavefunction GIPR are defined as

$$P_q(\{\psi_n\}) \equiv \sum_{i=1}^{L} |\psi_n(x_i)|^{2q} . \tag{4.15}$$

At criticality, the ensemble averaged GIPR, $\langle P_q \rangle$, scales anomalously with the length L as

$$\langle P_q \rangle \sim L^{-d_q(q-1)}, \tag{4.16}$$

where d_q is called the anomalous dimension. For multifractal wavefunctions, which are characteristic of Anderson transitions, d_q is a continuous function of q. From the definition, $P_1 = 1$ and $P_0 = L$. In practice, the GIPR can also be evaluated by box-scaling for a single system size, given a large enough sample [134].

4.2.1 Perturbation results for the weak-coupling regime

In the regime of weak coupling $Wk \gg 1$ the off-diagonal matrix elements of the Hamiltonian are small compared to the diagonal ones. Therefore the moments of the eigenfunctions can be computed perturbatively using the method of the virial expansion, which was introduced in section 3.5. We find that TEM eigenfunctions scale critically with the length of the system. The criticality is set by the inverse linear interaction term in Eq. (4.9) which dominates at large distances. In the weak-coupling regime, the set of multifractal exponents can be explicitly calculated. The result is different from the universal one found for all critical models with Hermitian random matrices [53] and is given by

$$d_q = \frac{2c_0(q)}{Wk(q-1)}, \quad q > \frac{1}{2}. \tag{4.17}$$

with the explicit expression for $c_0(q)$ is given by Eq. (3.42). The corresponding result for the orthogonal matrices reads

$$d_q = \frac{4\sqrt{\pi}\Gamma(q-1/2)}{Wk\Gamma(q)}, \quad q > \frac{1}{2}. \tag{4.18}$$

If a similar analysis is performed on the TM eigenfunction, the GIPR converge at large system sizes implying that the eigenfunctions are localized. This is due to the r^{-2} behavior of the coupling at large distances.

In the following section, an extensive comparison is made between these analytical expressions and the numerical simulations.

4.3 Numerical results

By direct diagonalization of a large ensemble of matrices, we have studied the PDF and GIPR scaling of the eigenfunctions of matrices from all the models introduced in the previous sections. Several values of disorder strength W and carrier wavenumber k are considered for matrices with sizes from $L = 2^7$ to 2^{12}. Each matrix is numerically diagonalized with MATLAB using the ZGGEV algorithm. The number of analyzed eigenfunctions for each set of parameters is around 10^4. Computation time for diagonalization of the largest matrix is 20 minutes on a PC.

4.3.1 Spectrum of the homogeneous chain

We start by calculating the spectrum of the homogenous infinite chain on resonance (W=0) where all the diagonal element are given by $\mathcal{M}_{ii} = 0 - 2\imath/3$. As an example we provide the analytic expression for the TEM modes and then we discuss further based on the numerical results, which for our discussion on a finite system are more relevant.

As the infinite system is translationally invariant, the eigenvectors are simply plane waves $\psi_q(x) = e^{\imath qx}$, with the corresponding eigenvalues ε_q given by the Fourier transform of the Green function

$$
\begin{aligned}
\varepsilon_q &= \sum_{x=-\infty}^{\infty} -g(|x|)e^{\imath qx} \\
&= \sum_{x=1}^{\infty} \left(-\frac{1}{kx} - \frac{i}{k^2x^2} + \frac{1}{k^3x^3}\right) e^{\imath kx} \left(e^{\imath qx} + e^{-\imath qx}\right) \\
&= -\frac{1}{k}\left[\mathrm{Li}_1\left(e^{\imath(k+q)}\right) + \mathrm{Li}_1\left(e^{\imath(k-q)}\right)\right] - \frac{i}{k^2}\left[\mathrm{Li}_2\left(e^{\imath(k+q)}\right) + \mathrm{Li}_2\left(e^{\imath(k-q)}\right)\right] + \\
&\quad \frac{1}{k^3}\left[\mathrm{Li}_3\left(e^{\imath(k+q)}\right) + \mathrm{Li}_3\left(e^{\imath(k-q)}\right)\right],
\end{aligned}
\tag{4.19}
$$

where the polylogarithm function $\mathrm{Li}_s(z)$ is defined as

$$
\mathrm{Li}_s(z) = \sum_{j=1}^{\infty} \frac{z^j}{j^s}. \tag{4.20}
$$

The spectra for a finite chain is slightly deformed with respect to its counterpart for the infinite chain, but the overall behavior can be captured for $L > 100$. Typical spectra for TEM and TM excitations in a finite chain are shown in Figures 4.1(a) and (d) for $k = 1$.

For $k < 1.4$, the TEM eigenvalues are divided into almost-real and complex subsets. The almost-real ($\mathrm{Im}\,\varepsilon \ll \mathrm{Re}\,\varepsilon$) subset corresponds to subradiative (bound) eigenstates. These eigenstates have a wavelength shorter than the free space propagation[70, 141] and cannot couple to the outgoing radiation, except at the two ends of the chain. The eigenmodes corresponding to complex eigenvalues ($\mathrm{Im}\,\varepsilon \sim \mathrm{Re}\,\varepsilon$) are superradiative. For these modes a constructive interference in the far-field enhances the scattering from each particle in comparison with the an isolated one.

From the form of expansion (4.6) it is clear the eigenstates with (close to) zero eigenvalues will dominate the response of the system to external excitation. However, different regions in the spectrum can be experimentally probed by two approaches: Firstly, by changing the lattice spacing, or secondly, by detuning from the resonance frequency, which will add a constant real number to the diagonal of the interaction matrix $\mathcal{M}$. Close to the

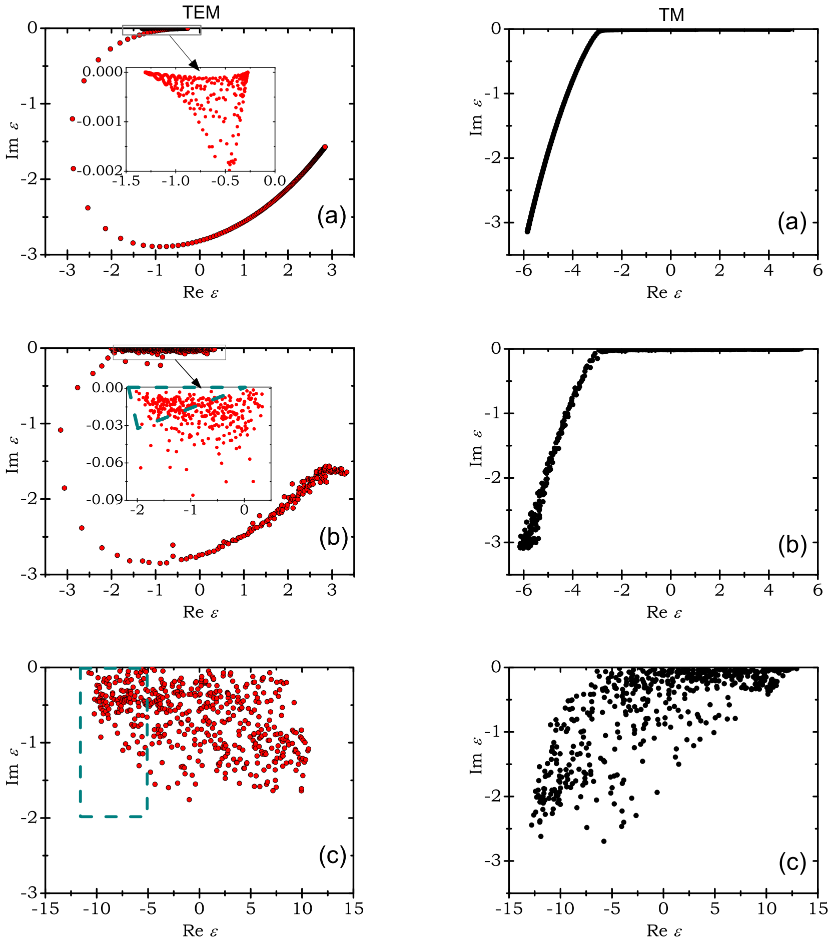

Figure 4.1: Left column: complex valued spectrum of the TEM interaction matrix (4.9) with $k = 1$ for (a) homogeneous ($W = 0$) and disordered in regimes of (b) strong ($W = 2$) and (c) weak ($W = 20$) coupling. The dashed square in (c) shows the region where the corresponding TEM eigenmodes are scaling critically. The eigenmodes corresponding to the eigenvalues in the dashed regions are selected for further statistical analysis. Right column: same as the left for TM polarization.

resonance this number is linearly proportional to the frequency variation. This shift results in driving a different collective excitation, which has obtained the closest eigenvalue to the origin of the complex plane.

4.3.2 The effect of disorder

As mentioned before, disorder is introduced to the system by adding random numbers from the interval $[-W/2, W/2]$ to the diagonal of $\mathcal{M}$. With this setting, the parameter space has two coordinates W and k, and $g = (Wk)^{-1}$ is the coupling parameter. The weak and strong coupling regimes correspond to $g \ll 1$ and $g \approx \mathcal{O}(1)$ respectively. For $k < 0.5$ the short range behavior is dominated by the quasi-static part of the interaction. The eigenstates of the disordered chain are thus exponentially decaying –similar to localized states. Since we are mainly interested in the critical behavior of eigenfunctions we focus on the region with $0.5 < k < 3$.

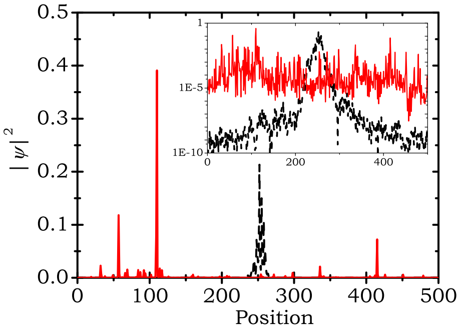

Figure 4.2: Typical TEM critical (red solid line) and TM localized (black dashed line) eigenvectors of matrices defined in section 4.1.3 with $k = 1$ and $W = 10$. The inset shows the same plot in logarithmic scale.

Small disorder

In the intermediate and strong coupling regime, the spectrum of the disordered matrix keeps the overall form of the homogeneous case (where the real part of the diagonal is zero), as can be seen in Fig. 4.1(b).

At the sub-radiative band-edge of the TEM spectrum, modes of different nature mix due to disorder. This region is magnified in the inset of Fig. 4.1(b). The eigenmodes corresponding to this region are of hybrid character. They consist of separate localization centers that are coupled via extended tails of considerable weight. The typical size of each localized section is longer than the interparticle spacing. Similar modes have been observed in a quasi-static investigation of two-dimensional planar composites[125]. For one-dimensional systems they are sometimes called necklace states in the literature [19, 103]. Heuristically, this behavior can be attributed to the disorder induced mixing of sub-radiative and super-radiative modes which have closeby eigenvalues in the complex plain. Further evidence for this mixed behavior will be later discussed based on the shape of PDF in section 4.3.3.

For TM polarization all of the eigenstates become exponentially localized with power-law decaying tails. The localization length increases towards the band center. Therefore, in a chain with finite length, one will see two crossovers in the first Brillouin zone, from localized to extended and back. However, the nature of localization seems to be different at the two ends. The subradiative modes ($\mathrm{Im}\,\varepsilon \ll \mathrm{Re}\,\varepsilon$) are localizaed due to interference effects similar to the Anderson localization while the superradiative modes ($\mathrm{Im}\,\varepsilon \sim \mathrm{Re}\,\varepsilon$) are localized by radiation losses. These two crossover regions eventually approach each other and disappear as the amount of disorder is increased, leading to a fully localized spectrum of eigenmodes. The spectral behavior is more complicated for higher wavenumbers with $k > \pi$ but a discussion on that is further than the scope of this chapter.

Large disorder

In the weak coupling regime, the matrix is almost diagonal and thus the eigenvalues just follow the distribution of the diagonal elements. Typical eigenstates are shown in Fig. 4.2. As will be shown later, for this regime, all the eigenstates for TEM and TM are localized (since the coupling is weak) except for a band (about 20% width) of TEM eigenstates with

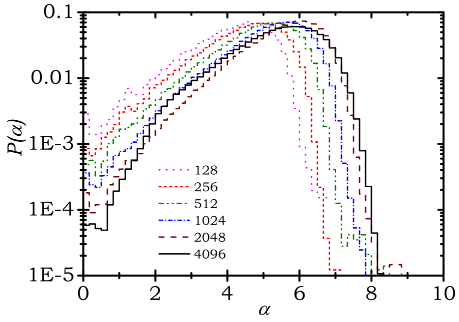

Figure 4.3: Scaling of PDF for TM eigenmodes for different lengths of the chain and correspondingly scaled box sizes of $b = 2^{-6} \times L$. Different line types (and colors) correspond to different system sizes as indicated by the legend. $W = 30$ and $k = 1$. The shift of the peak to the larger values of $\tilde{\alpha}$ indicates that the eigenmodes are localized.

the most negative real part of their eigenvalues. The states in this band show multifractal (critically extended) behavior for any arbitrarily weak coupling. Existence of these states is one of the major results of this investigation and their statistical analysis is the main subject of interest in the rest of this chapter.

The multifractality of eigenfunction in the weak coupling regime is inline with the prediction of the virial expansion result (4.17). However our theory cannot describe why only a part of the TEM eigenstates are critically extended and the rest of them are evidently localized, according to the numerical results.

4.3.3 Scaling behavior of PDF

The scaling of PDF is an effective tool for analyzing the localized to extended transition in sample with finite length [107, 108, 111]. We also use this statistical indicator to distinguish the regions of critical scaling. Only those eigenmodes for which their scaled PDF for different system sizes overlap are critical. For the wavefunctions that fulfill this criteria, the scaling of GIPR is analyzed. This second analysis confirms the presence of critical behavior by checking the the power-law scaling behavior. The logarithmic slope gives the multifractal dimensions. We have preformed extensive survey of the size-scaling behavior of PDF over the W, k space with 10^4 eigenfunctions for each configuration.

For each system size the scaled PDF is approximated by a histogram $\mathcal{P}(\ln I_B / \ln(b/L))$ over the sampled eigenfunctions These histograms are shown in Figures 4.3 to 4.6 for different models. The shift of the peak of the distribution toward larger values (higher density of darker points) by an increase in the system size is a signature of eigenmode localization. A shift in the opposite direction towards a Gaussian distribution with a peak at $\tilde{\alpha}_m = d = 1$ is characteristic of the extended states. Overlap of these histograms signifies the critical behavior of the eigenmodes.

TM and TEM modes in the weak coupling regime

The typical scaling of PDF for TM modes is shown in Fig. 4.3. It clearly reveals the localized behavior of these eigenfunctions. This is the generic behavior observed for these modes at any point in the parameter space. This result is in agreement with the Levitov's prediction,

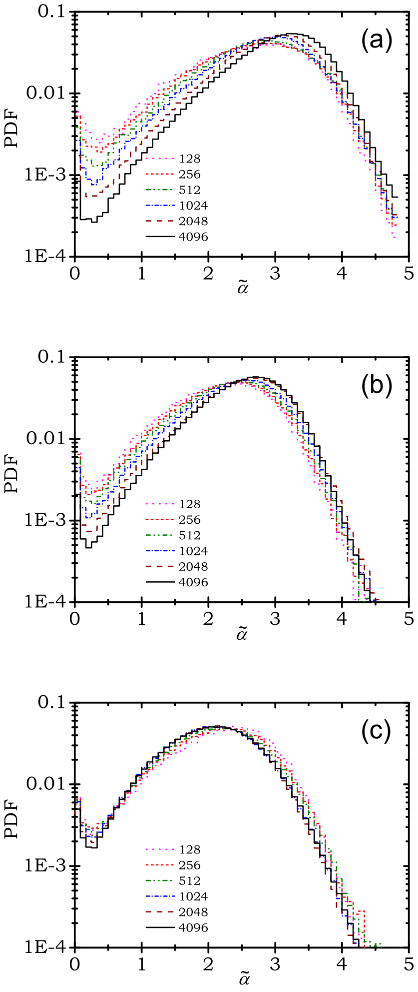

Figure 4.4: Same as Fig. 4.3 for TEM eigenmodes. For each figure 12% of the eigenmodes are used with (a) most positive, (b) closest to zero, and (c) most negative real part of their eigenvalues. Critical scaling is only observed in (c). The shift in the peak of the distribution shows that the rest of the eigenmodes are localized.

since the coupling is decaying as r^{-2}. Localization in disordered one-dimensional systems has already been studied extensively and we do not discuss it further here.

In the regime of weak coupling, $Wk > 10$, the numerical results show convincing indication of critical scaling in a band of the TEM modes. These results are plotted in Fig. 4.4. The band of critical modes consists of those with the most negative real part of their eigenvalues. Outside this band, the eigenfunctions show scaling behavior similar to localized modes as shown in Fig. 4.4(a) and (b). This crossover from localized to critical eigenfunctions may be useful for measuring the critical exponent. However, critical exponent must be defined based on a proper ordering of eigenvalues, which is known to be a non-trivial task for complex eigenvalues.

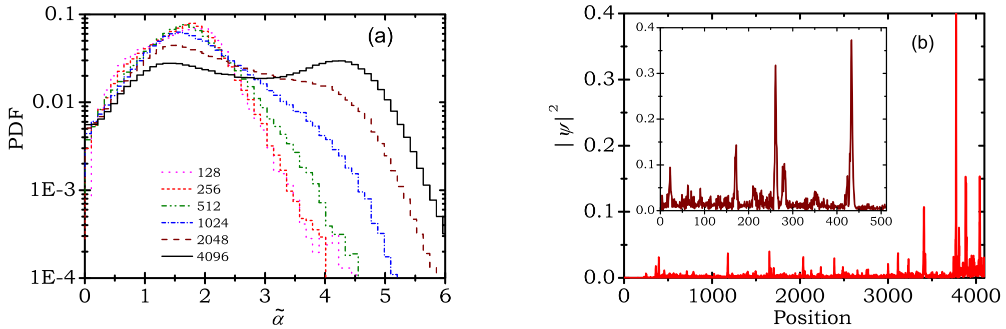

Figure 4.5: (a) Similar to Fig. 4.3 for TEM modes in the regime of strong coupling with $k = 1$ and $W = 0.7$. The analyzed eigenmodes are selected from the spectral region indicated by the dashed triangle in Fig. 4.1(b). (b) Typical eigenmodes used for the PDF in right for two system lengths $L = 4096$ and $L = 512$ (inset).

TEM modes in the strong coupling regime

In the strong coupling regime, i.e. weak disorder, we have found it more representative to order the complex eigenvalues by their argument. A narrow region near the negative real axis is selected as shown in Fig. 4.1(b). The histograms representing the scaled PDF of these eigenfunctions are plotted in Fig. 4.5(a). These histograms do not overlap so the criticality cannot be verified. Meanwhile, the behavior is neither representative of the localized modes nor the extended modes. It appears that the overall extent of the state is comparable with the system size even for the longest chain, but it has an strongly fluctuating internal structure, similar to critical states. Typical eigenmodes of this regime are shown in Fig. 4.5(b). Since the scaled PDF histograms do not overlap, we cannot prove the multifractal nature of the states with a formal logarithmic scaling. Describing the true nature of these modes and their statistical behavior needs further theoretical modeling.

PDF of the intermediate models

The results of the perturbation calculations in section 4.2.1 are insensitive to the details of the model. Therefore they cannot describe some of our observations that are based on direct numerical diagonalization. For example, according to the perturbation theory, all the TEM modes in the weak coupling regime must be critical. This prediction does not agree with the simulation results since PDF scaling in observed for only part of these modes. The same numerical analysis on Hermitian random banded matrices perfectly matches the results of perturbation results.

To further explore the origin of this deviation for complex-symmetric matrices of our model for TEM excitations, we have performed the same numerical procedures on the hypothetic models introduced in section 4.1.4. The PDF scaling graphs for these models are depicted in Fig. 4.6. All these results are for the regime of weak coupling with the same W and k.

H0, The matrices in this model are orthogonal and they are the closest to the frequently used PLRBM ensemble with an interaction decay exponent $\mu = 1$. The PDF shows perfect scaling as depicted in Fig. 4.6(a). The statistics is obtained by sampling

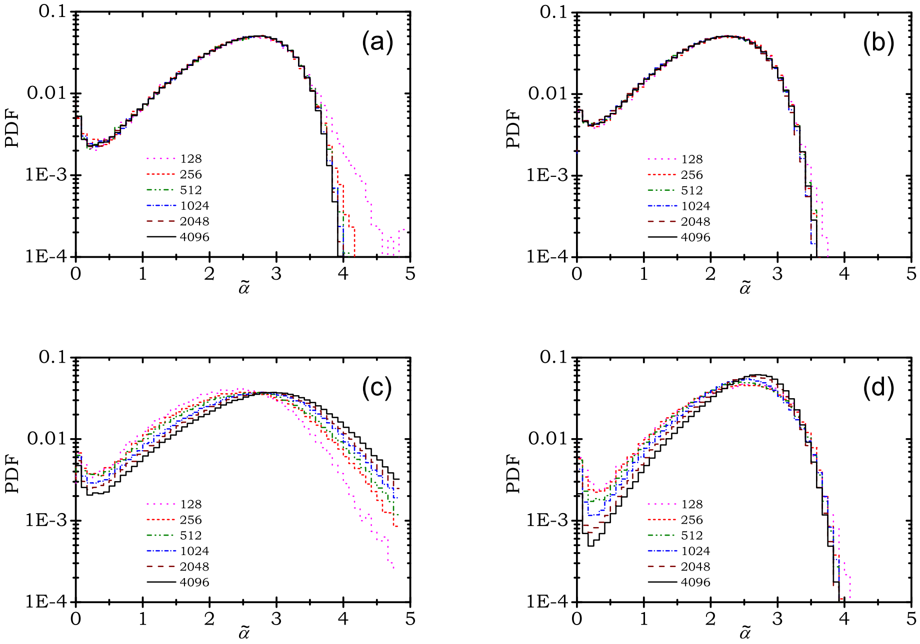

Figure 4.6: Similar to Fig. 4.3 for models (a) H0, (b) H1, (c) H2, and (d) C1. Critical scaling is observed for H0 and H1 models. The eigenvectors of the H2 and C1 models are localized. These models are defined in Sec. 4.1.4.

from 12% of the eigenvectors at the band center, with eigenvalues closest to zero. The analysis shows the same critical behavior (not shown) for the two ends of the spectrum. These results also confirm that our choice of numerical precision and sampling is sufficient for the essential conclusions we get.

H1, These matrices are also Hermitian like model H0. The magnitude of the off-diagonal elements is not random, but follows the decay profile of TEM complex-valued coupling (4.9). Only the phase is randomized. Critical scaling of the eigenfunctions is again evident from the PDF scaling depicted in Fig. 4.6(b).

C1, This ensemble of complex-symmetric matrices resembles the TEM model. The phases of the off-diagonal elements are randomized like the model H1. The finite-size scaling of PDF, depicted in Fig. 4.6(c) shows the behavior that is attributed to localized modes. For localized eigenvectors the peak of the distribution shifts toward higher values of α, which signifies a higher density for points with a low intensity.

H2, This model is the Hermitian counterpart of TEM coupling matrix. The difference between this model and H1 is in the phase factor, which is kept periodic like the original Green function. The only random elements of these matrices are the diagonal ones. Despite the minor difference between models H1 and H2, the result of PDF scaling analysis is completely different. These results are depicted in Fig. 4.6(d) and show that the eigenvectors are localized. This observation is inconsistent with the perturbation theory, which predicts critical behavior for this model like H0 and H1. Note that the considered periodicity for the interaction phase $k = 1$ is incommensurate with the periodicity of the lattice, which equals 2π in our redefinition of units.

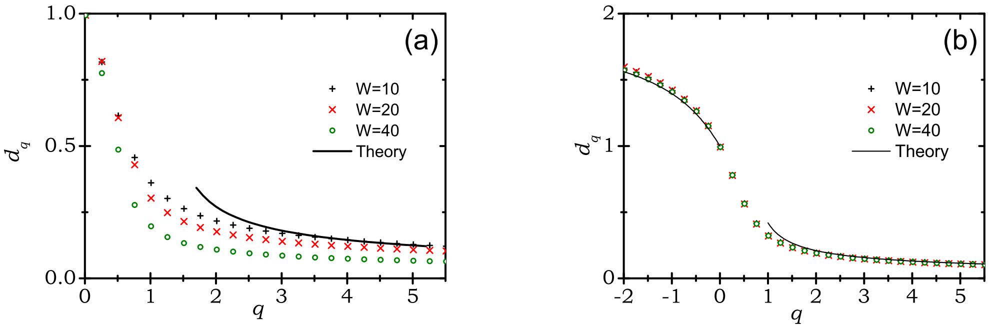

Figure 4.7: The anomalous dimensions d_q (symbols) at a fixed coupling strength for (a) TEM critical modes and (b) Hermitian matrices H1 are compared with the corresponding results (solid line) (4.17) and (4.18) from perturbation analysis. For Hermitian matrices, the symmetry relation predicted in Ref. [94] is used for plotting the theoretical curve at negative q. The errors estimated from the least squares fitting routine are smaller than the symbol sizes and are not shown. The largest error in d_q for point $q = 5.5$ on the graph is ± 0.02.

4.3.4 Multifractal analysis

Since the critical scaling of part of the TEM eigenmodes in the weak coupling regime is clearly observed in the scaling of PDF, we apply generic techniques of multifractal (MF) analysis to quantify the MF spectrum and compare it with our theoretical results. We have used both size scaling and box scaling methods for extracting the scaling exponents of GIPR for several different parameters. We do not observe significant differences in the results of either method (comparison not shown). Therefore, due to its faster computation, we use the box scaling analysis on the largest system sizes, $L = 4096$, to extract the anomalous exponents d_q for several values of W and k. A summary of these results for different values of disorder strength is depicted in Figures 4.7 and 4.8. To show the precision of the numerical analysis, we have also performed this analysis for Hermitian model H1. The results are shown in Fig. 4.7(b) and compared with the theoretical prediction of Eq. (4.18). Excellent matching between theory and simulation is evident for the Hermitian case. However, for the complex-symmetric matrices (corresponding to TEM coupling) the numerical results show significant deviations from the prediction of perturbation analysis, indicating that the first order virial expansion is insufficient for describing that model.

In particular, according to Eq. (4.17), d_q has to be proportional to the coupling strength $g \equiv (Wk)^{-1}$ in the weak coupling regime. The results of direct diagonalization show, in contrast, a dependence of d_q on W at a fixed value of g. This fact can be seen in Fig. 4.7(a). The numerical results are systematically lower than the theoretical prediction for $k < 3$.

Furthermore, the dependence of MF dimensions on the coupling strength is checked for $9 \leq Wk \leq 150$. The results are shown in Fig. 4.8 for $k = 1$ and $k = 3$. The overall inverse linear behavior is observed for $Wk > 30$. But the quantitative correspondence between the numerical results and prediction (4.17) from perturbation analysis is only met for the large values of k and high moments of GIPR, $q > 3$.

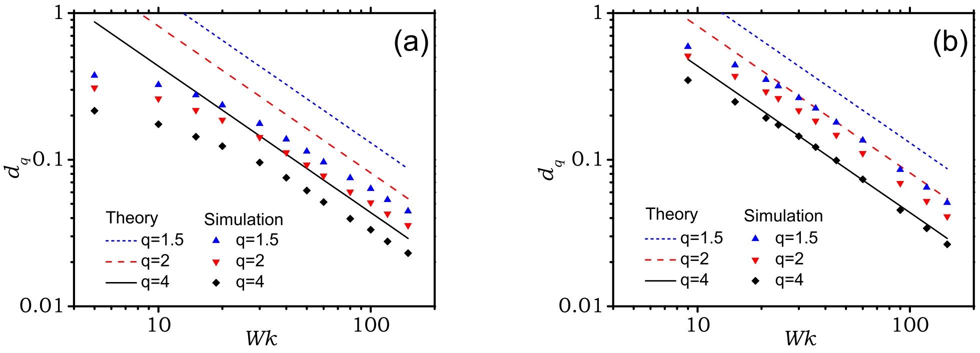

Figure 4.8: The anomalous dimensions d_q extracted from direct numerical diagonalization (symbols) for three different values of q are compared with the perturbation results (lines) of Eq. (4.17) in the weak coupling regime for different values of disorder and (a) $k = 1$ or (b) $k = 3$. The numerical results converge to the theory slowly.

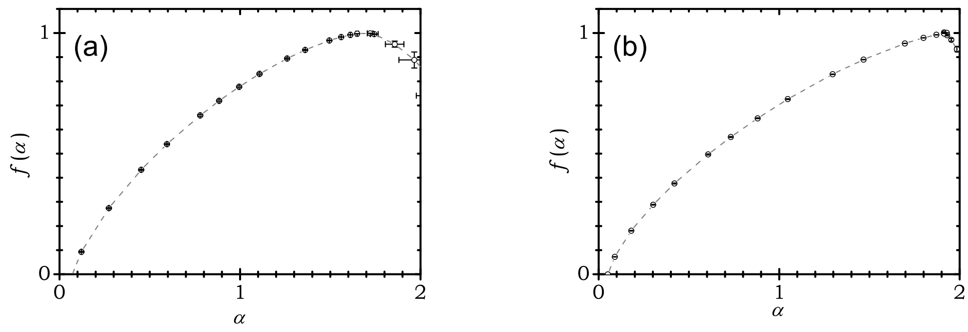

Figure 4.9: The multifractal spectrum $f(\alpha)$ for (a) TEM critical modes and (b) Hermitian matrices H0 extracted directly from the eigenvectors by using the method of Chhabra and Jensen [31]. For both graphs $W = 30$ and $k = 1$. The error bars indicate to the standard deviation among 20 realizations of disorder and are smaller than the symbol size for most of the data points. The dashed lines are guides to the eye.

4.3.5 The singularity spectrum

For a precise derivation of α and $f(\alpha)$ one has to perform a full scaling analysis on the intensity distribution. This is either possible by applying relation (3.29) to the calculated set of anomalous exponents or by a direct processing of the wavefunction intensities. The latter method, which was introduced by Chhabra and Jensen [31], is computationally superior. For this method there is no need for a Legendre transform, which is very sensitive to the numerical uncertainties.

We have applied the direct determination method to extract the singularity spectrum for TEM critical eigenfunctions and the Hermitian model H0. The results are shown in Fig. 4.9. As can be seen in both graphs, the position of the peak of the spectrum is different from the peak of the corresponding PDF plots, $\tilde{\alpha}_m$, which are presented in Figures 4.4(c) and 4.6(a). This difference is due to the large skewness of the PDF resulted from the very weak coupling regimes that are considered in this work.

For the Hermitian critical models the domain of α is restricted to $(0, 2d)$ due to the symmetry relation of $f(\alpha)$ [94]. Yet, there is no proof that this symmetry also holds for non-Hermitian matrices. From our data, it seems plausible that this symmetry is actually broken and there are some points with $\alpha > 2$. However, to provide a strong numerical evidence for this statement one has to analyze much larger ensembles with higher numerical precision.

4.4 Summary and conclusion

We have investigated, theoretically and numerically, the statistical properties of the eigenmodes of a class of complex-symmetric random matrices, which describe the electromagnetic propagation of polarization waves in a chain of resonant scatterers. We have found that all of the TM modes are localized in the weak coupling regime. The TEM modes in this regime show critical behavior due to the r^{-1} dependence in the dyadic Green function. This critical behavior is in agreement with the results of the method of virial expansion for almost diagonal matrices. We have used this method to calculate the MF spectrum of TEM modes.

Although the perturbation theory suggests criticality for all TEM modes, the numerical analysis shows this type of scaling only for part of the spectrum in the complex plain. This is understandable in the sense that the first order result of the perturbative approach gives an oversimplified picture, which is insensitive to details of the model such as a non-trivial phase dependence of the matrix elements. To reveal which aspect of the TEM coupling accounts for the existence of a critical band in the spectrum, we have analyzed three intermediate models. These models have properties between the dipole chain interaction matrix and power-law Hermitian banded random matrices. The summary of the scaling results for all these models is shown in Fig. 4.10. It seems that both non-Hermitian character of the TEM coupling and the periodic phase of the interaction between dipoles is important for the observed critical eigenmodes.

Our analysis also resulted in another unexpected finding. The eigenvectors of Hermitian banded matrices with r^{-1} coupling are no longer critically scaling if the interaction phase is set periodically. In our model H2, the randomness is only on the diagonal. Based on the PDF scaling results, we clearly see that the eigenvectors are localized. This is in contrast with the commonly believed conjecture that an interaction potential with a phase that is incommensurate with the lattice can be considered as random.

Criticality of wavefunctions has been studied theoretically and numerically for several models in the context of condensed matter physics. Recently, such wavefunctions have been observed near the Anderson transition for elastic waves [47] and electronic density of states at an interface [106]. The recent advances in optical and microwave instrumentation makes it possible to experiment in details the propagation of electromagnetic waves in artificially made structures. Our report points out to those systems in which such critical phenomena can be directly measured. These measurements provide a lot of insight for generic models of wave transport in disordered system.

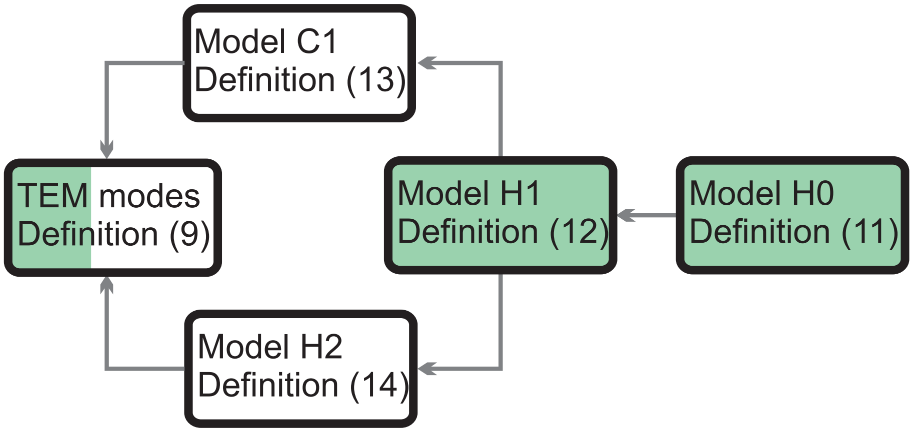

Figure 4.10: Summary of the scaling analysis on PDF of eigenvectors of matrices from various models. The intermediate hypothetic models transform the Hermitian RBM to the model describing TEM coupling. The colored boxes indicate those models that show critical scaling behavior. The model indicated by white boxes have localized eigenvectors. For TEM modes, only a part of the spectrum is critical.

CHAPTER 5

Experimental observation of multifractality near the Anderson localization transition of ultrasound

We report the experimental observation of strong multifractality in wave functions close to the Anderson localization transition in open three-dimensional elastic networks. Our results confirm the recently predicted symmetry of the multifractal exponents. We have discovered that the result of multifractal analysis of real data depends on the excitation scheme used in the experiment [47].

Critical phenomena are of prominent importance in condensed-matter physics. Criticality at the Anderson localization transition has been the subject of intensive theoretical research in the past three decades. Some important theoretical predictions have been made, among which is the remarkable aspect of multifractality of wave functions at this transition. Numerical simulations support these predictions but also raise more questions [43]. Recent experimental progress has paved the way for the direct investigation of the Anderson localization transition at the mobility edge in real samples [30, 64, 97].

In this chapter, we present the first experimental observation of strong multifractality (MF) just below the Anderson transition. This observation is based on the excitation of elastic waves in an open 3-d disordered medium. The symmetry relation (3.30) of the MF exponents [94], which was introduced in section 3.4.4 is tested and confirmed. All results are compared with the corresponding analysis of diffusive (metallic) wave functions in the same network at a different frequency or with a light speckle pattern generated by a strongly scattering medium, showing a very clear difference between localizing and diffusive regimes. Our results not only highlight the presence of MF in wave functions close to the mobility edge, but also reveal new aspects of the MF character in real experimental systems.

Most of the available information about MF is based on numerical investigations (See Ref. [43, 60, 91] and references therein). The early experimental attempts to observe strong MF in wave functions were performed by Morgenstern et al. using scanning tunneling microscopy of 2-d electron systems [97]. Their observation of MF was hindered by the presence of several eigenfunctions in the measurement and by the limited size of their system. Shortly after our report was published, Richardella *et. al* succeeded in recording critical spatial correlations in electronic states in $\mathrm{Ga_{1-x}Mn_xAs}$ samples close to the metal-insulator transition [106].

5.1 The experiment

We have used ultrasonic measurements to demonstrate three different, but closely related, manifestations of MF: (1) the non-Guassian form of the probability density function (PDF), (2) the scaling of generalized Inverse Participation Ratios (IPR), and (3) direct extraction of the singularity spectrum. Our experiments were performed on disordered single-component elastic networks, made by brazing randomly-packed aluminium beads together [64]. The diameter of each bead is 4.11 mm. The data presented here were obtained from a representative disc-shaped sample with a 120 mm diameter and 14.5 mm thickness. Two different configurations were used for excitation. In the first excitation scheme a point-like ultrasound source emits short pulses next to the sample surface. In the second case the source was put far from the sample so that a quasi-planar wave was incident on the whole interface. In close proximity to the opposite interface, vibrational excitations of the network were probed with sub-wavelength-diameter detectors in the frequency range of 0.2 to 3 MHz, where the wavelengths are comparable to the bead size and the scattering mean free paths are much less than the sample thickness [64]. The intensity at a particular frequency was determined from the square of the magnitude of the Fourier transform of the entire time-dependent transmitted field in each near-field speckle. The intensity was normalized by the total intensity in the measured speckle pattern. The normalized speckle intensity, $I(j)$ was recorded at each point j on a square grid of linear size $L_g = 55$ points with a typical nearest-neighbor spacing of 0.66 mm.

In the lower frequency band around 250 kHz, the ultrasound propagation is diffusive. A localizing regime is observed in a 50% bandwidth around 2.4 MHz, where the measured localization length in the sample is smaller than the size of the analyzed speckle patterns $(0.7L_g)$ and almost equal to the sample thickness. A full description of the experiment and a thorough comparison of previous measurements with the self-consistent theory of localization has been presented in [64].

5.2 Scaling analysis

We obtain the PDF from the histogram of the logarithm of box-integrated intensities I_{B_i}. We sample over 100 speckles in a 5% bandwidth around 250 kHz and 2.4 MHz for diffusive and localized regimes, respectively. Two representative histograms are shown in Fig. 5.1 with typical box sizes of $b = 9$ and $b = 2$ points for low and high frequency measurements, corresponding to box sizes of approximately two wavelengths in both cases. The PDF for localized waves is clearly much wider than the one for diffusive waves and the peak is shifted from the average intensity. We have also plotted the peak-position and the width of the histogram as a function of box size in the inset of Fig. 5.1.

In principle, it is possible to extract the MF spectrum from the PDF [107]. However, a box-counting analysis can give more accurate results based on the scaling of the IPR. Similar to many numerical studies, we approximate the expectation values by box-sampling over a single or multiple wave functions measured for a single realization of disorder. This

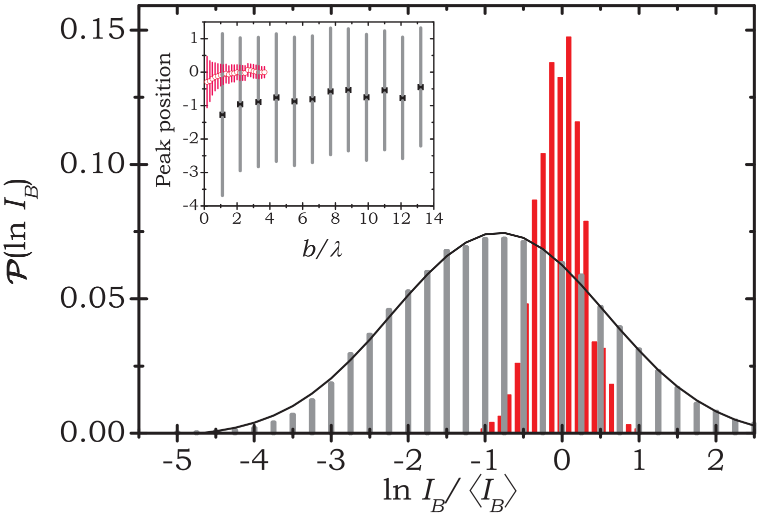

Figure 5.1: Comparison between coarse-grained PDF for localized and diffusive speckle intensities. The PDFs are experimentally obtained from the histogram of the logarithm of averaged intensities in the localized (thick bars) and diffusive (thin bars) regimes. The black line shows a fit to a single parameter log-normal distribution given by the parabolic approximation of Eq. (3.28). Inset: The peak position (symbols) and the full width at half maximum (bars) of the intensity histogram is plotted for localized (circles) and diffusive (squares) speckles as a function of coarse-graining box size.

approximation is known as typical averaging. Typical averaging is unable to reveal information that is related to statistically rare events [43]. In this approach, the system size is fixed and supposed to be large enough relative to the box size. The approximate scaling relation is derived by plotting the estimated IPR, given by Eq. (3.26), versus the box size b [1]. Note that although we have examined three-dimensional samples, the Euclidian dimension of our sampling space is two since the available data is taken just from the surface of the sample. The effective system size is L_g over which the intensities are normalized. By plotting P_q versus the box size in bilogarithmic scales [e.g., see the inset to Fig. 5.2(a)], power-law behavior is found for $q \in [-3, 4]$, with the slope yielding the scaling exponent $\tau(q)$. The average anomalous exponent is obtained by averaging the exponents measured for several frequencies between 2.0 and 2.6 MHz and subtracting off the normal part of the exponent $2(q-1)$. The standard deviation is taken as the error-bar.

The anomalous exponents are plotted as a function of q in Fig. 5.2(a). For comparison with the localized data, the same numerical procedure was applied to a diffusive speckle pattern, where the behavior is entirely different ($\Delta_q = 0$). In making this comparison, an optical diffusive speckle pattern was used to capitalize on the best available statistics.

The behavior of the anomalous exponents shown in Fig. 5.2 provides unambiguous evidence for surface MF of the localized ultrasound wave functions. This is the most important observation in this chapter. Note that MF is clearly seen in these data, even though the localized wave functions in our finite sample are near to, but not exactly at, criticality. In addition, our observation of MF clearly supports the predicted symmetry relation (3.30). Our experimental demonstration of this fundamental symmetry, seen in a very different system to the ones envisaged in [94], attests to the universality of critical

---

[1] We have used box sizes $b \in \{2, 3, 4, 6, 8, 12, 24\}$

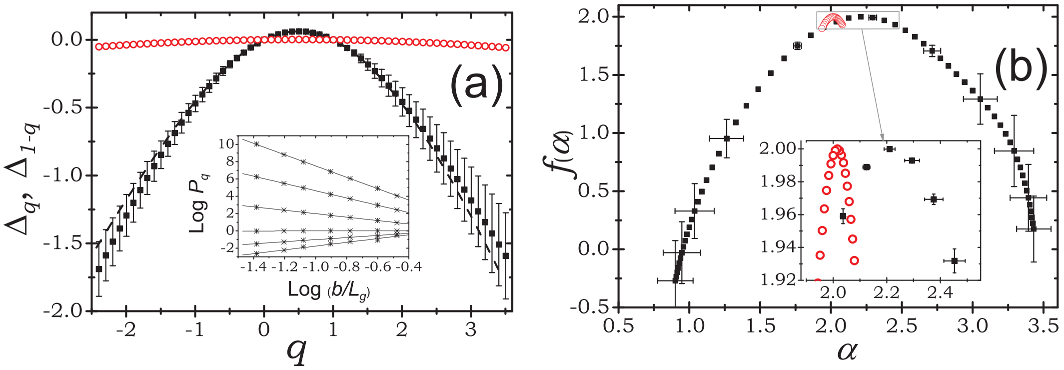

Figure 5.2: (a) The measured anomalous exponents Δ_q are shown for localized ultrasound (full squares) and diffusive light (open circles) speckles. The dashed line shows the same data-points, mirrored relative to $q = \frac{1}{2}$ in order to check the symmetry in the spectrum. The anomalous exponents are estimated from the box-counting method. The slope of the IPR plotted versus the box size in bilogarithmic scales yields Δ_q. One example is shown in the inset for $q \in \{-2, -1, 0, 1, 2, 3\}$ and $f = 2.40$ MHz. (b) The average singularity spectrum is calculated for the ultrasound speckles (full squares) at frequencies between 2.0 to 2.6 MHz. For comparison a singularity spectrum for diffusive optical speckle (open circles), with the Euclidian dimension, is extracted by applying the same box-counting procedure.

properties near the Anderson transition.

Finally, we have extracted the surface MF spectrum directly from the measurements using a direct method [31]. In this method, the numerical error caused by the Legendre transform (3.29) is avoided. To get enough statistics, 100 wave functions in a bandwidth of 5% are used to estimate the MF spectrum for several seven frequency bands between 2.0 and 2.6 MHz. No systematic deviation is observed between the seven spectra obtained in this frequency range. These spectra are then averaged for each value of $q \in [-6, 6]$ and the standard deviation is considered as the error bar. The results are summarized in Fig. 5.2(b). The peak of the MF spectrum is shifted from two (the Euclidian dimension of the measurement basis) by a value of 0.21 ± 0.02. For comparison, the same procedure is applied to the optical speckle using the same q-range. No shift is observed for the optical speckle.

The MF that is clearly seen in our data allows us to test the deviation from the parabolic approximation. This is characterized by the reduced anomalous exponents $\delta_q \equiv \frac{\Delta_q}{q(1-q)}$. In our results, shown in Fig. 5.3(a), we see a deviation of less than 20% for $q \in [-3, 4]$. The non-parabolicity of the spectrum is very difficult to measure but it may have important theoretical consequences. More precise investigation of larger samples is needed to reliably confirm or exclude the possibility of a small but significant deviation.

5.3 Discussion

We have also investigated the dependence of the reduced anomalous exponent at the symmetry axis, $\delta_{\frac{1}{2}} = 4\Delta_{\frac{1}{2}}$, on the frequency and type of excitation. The results are presented in Fig. 5.3(b). We observe a robust presence of MF for all frequencies between 1.7 to 2.9 MHz. The measured anomalous exponent is larger for the point source illumination. This difference may be related to the number of modes excited in each scheme. It has been

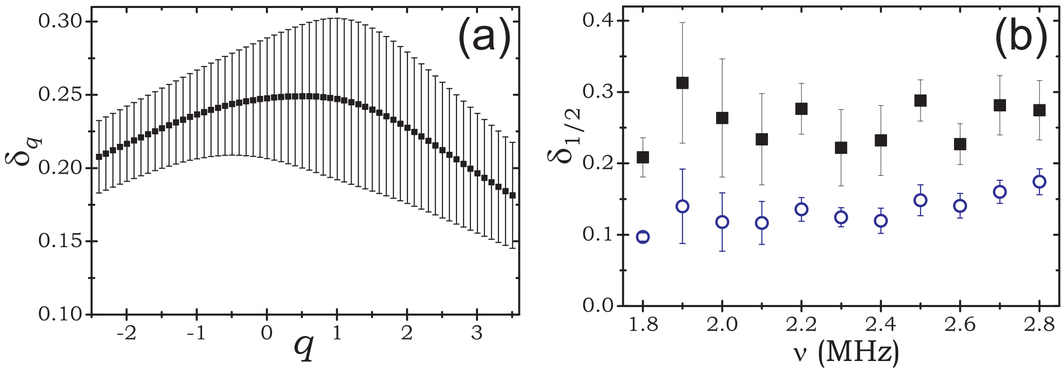

Figure 5.3: (a) The reduced anomalous dimension $\delta_q \equiv \frac{\Delta_q}{q(1-q)}$ is plotted versus q. Bars show the estimated error. Deviation from a horizontal line corresponds to the deviation from parabolic approximation. (b) The reduced anomalous dimension $\delta_{\frac{1}{2}}$ is plotted versus frequency in the localized regime for two excitation schemes: point-source (squares) and plane wave (circles). The error bars represent the standard deviation of the measured exponents that are averaged over each 0.1-MHz-wide frequency band.

previously discussed [127] that the overlap of two or more eigenmodes shifts the peak of the singularity spectrum towards the Euclidian dimension. Since the surface area of the sample is larger than the localization length, neighboring localized modes may coexist at the same frequency. These modes can all be excited by a quasi-plane wave while a point source couples more efficiently to the closest mode.

5.3.1 Deviation from numerical results

Numerical analysis of bulk and surface MF for the eigenstates of the Anderson tight-binding Hamiltonian on a 3-d cubic lattice at the metal-insulator transition have predicted corresponding shifts of 1.0 and 1.6 from the Euclidean dimension for the peak of the singularity spectrum [95, 107]. Another numerical study for an equivalent vibrational model on the *fcc* lattice shows a similar outcome for bulk MF [81], indicating to the universality of this phenomenon. It is not simple to explain the difference between the available numerical results and our experimental outcome. Several issues may play a role. Mode overlap and the finite lifetime of modes due to open boundaries are two of these issues. Most numerical studies are done based on uncorrelated disorder, which is experimentally hardly ever achieved. The uniform bead size in our samples, which is comparable with the vibrational wavelength, is a source of correlation. The presence of correlation in the disordered potential may influence the critical behavior and induce nonuniversality [35].

5.3.2 Final remarks

Despite the wealth of theoretical and numerical studies on the Anderson transition in 2-d and 3-d for the Schrödinger Hamiltonian in closed systems, critical properties of this transition for classical waves in an open system have never been studied. Our system is especially challenging due to its 3-d nature, open boundaries and presence of three polarizations for the elastic waves. Specific properties of classical waves such as absorption are yet to be investigated in the context of criticality. Our results show that these important questions can now be investigated experimentally, providing vital guidance for new theoretical work.

Our experiments reveal that the concept of MF not only concerns critical states but is valid as well around the mobility edge. This observation agrees with recent theoretical investigations [32]. Mutual avoidance of wavefunctions at large energy separations and their enhanced overlap at small energy separations are other important predictions of that theory, which can also be verified by our experiment.

In conclusion, we have presented the first experimental observation of multifractal wavefunctions below the localization transition. Our data validate experimentally the predicted symmetry relation of the anomalous exponents. Free from interactions and with the possibility of diverse illumination and detection schemes, sound and light experiments can provide a tremendous amount of useful information for this field of research. We believe that our observation of multifractality in classical waves will stimulate new theoretical and numerical investigations. On the experimental side, this work highlights again the strength of statistical methods for studying Anderson localization.

CHAPTER 6

Refractive index tuning

In this chapter, we introduce a new approach for measuring both the transport and the effective medium properties of light propagation in inhomogeneous media. These properties include the diffusion constant, the path length distribution, and the derivative of the effective index of refraction with respect to the changes in the density of the host medium. This method utilizes the equivalence of frequency variation to a change in the index of refraction, which was derived in chapter 2. Experimentally, we measure the correlations in the speckle via spectrally resolved refractive index tuning (RIT), controlling the latter via changes in the ambient pressure. This new generic measurement technique can be used to characterize a wide variety of materials, including photonic crystals, random photonic media, photonic meta-materials, and certain porous biological samples like bone and wood. In this chapter, we report some proof-of-principle measurements on well-characterized samples to show the precision of the RIT method [44].

Optical properties of quenched random samples are dominated by speckle, a highly irregular intensity pattern dependent upon spatial (or angular) or time (or frequency) coordinates caused by interference. Correlations, which are inherent properties of speckle despite the apparent irregularity, provide important information about transport parameters. In fact, the description of intensity correlations is at the heart of understanding transport theory [49]. In the past, correlations have been measured in time [24] and frequency [55] as a means of, for example, determining the diffusion constant of light.

What is often overlooked is the degree to which effective medium properties are essential for determining correlation functions, and thereby transport properties. Indeed, the importance of the effective medium, in some sense, exceeds that of the transport properties as the latter only becomes important when the material is turbid. Furthermore, as we have seen in developing a theory of transport in chapter 2, the effective medium is used as a building block. That is to say, the diffusion constant of light depends on the average index of refraction but not the other way around.

In this chapter, we make use of the symmetry between changes in refractive index and frequency variation that was explained in section 2.2. This symmetry allows us to perform "dynamic" measurements without using sophisticated time-resolved experiments or a pulsed light source, which is often much more costly than a monochromatic CW laser. By tuning the effective index and measuring intensity-intensity correlations, we show that a variety of transport properties of the sample can be measured in an entirely new way. Furthermore, by combining measurements of refractive index correlations with frequency correlations, the applicability of effective medium assumption is directly tested. This type of effective medium measurement is unprecedented, in that it is not affected by surface irregularities, does not require a coherently transmitted beam, and can be measured for any irregular sample shape. This new technique allows for transport properties to be determined without resorting to gross approximations for the effective medium. Given the importance of understanding disorder in a wide variety of fields including biology [57], advanced materials [120], solar cells [100], and in general modern photonics, we expect from our approach to find broad and cross-disciplinary applications.

Our method is based on controlled change of the optical path length distribution by refractive index tuning (RIT). It is the optical analogue of a class of experiments in condensed matter physics that control the elongation of electron trajectories by using a magnetic field. Those electronic experiments resulted in the observation of electronic weak localization and universal conductance fluctuations [18]. Due to its simplicity and high precision, RIT measurements can be applied to a diverse set of rigid samples, which cannot be analyzed by other dynamic methods due to the limitation of time (or frequency) resolution. The concept of changing the optical path length distribution has also been exploited for diffusing wave spectroscopy [85, 104], and for other types of waves in evolving media [77, 80, 121].

6.1 Theoretical principles

We assume a multiple scattering medium with quenched disorder. Previously, we have seen that in the diffusion approximation, the amplitude Green function, the amplitude correlator, and the intensity propagator only depend on the product $n_e\omega$. That is to say changing the frequency by $\Delta\omega$ is equivalent to changing n_e by Δn_e if $n_e\Delta\omega = \omega\Delta n_e$. This symmetry relation sets the basis for all the experiments in this chapter. It holds in a regime where

$$\frac{\Delta \mathrm{Im} K}{\Delta \mathrm{Re} K} \sim \frac{1}{4\pi}\left(\frac{\lambda_e}{\ell_s}\right)^2 \left|\frac{\Delta \ell_s}{\Delta \lambda_e}\right| \ll 1, \tag{6.1}$$

where K is the effective wavenumber for the average amplitude Green function, introduced in section 2.1.3.

By using this symmetry, we can generalize the results for the frequency correlation function, $\Delta n_e = 0$, to our case of variable refractive index. In this chapter, we will use this correlation for the slab geometry [55].

To take one example, relevant to our measurements, consider a slab of porous material, for which the host refractive index, n_h, may be tuned. The correlation is then measured as a function of n_h instead of n_e. In this case, $C^{(1)}_{\omega,\omega}(n_h, n_h + \Delta n_h)$ is given by:

$$C^{(1)}_{\omega,\omega}(n_h, n_h + \Delta n_h) = \frac{\tau_\delta \Delta n_h}{\cosh\sqrt{\tau_\delta \Delta n_h} - \cos\sqrt{\tau_\delta \Delta n_h}}, \tag{6.2}$$

with RIT decay coefficient (generalized analogue of diffuse decay time)

$$\tau_\delta \equiv \frac{2\omega\delta L^2}{D}. \tag{6.3}$$

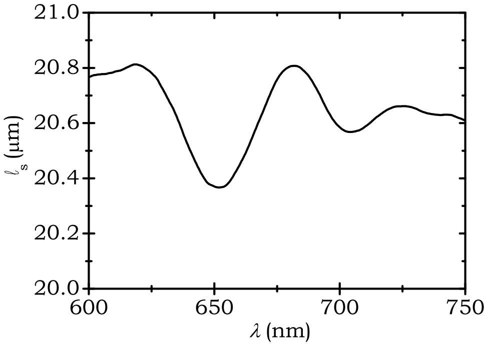

Figure 6.1: The mean free path as a function of light frequency measured for a 1-mm thick layer of porous polystyrene filter using a total transmission setup. The reported values are measured with an accuracy of $\pm 0.2\,\mu$m.

Here, we have introduced the tuning response δ, as

$$\delta \equiv \frac{1}{n_e}\frac{\partial n_e}{\partial n_h}. \tag{6.4}$$

The tuning response relates the change of n_e, a more or less theoretical concept, to the changes in n_h which can be easily experimentally controlled. We have accurately measured δ as will be shown later in this section. Knowing the accurate value of δ enables us to extract the diffusion constant by measuring the RIT correlation function $C^{(1)}_{\omega,\omega}(n_h, n_h + \Delta n_h)$. The tuning response δ is an important effective medium parameter, since it can be measured even for opaque samples with large optical thicknesses and unconventional geometries. Such samples pose a formidable and often insurmountable challenge for the more conventional measurements of effective refractive index.

6.2 Samples

For proving the principles of RIT technique, we have chosen samples that can be characterized by both RIT and conventional time-resolved measurements, allowing us to validate the accuracy of this technique. We consider a composite porous system with open channels consisting of a solid backbone and a gaseous host. The refractive indices of the solid backbone and the gaseous host medium are n_s and n_h respectively. In our measurements the index of the host, n_h, is tuned by increasing the pressure of the gas.

Porous polystyrene filters

The first measurements are performed on slabs of commercially available porous plastic air-filters (XS-7744, Porex Corp.) with various thicknesses. They are composed of sintered polyethelene spheres with a broad size distribution of 7 to 12 μm. The refractive index of the polyethelene is $n_s = 1.49$. This material has a porosity of $\phi = 0.46 \pm 0.02$ and a mean free path of $\ell_s = 20.6 \pm 0.2$ μm in the frequency range of interest. The porosity was determined by weighing a larger sample of the same material. The mean free path was determined from total transmission measurements. The result for the transport mean free

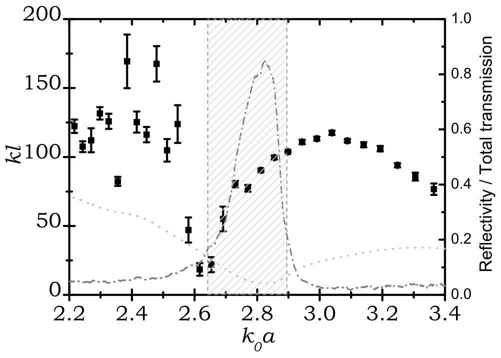

Figure 6.2: Optical characterization of opal photonic crystals. The dots show the scattering parameter $k\ell$ as a function of frequency. The dashed line is the specular reflection at normal incidence and the dotted line is the total transmission of light impinging at normal incidence, which is measures by using an integrating sphere. The gray shaded area indicates to the stop band.

path is shown in Fig. 6.1. These measurement reveal a negligible (max 2%) variation of ℓ_s in the frequency span, justifying the assumption in Eq. (6.1).

Self-assembled photonic crystals

We have also performed RIT measurements on a set of photonic crystal samples. These crystals are made of polystyrene colloidal spheres of 300 nm diameter (Duke Scientific) using the method of vertical controlled drying [61]. The grown crystal shows a stop-band in transmission of the visible frequencies, which puts restriction on the use of effective medium description for the average index of refraction. By using these measurements we can quantify the validity of an effective medium model experimentally determine the tuning response dispersion for such a resonant photonic environment.

The optical behavior of these crystals is characterized by reflection and transmission measurements. A thickness of 10 μm was measured using an optical microscope. The scattering strength is measured for this sample by using a white-light enhanced backscattering setup [99]. The summary of these results is shown in Fig. 6.2. The stop-band is clearly visible in the reflection measurements. This stop-band occurs around the incident wavelength of 667 nm. Interpretation of the fluctuation in scattering parameter at the band edges is a very interesting topic on its own but it is beyond the scope of this chapter. The refractive index of bulk polystyrene is $n_s = 1.59 \pm 0.02$ in visible and near infrared frequencies.

6.3 Setup and measurements

The sample was kept in a pressurized chamber and illuminate by a HeNe laser at 632.8 nm. Part of the transmitted speckle pattern was filtered by a linear polarizer and recorded on a 16-bit CCD-camera with 10^6 pixels. This setup is schematically drawn in Fig. 6.3(a) The recorded image consisted of roughly 10^4 independent coherence areas. Gradually tuning the air pressure in the chamber changes n_h, causing the speckle pattern to evolve. By monitoring the sequence of images, we can directly measure the autocorrelation coefficient of the evolving intensity pattern.

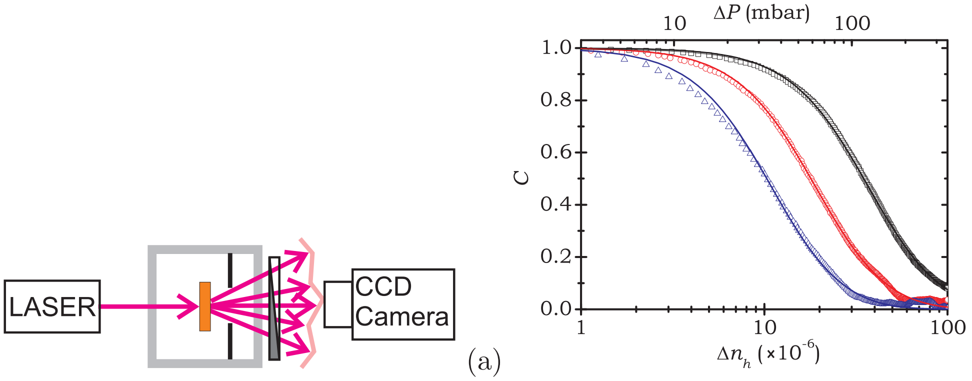

(a) (b)

Figure 6.3: (a) The experimental setup. The sample is placed in pressurized chamber and illuminated by a HeNe laser. A single polarization of the transmitted speckle is recorded by a CCD-camera. (b) RIT autocorrelation coefficient as a function of Δn_h. Data points show measurement results for 3 slabs of polyethylene filters ($L = 1, 1.5$, and 2 mm for black squares, red circles, and blue triangles, consequently). The lines show the fit to theory (Eq. (6.2)).

The first experiment was performed on three samples. The extracted correlation coefficients are plotted in Fig. 6.3(b) versus Δn_h. Each data series is fitted to the correlation function of Eq. (6.2) with a separate single fitting parameter, τ_δ. We see an excellent agreement between the theory and the experimental results. The optical path length distribution can be extracted from these measurements by applying a Fourier transform [56]. Remarkably, the sensitivity to the change of refractive index, demonstrated in Fig. 6.3(b), is close to some of the state-of-art refractive index sensors [144].

6.4 Results and discussion

6.4.1 Diffusion constant of porous plastic

Having measured the RIT decay coefficient τ_δ it is possible to extract the diffusion constant. This requires the value of tuning response δ. We present a precise method of measuring δ, which also makes use of the symmetry relation in the Green's function discussed earlier in this chapter. This symmetry implies that $C_{\omega,\omega+\Delta\omega}(n_e, n_e + \Delta n_e)$ has a peak equal to one for a nonzero shift $\Delta\omega$ given by

$$(n_e + \Delta n_e)(\omega + \Delta\omega) = n_e\omega \quad \text{or} \quad \frac{\Delta\omega}{\omega} = -\frac{\Delta n_e}{n_e}. \tag{6.5}$$

In other words, δ can be extracted from the spectral shift of every individual speckle spot while the host index of refraction n_h is varied.

To monitor this spectral shift the experimental setup was slightly altered. The light source was replaced by a white-light super-continuum laser (Fianium). The CCD-camera was replaced by a spectrometer, which was run in the imaging mode. The entrance slit of the spectrometer selects a transmission direction in form of a narrow rectangle, which contains roughly 10 independent coherence areas along the slit. The beam is spectrally resolved perpendicular to the slit direction by a grating. This configuration allows us to simultaneously monitor the spectral evolution of several speckle spots while n_h is changed.

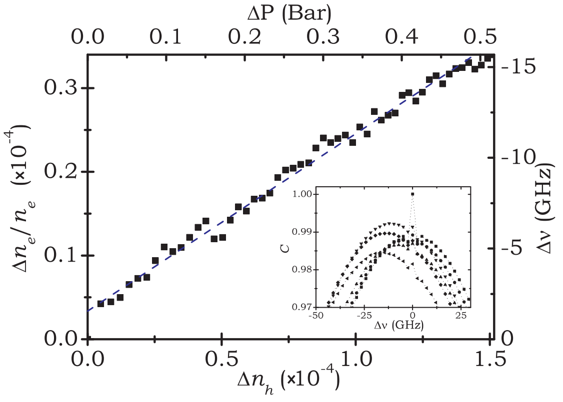

Figure 6.4: Measured relative change of n_e as a function of Δn_h. The value of $\Delta n_e/n_e$ is extracted by measuring this spectral shift. The refractive index of air is calculated based on the Edlen formula [39]. Inset: The shifted cross-correlation coefficient C versus the spectral shift $\Delta\nu$ for certain pressures (From right to left: $\Delta P = 0.0$, 0.075, 0.18, 0.28, 0.37, and 0.46 bar). The peak position of each curve denotes the spectral shift, which is proportional to the relative change in the effective refractive index. The spiky feature at zero position is an artifact of the slight inhomogeneity over the detection efficiency of CCD pixels.

The measurement was performed on a 100-μm-thick slice of the polyethelene filter. The selected thickness was optimized for the resolution of our monochromator. The intensity spectrum between 649 and 651 nm was measured while changing the pressure in the chamber from 1 to 1.5 bar in steps of 10 mbar.

RIT correlation functions at different frequencies are calculated from the measurements and plotted as a function of $\Delta\omega$ for each pressure. A collection of these plots is shown for six different pressures in the inset of Fig. 6.4 as typical representatives. As predicted, the peak value is shifted and equals unity within the experimental error. The peak position, measured by fitting a parabola to the top of each curve, denotes the overall spectral shift. Using our symmetry relation (6.5), the relative change of effective refractive index is calculated and plotted as a function of Δn_h in Fig. 6.4. We get a value of $\delta = 0.212 \pm 0.003$ from the slope of a linear fit to the data, for these set of samples, with a remarkably high precision.

In principle, it is possible to extract the diffusion constant from each separate RIT measurement. To improve the accuracy, we plot the auxiliary parameter $a \equiv 4\pi\nu\delta/\tau_\delta$ versus L^{-2} from the three measurements presented in Fig. 6.3. This plot is shown in Fig. 6.6. The slope gives the diffusion constant $D = 2.2 \pm 0.1$ m^2/ms using Eq. (6.3).

6.4.2 Comparison with the time-resolved method

To prove the quantitative exactness of our method, we compare our result for the diffusion constant with the result of conventional time-resolved measurements. The diffuse transmission through the same samples was recorded using a time-correlated photon counting setup and a subpicosecond pulsed laser at 600 nm wavelength. The resulting temporal decay curves are presented in Fig. 6.5. Following the guidelines of Ref. [67] and considering the response function of the detector, the diffuse decay time $\tau_d \equiv L^2/\pi^2 D$ is extracted from a fit to these measurements. The diffusion constant is calculated from the slope of a linear fit of the parameter $b \equiv \frac{1}{\pi^2\tau_d}$. vs. L^{-2}, shown in Fig. 6.6, resulting in $D = 2.1 \pm 0.1$ m^2/ms, This result is in excellent agreement with the value obtained from the index tuning experi-

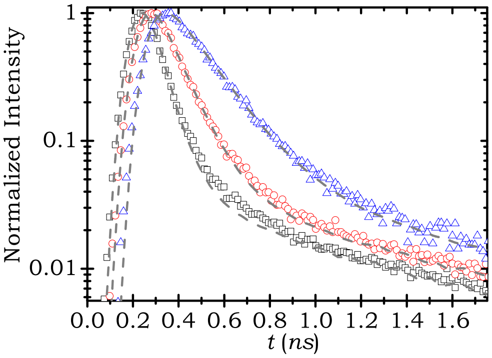

Figure 6.5: Time resolved intensity decay curve for slabs of polyethylene filters. Different datasets correspond to different sample thicknesses ($L = 1, 1.5$, and 2 mm for black squares, red circles, and blue triangles, respectively). The lines show the fit to the diffusion model after considering the absorption and the response of the detector.

ment. The high precision of this agreement is an important confirmation of the concept of effective wavenumber in random media. This concept has never been examined so directly in strongly scattering media, simply because it was a very difficult parameter to access experimentally.

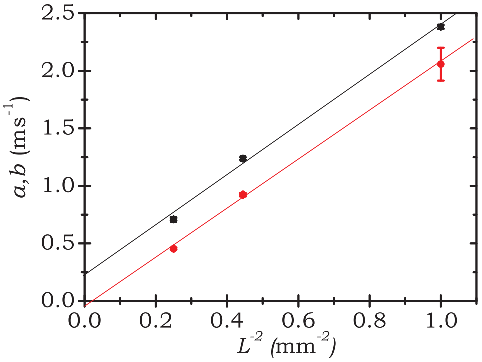

Figure 6.6: The measurement parameters $a \equiv \frac{4\pi\nu\delta}{\tau_\delta}$ and $b \equiv \frac{1}{\pi^2\tau_d}$ are plotted versus the inverse of the thickness squared. Black squares and red dots correspond to the index tuning and time-resolved measurements respectively. The slope of each data set is equal to the diffusion constant D measured by each specific method. The fact that the two slopes are equal proves the consistency of our index tuning method with the time resolved measurements.

6.4.3 Tuning response of a photonic crystal

RIT enables us to monitor the behavior of tuning response as a function of frequency. This measurement is especially interesting if there medium has a resonance behavior like a photonic crystal. For this measurement we divide the frequency spectrum to narrow bands of 5 nm wide. For a finer frequency resolution, thicker samples must be used.

By recording the spectrum of a narrow transmission angle and monitoring its shift while changing the pressure inside the chamber, we can measure the tuning response. Measuring

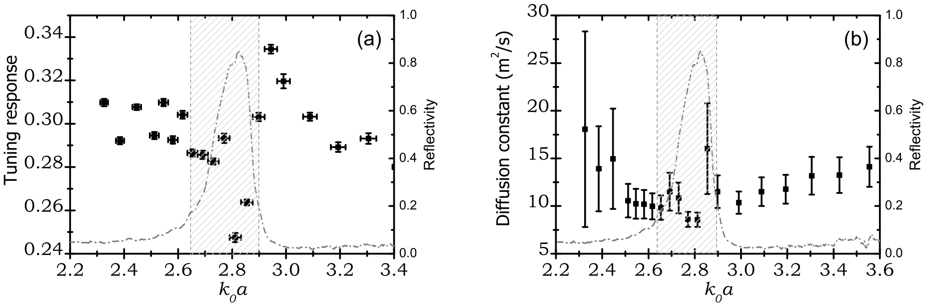

Figure 6.7: (a) The tuning response of the opal photonic crystal as a function of wavelength. The dashed line is the specular reflection at normal incidence and shows the position of the stop band. (b) The (average) diffusion constant as calculated from the frequency correlation in the spectrum of a narrow transmission channel.

the frequency correlation at a single pressure will provide the diffusion constant. The tuning response and diffusion constant of the opal sample, described earlier in the chapter, were measured across its stop band. The results are shown in Fig. 6.7. There is more about 30% variation in the tuning response when crossing the stop-band. This result clearly shows that all effective medium theories that does not consider the dispersion in a photonic crystal fail in describing its effective refractive index. The RIT method for measuring δ is applicable to a variety of samples, and assumes no specific effective medium model. Such a property can be a perfect check for the accuracy of numerical simulations when applied to complex photonic structures such as metamaterials or photonic crystals. The parameter δ can also be predicted using theories of the effective medium [22, 23, 117] which are all based on long-wavelength limits. This comparison is further discussed in the following section.

6.5 A test for effective-medium theories

In this section results from different effective medium theories are reviewed. The tuning parameter δ is calculated for for the same sample that was investigated earlier in this chapter using three of the models. The predictions are compared the result of the RIT measurement. Before showing this comparison, we briefly mention the idea behind these models.

Geometric ray picture

In this model the refractive indices are linearly averaged, weighted by the volume filling fraction of each component. This method is used in most of the hand-waving estimated [61]. In specific, it was used by Zhang and Sheng [117] for describing scalar-wave localization.

$$n_e = \phi n_s + (1-\phi) n_h, \tag{6.6}$$

$$\delta = 1 - \phi. \tag{6.7}$$

Scalar long-wavelength limit

This model is similar to the geometric picture except for averaging permittivities in place of refractive indices. It was used by Vos *et* al. for describing photonic crystals and derived by Busch and Soukoulis from coherent potential approximation. To derive refractive index derivatives from dielectric constant derivatives one should note:

$$n_e = \sqrt{\epsilon_e}, \quad n_h = \sqrt{\epsilon_h}, \quad n_s = \sqrt{\epsilon_s}, \tag{6.8}$$

$$\delta \equiv \frac{\partial n_e}{\partial n_h} = \frac{n_h}{n_e}\frac{\partial \epsilon_e}{\partial \epsilon_h}. \tag{6.9}$$

This model averages the dielectric constants according to the volume fraction.

$$\epsilon_e = \phi\epsilon_s + (1-\phi)\epsilon_h, \tag{6.10}$$

$$\delta = \frac{n_h}{n_e}(1-\phi). \tag{6.11}$$

Maxwell-Garnett dielectric function

The Maxwell-Garnett formula is perhaps the most widely used estimate for the effective refractive index in colloidal suspensions. It is given by

$$\epsilon_e = \epsilon_h \left[1 + \frac{\phi\beta(\epsilon_s - \epsilon_h)}{1 - \phi + \phi\beta}\right], \tag{6.12}$$

Where β is a function of the shape and orientation distribution of the scatterers. This theory assumes low volume fraction of the solid part. Therefore, we calculate δ only up to the first order in ϕ.

$$\delta = \frac{n_h}{n_e}\left(1 + \left[(n_s^2 - 2n_h^2)\beta + \frac{n_h}{2}(n_s^2 - n_h^2)\frac{\partial\beta}{\partial n_h}\right]\phi\right). \tag{6.13}$$

Bruggeman dielectric function

This model was suggested by Bruggeman to correct for the asymmetry of the Maxwell-Garnett formula with respect interchanging the host medium and the inclusion. However, it is still a phenomenological model, and is not fully justified apart from the Rayleigh scattering regime. It suggests

$$\phi\frac{\epsilon_s - \epsilon_e}{\epsilon_s + 2\epsilon_e} + (1-\phi)\frac{\epsilon_h - \epsilon_e}{\epsilon_h + 2\epsilon_e} = 0. \tag{6.14}$$

The explicit formulae for the tuning response in this model is rather lengthy, but it can be easily estimated for a specific choice of refractive indices and filling fractions. An extensive discussion on the applicability of conventional models can be found in the book by Bohren and Huffman [22].

For illustrative purposes, we present the predicted value for n_e and δ by three of the more popular effective medium theories: (i) the average permittivity, (ii) the Maxwell-Garnett and (iii) the Bruggeman models. The predictions for our porous plastic samples are $n_e = 1.29 \pm 0.02$, 1.25 ± 0.02, and 1.22 ± 0.02 and $\delta = 0.28 \pm 0.02$, 0.45 ± 0.03, and 0.52 ± 0.03 respectively. These predictions for δ differ from each other and from our experimental result by as much as a factor of two. It is also worth noting that the predicted value of δ is more model-dependent than n_e itself. The main reason for this discrepancy is perhaps the assumption of the long wavelength limit, which does not hold in our experimental conditions. Our unambiguous measurement of δ highlights the necessity of more sophisticated models of the effective medium [23]. For such models, which are usually based on numerical simulations, the tuning response parameter serves as a very sensitive test.

6.6 Further applications

Apart from the fundamental insight, the concept of RIT is also useful for gas sensing or other daily life applications. Correlation function (6.2) decays exponentially with Δn_h and can also serve as a very sensitive probe of the refractive index changes in the ambient medium.

Refractive index sensor

For the 2-mm sample, a change of 10^{-6} in the refractive index of air results in 3% reduction in the autocorrelation coefficient, which is easily detectable. Most of refractive index sensing methods are based on resonances and their shifts (see [144] for a recent review). The sensitivity demonstrated in this paper is already close to the state-of-art surface-plasmon-resonance sensors while the instrumentation for our method is much simpler. However, the present work is by no means showing a limit for the sensitivity of our method, since it can be easily enhanced using thicker slabs (the sensitivity increases quadratically with the sample thickness). For higher sensitivities, technical details such as the stability of the light source and thermal isolation of the sample must be considered. These details were not optimized for the current proof-of-principle experiments. Another downside of our method is the rather large detection volume needed for a reasonable sensitivity. This disadvantage can be overcome by using larger index contrasts and shorter wavelengths, which is readily available in plasmonic sensors.

Evolution detection in turbid media

Measuring correlations of multiple-scattered waves in evolving media has shown a wide range of application in different branches such as rheology, geophysics and medicine [77, 80, 85, 104, 121]. Adding RIT to the arsenal of optical characterization techniques for turbid media, broadens the choice of samples that can be investigated. As a low-cost and portable measurement, RIT can perhaps reduce the cost of analysis in comparison with the existing spectroscopic methods in diffuse media.

6.7 Conclusions

In conclusion, we have presented a new effective medium quantity and a new transport correlation function and shown how to precisely measure both of them by using refractive index tuning. Our measurements directly test and approve the validity of assuming an effective wavenumber for an inhomogeneous medium, which is very important for describing all sorts of photonic metamaterials. Using these two quantities one can measure several dynamic transport properties with high precision, as we have demonstrated for the lowest order $C^{(1)}$-correlations and the diffusion constant. Measuring higher order correlations and studying Anderson localization is a natural follow-up to our research.

CHAPTER 7

Measuring intensity correlations using diffuse second-order interference

Methods based on nonlinear optical processes have shown to be very sensitive indicators of the microscopic structure of materials, specially at the interfaces [114]. Despite the challenges of detecting low signals, these nonlinear measurements provide valuable information about about interfaces or molecular structures that are completely inaccessible with linear microscopy [50]. The applications of measuring higher harmonics are not limited to optics and can for example be influential in studying the interior of earth by using seismic waves. Second harmonic ultrasound measurements have also been used to get a higher contrast in blood perfusion measurements inside human body.

In section 2.3, we derived the relation between the efficiency of a nonlinear conversion process with the intensity-intensity correlations inside random media. This proportionality can be potentially used to extract new information about the internal structure of opaque medium. Furthermore, some important phenomena are specific to intensity measurements and cannot be detected in amplitude-level measurements. Anderson localization is one example. The multifractal behavior of eigenfunctions that was introduced and discussed in the past three chapters can only be characterized based on the intensity distribution and its correlations [32]. The relation between fluctuation of second harmonic efficiency and the mode structure in a disordered system have also been theoretically investigated for planar composites [122].

From the theoretical results of chapter 2, we saw that the intensity-intensity correlations add an additional contribution to the total second-harmonic generation. Determination of this surplus will require an absolute measurements, which is often a challenge in realistic situations due to the unknown instrumental response functions. In this respect, a relative measurement is much easier to perform. In this chapter, we introduce such a relative measurement, and present experimental results on turbid nonlinear samples, like porous gallium phosphide and laser-crystal powder. Our results show clearly that intensity correlations of type C_0 are non-universal and their dependence on the microscopic structure is much more pronounced that typical mesoscopic parameters like scattering mean free path. These experiments also show that a scalar wave treatment is not suitable for describing the nonlinear efficiency and underscores the prominent role of light polarization and the tensorial form of the nonlinear susceptibility.

7.1 Two classes of nonlinear random media

Before describing our experimental method, we briefly review the two common types of samples that are relevant for nonlinear random media. In the first category, scattering is introduced in a slab of nonlinear dielectric by a small density of point-like scatterers. This case is theoretically analyzed by Kravtsov et al. [73]. The density of the intrusions is considered to be so small that the nonlinear susceptibility is not affected, thus the microscopic nonlinear coefficient is supposed to be uniform across the sample. The background medium can however be optically dispersive, $\Delta n \equiv n_{2\omega} - n_{1\omega} \neq 0$. This is often the case in nonlinear crystal. It is also the main limitation factor behind the extraction of the converted light due to the presence of phase mismatch and destructive interference between fundamental and second-harmonic light. The conventional way of overcoming this issue is to use birefringence crystals, but that rules out the use of several materials with high nonlinear coefficients. That is why, introducing small scatterers may enhance the second harmonic yield because it prevents the waves from destructive interference.

By applying the diffusion approximation to the nonlinear Maxwell equations, Kravtsov et al. derived the second-harmonic yield in a semi-infinite medium. Their results show that when $\Delta n \leq 0$, the bulk contribution to the diffusely-reflected second-harmonic light $R_{2\omega}$ is independent of the scattering parameter $k_{1\omega}\ell_{1\omega}$. When $\Delta n \geq 0$ then $R_{2\omega}$ depends on $k_{1\omega}\ell_{1\omega}$ like

$$R_{2\omega} \propto \cot^{-1}[A k_{1\omega}\ell_{1\omega}], \tag{7.1}$$

where A is a number that is dependent on the optical dispersion of the medium and the ratio between mean free paths at second-harmonic and fundamental frequencies. For this results to hold, the scattering mean free path must be much larger than the wavelength of light.

In the second case, a suspension of small spherical particles have been considered by Makeev and Skipetrov [83]. In their model, the conversion centers are the same as the scatterers and the background medium is linear. In their derivation the second-harmonic yield per scatterers shows no explicit dependence on the linear scattering properties of the suspension, i. e. there is no mesoscopic effect in the lowest order of density.

Unlike the first system, nonlinear conversion in the second model is local the second-harmonic intensity generated at each point is proportional to the square of the local intensity. This model holds all the assumptions we took when deriving the relation between conversion efficiency and mesoscopic C_0-correlations in chapter 2. The additional term on the order of $(k_{1\omega}\ell_{1\omega})^{-1}$ is half the product of C_0 and the zeroth-order term:

$$R^{(1)}_{2\omega} = \frac{1}{2} C_0 R^{(0)}_{2\omega}. \tag{7.2}$$

Based on this result, one should be able to measure the C_0-correlations by looking at the change in second-harmonic yield as a function of scattering strength. In practice, performing such an absolute measurement with a precision that is high enough for extracting the C_0 contribution is experimentally challenging. Furthermore, the nonlinear susceptibility of the colloidal particles may be influenced by changing their density or adding extra scatterers.

We have found a better solution and that is to use a two-beam setup. This experiment is introduced in the following section.

A second solution is to focus on a single nonlinear conversion center embedded inside the turbid medium and look at the fluctuations of the conversion efficiency when this scatterer probes different realization of disorder. All the following arguments holds also for incoherent two-photon processes such as two-photon fluorescence. One advantage of using fluorescent sources is that the life-time is also a probe of local density of states (LDOS) [20] and one can experimentally look into the relation between LDOS-fluctuations and mesoscopic intensity correlations.

7.2 Two-beam experiment

In this section, we introduce the setup for measuring intensity-intensity correlations inside random media by using nonlinear combination precesses. In this scheme, two weakly focused Guassian beams with the same frequency are incident on the same spot of a multiple-scattering slab. The second-harmonic light is generated inside the sample. A fraction of the scattered second-harmonic intensity is measured in reflection or transmission. Ito and Tomita have used a similar scheme to measure the spatial and temporal extent of the speckle inside multiple scattering medium [65]. They have compared their measurement results and found a very good agreement with a theoretical model based on the scalar wave approximation. In this section, we first show why using a scalar wave approximation is fundamentally wrong for such an experiment. In the following section, we show how the specific choice of the analyzed material could have influences their observation and brought the experimental results close to the prediction of a scalar treatment.

7.2.1 Underlying theory

Following the formalism introduced in section 2.3, we first look at the the scalar model. The amplitude of the wave-functions corresponding to each of the impinging beams are denoted by complex variables $\psi_{1\omega,a}(\mathbf{x})$ and $\psi_{1\omega,b}(\mathbf{x})$ at position $\mathbf{x}$ inside the sample. For simplicity, we omit the position dependence in the following short calculation, noting again that the medium is statistically homogeneous, and averaging over position is the same as averaging over realizations of disorder.

Following Eq. (2.43), for the second-harmonic polarization density generated at any position inside the sample we have

$$p_{2\omega,a+b} = \tilde{t}(\psi_{1\omega,a} + \psi_{1\omega,b})^2. \tag{7.3}$$

with the subscript $a+b$ denoting the total yield in presence of both impinging beams. For the moment, we have assumed that the nonlinear susceptibility tensor can be replaced by a scalar. The second-harmonic source intensity at each point reads

$$\begin{aligned} J_{2\omega,a+b} &\equiv \bar{p}_{2\omega,a+b} p_{2\omega,a+b} \\ &= |\tilde{t}|^2 (\bar{\psi}_{1\omega,a} + \bar{\psi}_{1\omega,b})^2 (\psi_{1\omega,a} + \psi_{1\omega,b})^2 \\ &= |\tilde{t}|^2 [I^2_{1\omega,a} + I^2_{1\omega,a} + 4 I_{1\omega,a} I_{1\omega,b} \\ &\quad + 2(I_{1\omega,a} + I_{1\omega,b})(\bar{\psi}_{1\omega,a}\psi_{1\omega,b} + \bar{\psi}_{1\omega,b}\psi_{1\omega,a}) + \bar{\psi}^2_{1\omega,a}\psi^2_{1\omega,b} + \bar{\psi}^2_{1\omega,b}\psi^2_{1\omega,a}]. \end{aligned} \tag{7.4}$$

Note that the source intensity is not yet averaged over realizations of disorder or position. The terms in the last line of equation (7.4) do not survive the ensemble averaging (or integrating over an area much larger than the speckle size), except for the trivial case that the impinging beams are exactly overlapping. Using the definition of mesoscopic correlation functions $C^{(1)}$ and C_0, we can write down, up to the first order in inverse scattering strength, the the following identities:

$$\begin{aligned}\langle I_{1\omega,a}^2\rangle &= (2+C_0)\langle I_{1\omega,a}\rangle^2,\\ \langle I_{1\omega,b}^2\rangle &= (2+C_0)\langle I_{1\omega,b}\rangle^2,\\ \langle I_{1\omega,a}I_{1\omega,b}\rangle &= (1+C_{ab}^{(1)}+C_0)\langle I_{1\omega,a}\rangle\langle I_{1\omega,b}\rangle.\end{aligned} \tag{7.5}$$

We have used the facts that $C_{aa}^{(1)} \equiv 1$ for all a and C_0 has an infinite range. In the experiment, the second-harmonic signals V_a and V_b are measured when beam b and a are blocked respectively. These signals (voltages) are directly proportional to the second-harmonic source intensity if we consider the second-harmonic light is not depleted. This is a valid assumption since the medium is not absorbing and the second-harmonic intensity is much smaller than the fundamental intensity. Since the propagation of second-harmonic light from the point of creation to the detector is completely linear, the proportionality factor is independent of the impinging beam and is solely determined by the instrument response function. The collective signal V_{a+b} is measured when both beams are incident on the sample and illuminating the same volume in space. Considering the ensemble average of Eq. (7.4) and using identities (7.5) we get

$$V_{a+b} = V_a + V_b + \frac{4(1+C_{ab}^{(1)}+C_0)}{2+C_0}\sqrt{V_aV_b}. \tag{7.6}$$

From this experiment, C_0 can be measured when $C_{ab}^{(1)} \to 0$.

7.2.2 Beyond the scalar approximation

Light waves are not scalar. Yet, in most of the experiments regarding random media in the linear regime, the polarization is scrambled and most of the intensity measurements can be close to perfectly modeled by a scalar treatment. The situation is different for nonlinear random media, since the polarization shows up directly in the conversion process and hence manipulates the intensity of the higher harmonics. For the case of second-harmonic generation, the converted light is determined by the tensorial nonlinear susceptibility at each point:

$$\mathbf{p}_{2\omega}\cdot\hat{\mathbf{u}}_i = \sum_{j,k}\chi_{ijk}^{(2)}(\mathbf{\Psi}_{1\omega}\cdot\hat{\mathbf{u}}_j)(\mathbf{\Psi}_{1\omega}\cdot\hat{\mathbf{u}}_k), \tag{7.7}$$

with $\hat{\mathbf{u}}_i$ the unit vector along each Cartesian coordinate. The susceptibility tensor depends both on the microscopic material properties and the geometry of the scatterer. Its determination, already a challenge for single crystals, becomes very complicated when the surface to volume ratio increases as in porous or powder structures. Therefore, one has always to resort to very simplified approximations. One such approximation is to consider a nonlinear point scatterer with isotropic internal polarizability.

Interestingly, even with such a simplification, the result of vectorial treatment for the two-beam experiment introduced above will be different from the scalar case. For a vectorial electric field, the electric field from each source should be added vectorially before taking its square value. This summation incorporates the angle between their polarizations θ, which is well-defined at each point of space and moment of time, but varies rapidly both in time and space. Instead of Eq. (7.3), we will get

$$p_{2\omega,a+b} = \tilde{t}(\psi^2_{1\omega,a} + \psi^2_{1\omega,b} + 2|\mathbf{\Psi}_{1\omega,a}||\mathbf{\Psi}_{1\omega,b}| \cos\theta). \tag{7.8}$$

For the second-harmonic source intensity, after the ensemble averaging and omitting the oscillatory terms, we have

$$\langle J_{2\omega,a+b}\rangle = \langle I^2_{1\omega,a}\rangle + \langle I^2_{1\omega,b}\rangle + 4\langle I_{1\omega,a} I_{1\omega,b}\rangle\langle\cos^2\theta\rangle. \tag{7.9}$$

The averaging for $\langle\cos^2\theta\rangle$ must be performed over the unit sphere with a proper weighting. Assuming a homogeneous distribution for θ, this average equals $\frac{1}{3}$. For the more general case of an arbitrary nonlinear susceptibility tensor, this averaging must be weighted, incorporating the components of the tensor, Due to the quadratic averaging, the average can never be less that the value from the isotropic case (due to the Cauchy Schwarz inequality). In the most general case, we can summarize the results from the two-beam experiment on any sample with the following expression

$$V_{a+b} = V_a + V_b + C_X\sqrt{V_a V_b}. \tag{7.10}$$

with C_X a non-universal and bounded quantity,

$$\frac{2}{3} \leq C_X \leq 2, \tag{7.11}$$

which includes both the material structure and mesoscopic effect. Separation of these two effects in C_X is in general not possible except for the very simplified cases like isotropic point scatterers where we have considered in Eq. (7.4) or a highly uni-axial susceptibility tensor, which we shall discuss further in section 7.4.3. Note that for this result, only diffuse interference is considered. The interference of coherently propagating beams can enhance the signal by a factor 16, because all the terms in Eq. (7.4) will then survive averaging. For the isotropic model in the diffuse regime the results is

$$C_X = \frac{4(1 + C^{(1)}_{ab} + C_0)}{3(2 + C_0)}. \tag{7.12}$$

Given a sample which follows this approximation, it should be possible to directly measure mesoscopic C_0-correlations with our two-beam method. For other types of samples, this experiment can be a great tool for characterizing the internal structure of the sample by measuring the structure-dependent C_X quantity.

7.3 Experimental settings

The outline of the experimental setup is schematically drawn in Fig. 7.1. Light from a 5-ns pulsed tunable Nd:YAG laser (Opolette, Opotek) is split in two paths and overlapped again by a second beam-splitter. One of the mirrors is put on a translation state. A lens after the second beam-splitter focuses light on the sample at its focal plane. With this configuration, the displacement of the mirror will result in changing the incident angle for one of the beams on the sample. The beam polarization in each path can be varied independent of the other one. The samples are few tens of microns thick and opaque, but

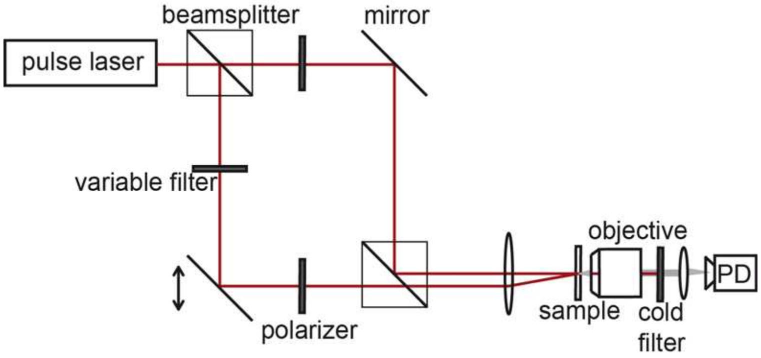

Figure 7.1: Schematic of the setup used for the two-beam experiment. Two beams of the same cross section with controlled intensity and polarization are incident on the sample at slightly different angles. The second-harmonic signal generated inside and transmited through the sample is collected by an objective and detected by a photo-diode after proper filtering.

the substrate is transparent. The second-harmonic light generated inside the sample is detected in transmission. The transmitted light at the fundamental frequency is filtered by a cold-glass filter. The second-harmonic signal is collected by an objective and focused on a sensitive photo-diode. Saturation effects are avoided and the voltage of the diode is linearly proportional to the total second-harmonic intensity generated in the sample.

To extract the C_X parameter introduced in the previous chapter, a series of measurements are performed for each configuration of direction and polarization of the two incident beams. This series includes varying the intensity of one of the beams and recording three values of V_a, V_b, and V_{a+b} for each intensity, after correcting for the dark signal. The C_X parameter is equal to the slope of the line fitted to the measurement points $(V_{a+b} - V_a - V_b)$ plotted versus $\sqrt{V_a V_b}$.

Various samples have been investigated with this setup. Most of the results presented in this chapter are measured on porous GaP samples with different scattering strengths. The samples are fabricated for this experiment using the method of photo-electrochemical etching [102]. The thickness and scattering strength of all the samples are characterized by using SEM images and coherent backscattering measurements. A summary of the samples characterization is presented in table 7.1.

7.4 Results and discussion

The first control experiment was to check the polarization dependence that was discussed in this chapter. In this experiment, the C_X parameter is measured as a function of the angle between the two incident beams for parallel and crossed polarizations. The results are shown in Fig. 7.2. For the crossed polarization, $C^{(1)}$ is zero for any angle and thus the C_X is independent of the angle between the two beams. If C_0 could have been extracted from C_X, this observation would have been the strongest evidence ever seen for the infinite range of C_0-correlations . For the parallel polarization, at large angles, the effect of $C^{(1)}$ vanishes again and the enhancement falls on the value observed for the cross-polarization case. At small angles however, the enhancement due to $C^{(1)}$ can clearly be seen as an increase in the enhancement. At even smaller angles, close to zero, the interference of coherent beams

Tag	$L(\mu\text{m})$	$k\ell(600)$	$k\ell(1200)$	C_X	Serial
D2	51 ± 2	4.9	11.4	1.21 ± 0.03	
D4	43 ± 2	1.3	4.4	1.08 ± 0.03	
F2	35 ± 2	2.1	10.6	1.01 ± 0.04	
S1	52 ± 1	0.46	3.4	1.07 ± 0.07	S1080109
S2	24 ± 1	0.8	3.1	0.93 ± 0.02	S1080121
S3	83 ± 1	0.89	5.1	1.43 ± 0.06	S1080124
S4	109 ± 2	20.5	29	1.39 ± 0.02	S1080218
S5	70 ± 1	8.6	13	1.16 ± 0.03	S1080226
S6	99 ± 2	10.6	17.8	1.25 ± 0.03	S1080227
S7	56 ± 1	3.2	7.3	1.25 ± 0.04	S2080109
S8	43 ± 1	4.5	5.7	1.05 ± 0.03	S2080226
S9	90 ± 2	13.3	19.5	1.31 ± 0.02	S2080227
S10	96 ± 2	12.9	15.5	1.40 ± 0.04	S3080227
S11	33 ± 1	4	5.5	1.00 ± 0.04	S3080228
S12	60 ± 1	0.65	4	1.22 ± 0.08	S4080114
S13	38 ± 1	6.8	9	1.15 ± 0.03	S5080228

Table 7.1: Summary of specifications for the GaP samples that are analyzed by the two-beam method. The thickness of etched porous-GaP layer is derived from scanning electron micrographs. The mean free paths are estimated from total transmission measurements. The resulted values are in agreement with measurements using white-light EBS setup [99] within fifty percent accuracy.

wins over the diffuse interference effects and a rapidly fluctuating interference pattern is observed. This interference pattern is not fully resolved due to its sensitivity to the incident beam jitters, but in theory the observed enhancement (or suppression) should be fluctuating between -2 and 14, when the angle is approaching zero.

In the second experiment, the polarization of collinear incident beams are set to crossed and C_X is measured on a single GaP sample as a function of wavelength. The results are presented in Fig. 7.3. Although, it is not easy to model this result, this observation clearly shows the non-universal nature of C_X. Performing the same experiment on the laser powder (LiNbO_3) results in even a higher value of C_X, even though this sample has a longer scattering mean free path than porous GaP. Once again this observation is a sign of material dependence of C_X. In section 7.4.3, we will discuss our understanding of the underlying physics that explains the difference between the GaP and LiNbO_3 that can partly explain the measured enhancements.

7.4.1 Dependence on scattering strength

If the tensorial form of nonlinear susceptibility was spectrally uniform, the results shown in Fig. 7.3 could have been used to extract the dependence of C_X on scattering strength, since we know that the mean free path of GaP is highly dispersive due to its porous structure. But the same geometrical effects of the pore shapes that are responsible for the dispersive mean free path can also affect the effective nonlinear susceptibility. To better understand this dependence, we have performed the diffuse nonlinear interference measurement on several GaP samples with various scattering strength (see table 7.1) at the same wavelength. The results are presented in Fig. 7.4. Although the resulted points are largely dispersed in the graph, the overall trend shows reduction of C_X for smaller scattering strength. We should

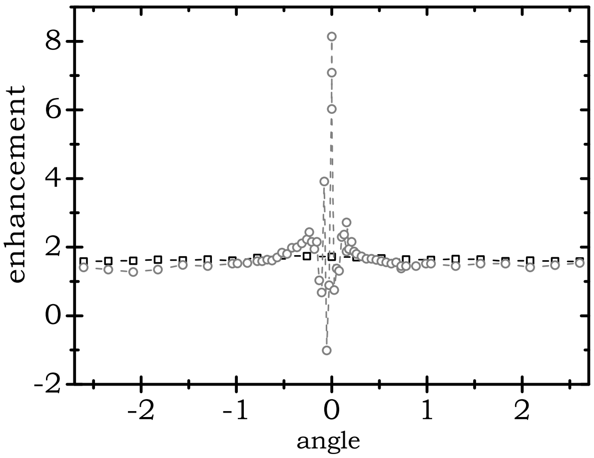

Figure 7.2: Dependence of the two-beam nonlinear enhancement signal on the angle between the incident beams for parallel (circles) and crossed (squares) polarizations for a typical sample. The large fluctuations in the for PP case are due to direct interference between the incident beams. In principle, the signal should oscillate and can be maximum 14 and minimum -2. These fringes are not completely resolved in this measurements due to the focusing of the incident beams. The flat signal for CP case indicated to the infinite range of C_X. The enhancement is normalized to the signal of a single beam and the angle is measured in degrees.

note that if mesoscopic C_0-correlations were to be observable in these measurements, their contribution should have increased at smaller values of $k\ell$. Therefore, we conclude that the measured dependence of C_X on scattering strength is dominated by the structural dependence of the susceptibility tensor on the variations of pore geometry and cannot be exclusively representing a mesoscopic effect.

7.4.2 C_X measurement in a single shot

The C_X parameter is directly connected to the internal structure of nonlinear scattering centers. Meanwhile, due to its determination in a relative measurement and natural sampling of many positions and directions in the turbid sample, its determination can act a robust indicator for the changes in the microscopic composition of the scatterers. This property can be used to monitor the microscopic crystalline structure of for examples drugs, which have a vital role in the effectiveness of a medical treatment. Therefore, it may be favorable to introduce a method that measures C_X in a single shot, instead of the three successive measurements that were introduced above. This single shot technique can also be used to monitor evolving samples like suspensions. Due to the short duration of the incident pulses, the two-beam experiment can function as a stroboscopic technique to monitor the dynamics of physical or chemical reactions in the suspension.

The main idea of this one-shot setup in schematically drawn in Fig. 7.5. In this setup, the incident beams are extended along one of the beam axes using cylindrical lenses. The elipticity axes of the two beams make an angle with each other such that the central part of the ellipses overlap while the ends do not. This way, the signal at the non-overlapping regions can be used as a reference for V_a and V_b (after spending adequate effort on profile

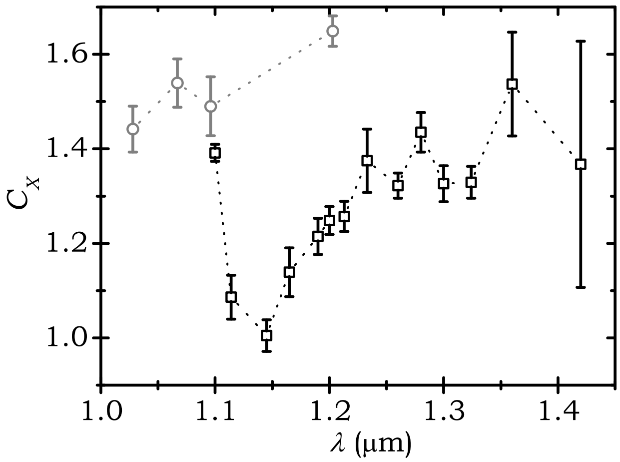

Figure 7.3: Dependence of C_X on wavelength for porous GaP sample S6 (squares) and $LiNbO_3$ powder (circles). The behavior is attributed to a mixture of both structural dependence of nonlinear susceptibility and multiple-scattering effects.

corrections), while the signal at the center is a measure for V_{a+b}. Figure 7.5 shows an schematic drawing of such a measurement and Fig. 7.6 shows one typical measurement aside with the relevant cross-cuts.

Comparing the results from this one-shot experiment with those from the Mach-Zender-type one shows a quantitative good agreement. When combined with more advanced microscopy techniques, this experiment can provide structural information that are not accessible in the conventional second-harmonic microscopy experiments. In some sense, the C_X measurement is the nonlinear extension of interferometric phase-contrast imaging in linear microscopy.

7.4.3 Applicability of the scalar model

Finally, it is worth discussing the use of a scalar model for non-linear diffuse interference. In the introduction of this chapter, we mentioned that Ito and Tomita [65] have used a similar two-beam experiment in the past to measure the $C^{(1)}$ correlations inside a sample of laser powder and in fact used a scalar model to fit their data. Contrary to our statement that a scalar model is wrong for the interpretation of this experiment, a relatively good agreement has been found between their measurements and the scalar model that was used. The question arises: how is that possible?

We think the explanation for this apparent confusion is in the very choice of sample that was used in that article. They have used $LiNbO_3$, which has the following bulk nonlinear susceptibility tensor:

$$d^{\mathrm{LiNbO_3}} = \begin{pmatrix} 0 & 0 & 0 & 0 & 14 & -7.4 \\ -7.4 & 7.4 & 0 & 14 & 0 & 0 \\ 14 & 14 & -98 & 0 & 0 & 0 \end{pmatrix}. \tag{7.13}$$

The element $d_{33} = 2\chi_{333} = -98$ is much larger than the other elements which means the second harmonic conversion efficiency is much higher when the polarization of the two fun-

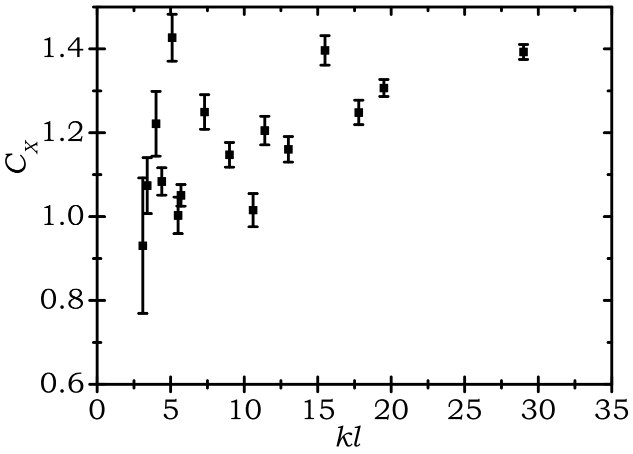

Figure 7.4: Dependence of C_X at $\lambda = 1200$ nm on scattering strength for several Porous GaP samples. The scattering strength is estimated by measuring the total transmission.

damental photons are aligned with the 3rd lattice vector. This means that the crystal, effectively, acts as a local polarizer that filters those photons responsible for (efficiently) generating the second harmonic photon. This picture, rehabilitates the scalar model for describing their experimental data. We have also measured on the some LiNbO$_3$ powders. A comparison with porous GaP is made in Fig. 7.3. We have also found a higher enhancement than the prediction of an isotropic vector calculation, inline with the literature. The difference between our final result and two, the value that comes out the scalar model, may be related to the small size of powder grains or the emergence of the vectorial nature of conversion process due to the other non-zero elements of the nonlinear susceptibility tensor.

Having looked at actual material properties of LiNbO$_3$, it is worth discussing the results for GaP. For the bulk of this substance, the nonlinear susceptibility tensor has a completely different structure:

$$d^{\mathrm{GaP}} = \begin{pmatrix} 0 & 0 & 0 & 16 & 0 & 0 \\ 0 & 0 & 0 & 0 & 16 & 0 \\ 0 & 0 & 0 & 0 & 0 & 16 \end{pmatrix}. \tag{7.14}$$

In fact, the second harmonic conversion in bulk GaP has a rotationally symmetric nature. All the conversion processes can be described by combining two photons with perpendicular polarization into the the third second-harmonic photon with polarization again perpendicular to both fundamental photons. The cyclic permutation of polarization directions does not influence the efficienty; $\chi_{123} = \chi_{231} = \chi_{312}$. This property, makes GaP a very suitable candidate for using an isotropic vector model, which shows the minimum $C_X = \frac{2}{3}$.

Although, from our data, the GaP results are closer to the theoretical prediction from isotropic vector model than for other substances, it is short of quantitative agreement. This observation may have several reasons. The most probable explanation is the porosity of our samples, which introduces a large surface to balk ratio and causes deviation from the bulk nonlinear susceptibility. If these structural factors could have been measure independently, one could extract multiple-scattering effects from these results. Therefore, other two-beam experiments on single nano-crystals may be needed to make a firm conclusion about this

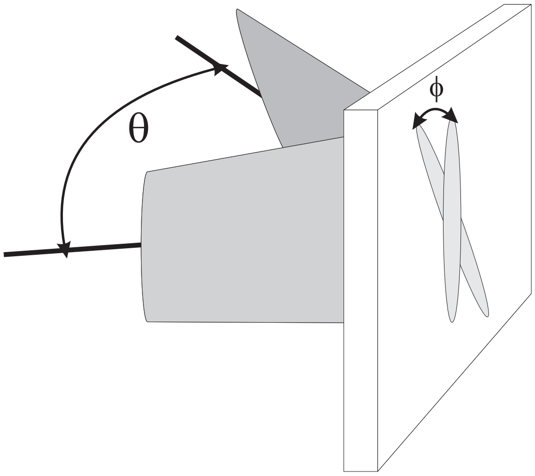

Figure 7.5: Schematics of the single-shot C_X measurment. The incident beams with elliptical cross-sections overlap in part of their profile due to their relative orientation. The second harmonic signal is recorded in transmission using a sensitive EM-CCD camera.

observation.

7.5 Final remarks

In this chapter, we have presented a method based on second harmonic generation to study mesoscopic intensity correlations inside multiple scattering media. We have performed several measurements which are consistent with the theoretical prediction but stayed short of disentangling the mesoscopic part from the intrinsic material properties that influence the output of our method. However, these results are enough for proving the shortcomings of a scalar model. By carefully looking into the nonlinear susceptibility tensor, we have shown that the scalar model holds only for very specific cases.

The next steps for this research involve the investigation of colloidal suspensions, for which the scattering strength can be varied without changing the structure of individual scatterers. This experiment would be the only way in our opinion that can really split the mesoscopic effects from the structural ones. A helpful trick would be to use the sum-frequency generation of two input beams with different frequencies, instead of second harmonic generation. This way, the overlap signal can be spectrally split from the signal of individual beams and therefor perform the actual measurement “background free”. Using the two-photon fluorescence instead of the coherent second harmonic signal will also have the benefit of comparing the correlation measurements with the lifetime variations of the dye molecules and by that further exploring the relation between LDOS fluctuations and mesoscopic C_0-correlations .

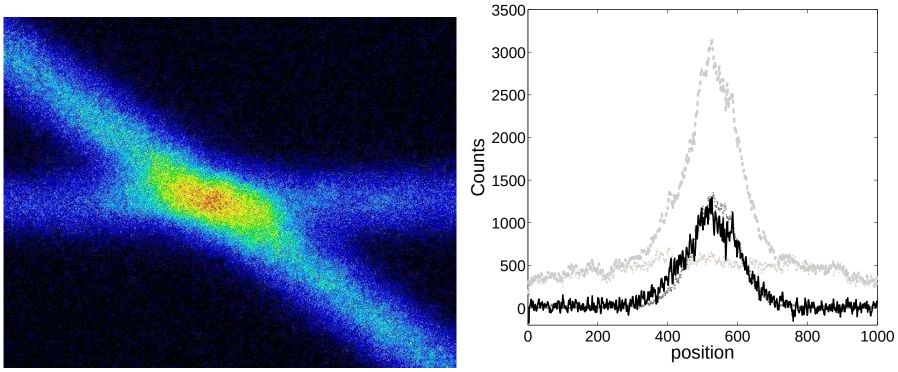

Figure 7.6: Left: A typical "single-shot" measurement image from a 100-μm thick slab of porous GaP. Right: The horizontal cross-cut of the measured data with the total SHG signal shown with dashed gray line and SHG signal of each individual beam shown by light and dark gray dots. The black line shows the difference between the total signal and the sum of SHG signal from two beams when measured individually.

Afterword

In my viewpoint, as limited as it is, getting a PhD is not just spending few years on advanced research in order to gain more skills and knowledge on top of a student's education. As Ad tells to-be-scientists in his survival guide lectures, our goals should not be "to have a large numbers of papers or citations, to lead a larger and larger group, or to have a large office". Our goal must be "to become a world-class scientist". Getting there certainly takes much more than reading a lot, working day and night, or "to shut up and calculate", to quote Feynman. Sometimes you need to speak out, even against the big shots. Other times you should listen and admit to your misunderstandings. Overall, I can say, it takes the right attitude. I am very glad that I am getting promoted in a group with a holistic approach towards training a scientist. Thank you Ad, thank you, for teaching me exactly what I needed to learn before I could think of starting a propitious scientific career.

In my high-school years, I was fascinated by building electromechanical systems, for example robots. To my father's disappointment, I never showed any interest in continuing my studies in medicine, because I wanted to study engineering and become an "inventor", whatever that represented for a teenager. To give a clue, Graham Bell and Edison were much more fascinating characters for me than Einstein, Hawking, or Louis Pasteur. It took a year of pure fun and fundamental physics courses for me to become interested in studying physics for its own sake. Chosen for the Iranian team for participation in the International Physics Olympiad, I could enjoy a full year of special training, instead of reciting boring things, like Arabic grammar textbooks, for the notorious university entrance national exam. Those courses were among the best physics lectures I have ever followed, and all taught in the cleverest manner. I would like to thank Amir Aghamohammadi, the late Masood Alimohammadi, Mohsen Alishahiha, Mahmoud Bahmanabadi, Reza Ejtehadi, Mohammad Khorrami, Ahmad Shirzad, Shahram Shariati, and Hossein Tavalla, for teaching to me fundamentals of physics in the most elegant and original way. I lost my interest in engineering, again to my father's disappointment, and got fascinated by the discipline of experimenting, modeling, and solving. So I continued studying "just physics".

At Sharif university, I had the pleasure of taking most of my courses with the same team of lecturers from the Olympiad year, plus other excellent teachers, among who I like to mention Hessam Arfaei, Vahid Karimipour, and Shahin Sheikh-Jabbari. I remained active in the Olympiad training camp, the so-called Young Scholars Club, where I became a lab supervisor for the forthcoming teams. There I gained invaluable experience in designing ten-dollar experiments for measuring almost any physical quantity. I did not take a single practical course at the university because I hated their precooked recipes and fill-in answer sheets. While in YSC, I even got the chance to start my own elementary research laboratory, where I studied non-coalescence of liquid jets, with a couple of colleagues. We were inspired by observing the dance of floating droplets when one knocks skillfully on a PET bottle. We used to call it the Khorsand effect. At a workshop in Zanjan in 1998, I showed some photographs of my experiments to Fereydoon Family (Emory university), who brought me in contact with Sidney Nagel (University of Chicago) and via him with Howard Stone, who was at Harvard at the time. The enthusiastic reaction of Howard to my simple-minded email was beyond any expectation. Thirteen years have passed and I still clearly remember that sweet excitement of frequently receiving those green-hashed pockets from Harvard. They were full of hand-picked articles and study materials, with hand-written notes of Howard on them. Just imagine for a moment, a prominent researcher at Harvard, takes the emails of an 18-year-old student from nowhereland so serious that he would go to the library, copy parts of a book of Lord Rayleigh, and send it to him halfway round the globe. In the past five years, I have seen several prominent scientists, and a handful of Noble laureates. None of them impressed me as much as Howard Stone did. For me, he is the role model for caring, giving, and not self-centered scientific character. If ever I might become a world-class scientist, I wish to be like Howard.

With the self-confidence I gained from Howard's response, and with the support of Shahram Shariati, I wrote my "results" and put them on Arxiv (arXiv:physics/9908006). Anyone who reads that piece of text, including the current me, will find it plainly laughable. It would have perhaps disappeared in less than a day if the Arxiv moderation system was active at the time. I still feel humbled by the fact that Howard did not laugh at it and even reviewed that manuscript. Later that year, Antonio Barone (University of Naples), who was visiting Tehran for a conference on Superconductivity, took another batch of photographs from our experiment to Rudolfo Monti and Raffaele Savino. They invited me to their lab in Naples, which was named after Carlo Marangoni. I spent a summer in their lab and we achieved quite exciting results but I ran out of time before we could compose an article about those results. Despite Raffaele's second invitation, I could not go back to Naples, because I had to suffer the mandatory military service. The very same bouncing droplets made it to the cover of PRL and Nature in 2005, after French researchers attributed sort of particle-wave duality to them.

Around the same time, I started to discover other interests of mine ranging from industrial design to entrepreneurship. Those explorations, perhaps driven by freedom from the pressure of college years and a desire for independence, distracted me from physics research. I was trying to become a high-tech designer of water fountains, and my role model was Mark Fuller (Wet Design). For that I needed capital investment. I decided to sell some of my home-made laminar fountains, but soon I found out that real business takes much more than just technical skills or novel ideas, especially in a developing country. Even a year of studying for an MBA could not turn my frustrating efforts to start a company into any level of success. With the emergence of a populist delusional government in 2005, any remaining glimmer of hope disappeared. Together with Bahar, we decided to try our chances elsewhere. The easiest way out for me was to get back to the university.

I have been asked several times why did I choose for University of Twente. The answer is again in the attentive character of a physicist, Wilfred van der Wiel. As far as I have seen, physicists being considerate is more like an exception than a rule, and as it happened such a person was, and still is, working in Enschede. To be frank, I did not even know where to look for Twente on the map when I was applying to several open PhD positions all over the Netherlands. Wilfred was the only person who let me know I need to obtain a masters degree first. He introduced me to the new track of Nanotechnology. Despite my very late application I got admitted and even was awarded the Shell Centenary scholarship. For that I have to thank Rik Akse, as well, who was very kind to accept my late application.

The style of the courses in the Nanotechnology track were very different from my previous experience of exercise intensive classical studies in Sharif. The multidisciplinary nature of those courses were encouraging me to think more of working in a big enterprize, or starting up a company. I even tried to continue studying for an MBA as a double track. At the time, prospects for finding a job in the western academia were looking so dim to me and I was not prepared to take another risk in my career. But it took just one session of fascination by another scientist with character to re-install me on my old track and initiate my quick transformation from an enthusiast for entrepreneurship into a traditionalist advocate of fundamental research. That guru later became my PhD-supervisor.

There is nothing very unconventional about the rest of my academic history, at least not so special for those who are familiar with Ad's personality. So I can simply continue these lines just like a classical acknowledgement. I like to thank all my teachers in Twente, especially Willem Vos and Allard Mosk from the Complex Photonic Systems (COPS). I had a very pleasant summer internship in Leiden. Eric Eliel gave me many opportunities for exploring and let me enjoy again the pleasure of investigating whatever was the most mysterious phenomenon. Dmitry Mazurenko was the initiator of my master project and after he left, Patrick Johnson took care of a very successful finish for it. Over the years, I learned that I should be very careful in answering Patrick's questions. Whenever he uses his special humble tone, he is exactly targeting the weakest point of my arguments. Our lunch group shrank to less than a half when Willem moved back to Twente, but all those Amsterdam-Twente migrations could not interfere with our heated east-west meetings. As a consequence, I never really felt the split from the Twentse COPS. Hereby, I thank all the past and present COPS members for all the friendly discussions we had.

The nanophotonics colloquium has a milder style of kneading the speaker, but can still be a tough experience for a newly joined member, specially if Ad is the chairman and that poor fellow is late. But that hard training has raised magnificently the quality of scientific presentations from AMOLF, in comparison with other institutes that I have visited. I would like to thank all the participating group leaders: Jaime Gomez Rivas, Femius Koenderink, Kobus Kuipers, Albert Polman, and Ad for their precious coaching. I learned a lot from the four European workshops I attended, for which I like to thank their organizers and also mention the most instructive lectures by Boris Altshuler, Immanuel Bloch, Roland Ketzmerick, and Jörg Kotthaus. Attending the courses taught by Jean-Sébastian Caux and Carlo Beenakker in the framework of DITP, partly satisfied my appetite for learning advanced theoretical methods. I also thank Florian Marquardt for teaching his quantum optics course in English and making all the videos accessible; I hope he does it more often.

I started experiencing the great opportunities brought by an international collaboration thanks to the open scientific attitude of Bart van Tiggelen and John Page. I think we are all very pleased about the outcome (chapter 5). On several occasions, I had very fruitful discussions with Sergey Skipetrov, but have not got the chance yet to be a coauthor of him. Yan Fyodorov and Sasha Ossipov dedicated all their time to the dipole chain discussions (chapter 4) when I was visiting Nottingham. For that work I also benefited from discussions with Femius Koenderink. My latest delocalized collaboration is perhaps the most exceptional one. It all started by exchanging questions via email with Florian Marquardt and Hakan Türeci and sharing ideas on a wiki website, where Li Ge joined in. It reached its climax when I was in Princeton, and we are yet to finalize our exciting conclusions. I like to thank Hakan and Li for their hospitality and Florian for his dedication.

The old AMOLF building was famous for its bridge, which was connecting the Bio side to the mostly-opticians corner. But south of the bridge was more socially *conton*ic than its north, and that was partly because of the large mass of phoscat-phogap alliance. Inside the group, however, was very entertaining especially at the time of no-merci productions. Ivan, Tijmen, Tom, Karen, Philip, Ivo, Bernard, Bart, Leon, Alex, and Merel were lampooned and now guess who is next? I should not forget to mention Otto, Willem T., Edwin, Frerik, Rajesh, Niels, and Danang who escaped getting the subject of this funny sport, and Elbert who could not leave without giving us a second chance. The new AMOLF building has more bridges, and the newer generations are more socializing with each other. However, the asocial phoscatters could not overcome the old tradition and kept their circle closed. The more recent custom of avocado-flavored phoscat lunches helped in reinforcing the barriers. However, I am sure I will miss all those joyful moments inside the circle, on the same day I leave the institute. Patrick, Paolo, Timmo, Ad, Bergin, Jochen, Ronald, and Ramy, your are an amazing group. Pierre, thank you for sharing your LaTeX markup for Feynman diagrams with me. I also would like to thank all the AMOLF personnel, especially the cool guys in the workshop and design room. I should specifically mention Iliya Cerjak and Dirk-Jan Spaanderman, who made a lot of my experiments possible, and whose profession I envy.

I like to exclusively thank Ramy for being my closest friend in the low lands. You were always there to help, when I needed it. Thank you Ramy for editing my broken Dutch text in the NTvN article on localization and the Dutch summary in this thesis with such a devotion. It was the most fun when we were working together in the lab. Timmo and Ramy, thank you for accepting to be my paranymphs with all the burdens attached to it.

Amsterdam is a great city, and it just fits our taste for living in uncrowded places. It is however large enough for one to always find something to amuse himself with. We couldn't have enjoyed the livelihood of Amsterdam without the friendly UvA J/Kers. I also like to thank Theo and Claudia who were always very kind to us. Thanks to their friendship with Piet we could settle down in the fantastic neighborhood of Bredeweg, with its compassionate tenants and their incredible Queen's day festival. We could also continue experiencing the great taste of Persian cuisine, which tastes best when served in crowded gatherings, thanks to our Iranian friends in Amsterdam and Delft; dametoon garm.

Despite our strong attachment to Amsterdam, we have to leave it, hopefully just for a short while. The globalization of the academic marketplace, have its own pro's and cons. Whoever is determined to stay in it has to make sacrifices. However, with a new group comes the opportunity of creating synergy between what you have learned and what others have accomplished. I like to thank Jack Harris, Peter Lodahl, Niek van Hulst, and Vahid Sandoghdar for the invitation to their labs. I have special thanks for Gerd Leuchs, who graciously helped us with our dual career issue. Thanks to Vahid's considerate support and sympathetic help of Irene Weinzierl, our move to Erlangen is happening more smoothly than we could have imagined.

Finally, I like to show gratitude to my parents for their immense support in all stages of my life, even when they were not fully satisfied with my choices. I thank Telli and Enrico for their compassionate love for Soline and letting her experience the joy of being with aunts and uncles, outside her parents' homeland. The cheerful times we spent together in Italy, France, Rotterdam, and Amsterdam contain the best of our memories. My adorable Soline, you have delighted my life with pride and joy. I am so proud of you that I have left behind all my greed for recognition. And my dearest companion in life, Bahar, it is getting a decade since we started to share all our contentment and grievances, and I cannot imagine living a single day otherwise. You have been the most gracious friend I have ever had. Together, we came a long, and sometime extremely tremulous, way. You have always supported my causes and covered my shortcomings. With a giving and capable friend like you, one can never fail. And now that we have an angel with us that abates all our tiredness in a blink, I can see nothing but a hilarious and bright future for our little family. Thank you for your wholehearted support in difficult times and your delightful company in joyful moments. Thank you for being you.

Sanli
Amsterdam, 2011

Summary

The main topic of this dissertation is studying the propagation of waves in disordered materials. More specifically, we have studied, theoretically and experimentally, the manifestations of Anderson localization in various systems using classical waves, such as light and ultrasound. Anderson localization refers to the suppression of wave diffusion in random media due to interference effects. This conductor to insulator transition was discovered fifty years ago by Philip Anderson in the context of electronic conductivity of metals.

Over the past decades, Anderson localization have attracted interest far outside its original scope of definition: as far as seismology and biomedical imaging. Most of the theoretical developments on the understanding of this phenomenon have been made by the condensed-matter physicists. Meanwhile, many important experimental achievement have been provided by the research on classical waves. However, a unified picture that captures both the experimental realities and theoretical descriptions of this phenomenon, for all types of waves, is still missing. Unfortunately, some existing interpretations of Anderson localization, even as reported next to experimental results, have been very mystified and sometimes superficial. Several claims have been made related to the observation of localization-related phenomena based on inadequate evidence or sometimes erroneous comprehension of the physics behind it.

On the theoretical side, two main approaches have been used, side by side, for studying Anderson localization. In the multiple scattering formalism, the propagation of waves is described in terms of scattering centers and Green functions. Light propagation in complex photonic structures can be described by a summation over several scattering paths. This summation is mathematically treated with diagrammatic techniques, which are commonly used in field theory. This approach successfully describes diffusion. It also sets the foundation for the self-consistent theory of localization, which includes the interference effects to an extent that the classical diffusion breaks down. This technique has proven to be very successful in describing several experimental transport measurements, which often approach localization transition from the diffusive side.

The second approach to studying waves in disordered media is to see the whole system as a matrix. This matrix can either be the Hamiltonian or the scattering matrix. For a disordered system, the entries of this matrix look like random. It is assumed that the statistical properties will not change if the entries are taken as completely random. This is the main concept behind random matrix theory (RMT). In contrast to the multiple-scattering formalism, which can be seen as the reductionist approach to studying waves in disordered media, random matrix theory is a holistic approach. In an RMT treatment, one often overlooks all the details of the system under investigation. Despite the apparently loose justification of RMT basic assumptions, the predictions are often generally applicable and surprisingly successful in reproducing the experimental results, even for very complicated systems.

The first two chapters of this dissertation are dedicated to introducing the basic foundations of multiple-scattering (chapter 2) and random matrix (chapter 3) theories. Books have been written about these subjects, and there was neither the intention nor the capacity of presenting a thorough introduction. Chapter 2 helps the reader to follow the derivation of two new theoretical results that are performed by us, using a multiple scattering approach. The first result is the equivalence of variations in frequency with variation in effective refractive index. This equivalence sets the basis for the method of Refractive Index Tuning, which is described in chapter 6 and supported by experimental results. The second theoretical result is the relation between so-called C_0 fluctuations and the efficiency of second-harmonic generation in random media. This equivalence was the motivation behind the experiments that are described in chapter 7. Both experiment were originally designed in relation with the idea of analyzing samples in the localized regime.

In chapter 4, the intensity distribution of electromagnetic polar waves in a chain of near-resonant weakly-coupled scatterers is investigated theoretically and supported by numerical analysis. Critical scaling behavior is discovered for part of the eigenvalue spectrum due to the disorder-induced Anderson transition. This localization transition (in a formally one-dimensional system) is attributed to the long-range dipole-dipole interaction, which decays inverse linearly with distance for polarization perpendicular to the chain. For polarization parallel to the chain, with inverse-squared long-range coupling, all eigenmodes are shown to be localized. A comparison with the results for Hermitian power-law banded random matrices and other intermediate models is presented. This comparison reveals the significance of non-Hermiticity of the model and the periodic modulation of the coupling

The experimental observation of strong multifractality in wave functions close to the Anderson localization transition in open three-dimensional elastic networks is reported in chapter 5. The first observation of localization in these samples were reported in a prior publication. Our second look at the measurements provided the first experimental indication of multifractal structure of waves near the localization threshold and confirmed the nontrivial symmetry of the multifractal exponents, which was theoretically conjectured before.

Samenvatting

Het belangrijkste onderwerp in dit proefschrift is de voortplanting van golven in wanordelijke materialen. Wij hebben, zowel theoretisch als experimenteel, uitingen van Anderson lokalisatie bestudeerd met klassieke golven, zoals licht en ultrageluid. Anderson lokalisatie verwijst naar de onderdrukking van diffusie in wanordelijke materie als gevolg van interferentie. Deze overgang van geleider naar isolator werd 50 jaar geleden ontdekt door Philip Anderson in het kader van elektronentransport in metalen.

In de afgelopen 50 jaar heeft Anderson lokalisatie veel aandacht gekregen in wetenschapsvelden die zich ver buiten zijn oorspronkelijke kader bevinden: bijvoorbeeld in de seismologie en biomedische beeldvorming. Het merendeel van de theoretische ontwikkelingen die tot een beter begrip van dit fenomeen hebben geleid, zijn gedaan door vaste-stof-fysici. Veel belangrijke experimentele observaties zijn echter gedaan door onderzoek met klassieke golven zoals microgolven en geluidsgolven. Nog steeds is er geen eenduidig beeld dat zowel de experimentele realiteit als de theoretische beschrijvingen van dit fenomeen voor alle soorten golven beschrijft. Helaas zijn sommige interpretaties van Anderson lokalisatie zeer oppervlakkig. Verschillende claims zijn gemaakt met betrekking tot de observatie van lokalisatieverschijnselen op basis van onvoldoende bewijs of verkeerd begrip van de onderliggende fysica.

Aan de theoretische kant, worden twee belangrijke benaderingen naast elkaar gebruikt voor het bestuderen van Anderson lokalisatie. In het meervoudige verstrooiingsformalisme, wordt de voortplanting van golven beschreven in termen van verstrooiers en Green functies. Voortplanting van licht in complexe fotonische structuren kunnen daardoor beschreven worden door een sommatie over meerdere verstrooiingspaden. Deze sommatie wordt mathematisch beschreven met diagrammatische technieken, die gewoonlijk worden gebruikt in veldtheorieën. Deze aanpak beschrijft diffusie zeer goed. Het vormt ook de basis voor de zelf-consistente theorie van lokalisatie, die interferentie-effecten op dusdanige wijze meeneemt dat klassieke diffusie wordt afgebroken. Deze wiskundige techniek is zeer succesvol gebleken in het nauwkeurig beschrijven van experimentele transportmetingen, mede doordat deze experimenten net als de theoretische beschrijving de lokalisatie-overgang vanaf de diffuse kant benaderen.

De tweede theoretische benadering aan de studie van golven in wanordelijke media is het hele systeem te beschouwen als een matrix. Deze matrix kan de Hamiltoniaan of de verstrooiingsmatrix representeren. Voor een wanordelijk systeem, lijken de afzonderlijke elementen van deze matrix willekeurig. In de theorie wordt aangenomen dat de statistische eigenschappen niet zullen veranderen als de elementen volstrekt willekeurig worden gekozen. Deze aanname is het belangrijkste concept achter de zogenaamde Random Matrix Theorie (RMT). In tegenstelling tot het meervoudig verstrooiingsformalisme, dat kan worden gezien als een reductionistische benadering van het bestuderen van golven in wanordelijke media, vormt de RMT een holistische benadering. In een RMT beschrijving worden de meeste microscopische details van het systeem verwaarloosd. Ondanks deze ogenschijnlijke ad-hoc rechtvaardiging van de RMT uitgangspunten, zijn de voorspellingen vaak algemeen toepasbaar en verrassend succesvol in het reproduceren van experimentele resultaten, zelfs voor zeer complexe systemen.

De eerste twee hoofdstukken van dit proefschrift zijn gewijd aan de introductie van de grondslagen van de meervoudige verstrooiingstheorie (hoofdstuk 2) en de random matrix theorie (hoofdstuk 3). Hoofdstuk 2 helpt de lezer om de afleiding van twee nieuwe theoretische resultaten te begrijpen die door ons worden afgeleid met behulp van een meervoudige verstrooiingsaanpak. Het eerste resultaat is de overeenkomstigheid tussen variaties in de frequentie en variaties in de effectieve brekingsindex. Deze overeenkomstigheid vormt de basis achter de experimentele methode van Refractive Index Tuning (RIT). Deze methode wordt beschreven in hoofdstuk 6 en ondersteund door experimentele resultaten. Het tweede theoretische resultaat is de relatie tussen de zogenaamde C_0 correlaties en de efficiëntie van de tweede harmonische generatie in wanordelijke media. Deze relatie vormde de motivatie voor de experimenten die worden beschreven in hoofdstuk 7. Beide experimenten werden oorspronkelijk ontworpen met het idee om samples in het gelokaliseerde regime te analyzeren.

In hoofdstuk 4, wordt de intensiteitsverdeling van elektromagnetische golven in een polaire keten van bijna-resonante, zwak-gekoppelde verstrooiers theoretisch onderzocht en ondersteund door een numerieke analyse. Voor sommige eigenwaardes in het spectrum wordt kritisch schalingsgedrag ontdekt als gevolg van de Anderson overgang. Deze lokalisatie transitie (in een formeel eendimensionaal systeem) wordt toegeschreven aan de lange afstand dipool-dipool interactie. Deze interactie vervalt omgekeerd evenredig met de afstand voor polarisatie die loodrecht op de keten staat. Voor golven met een polarisatie parallel aan de keten, wordt aangetoond dat alle eigenmodes lokaliseren. Een vergelijking met de resultaten behaald met Hermitische machtsfunctie random bandmatrices en andere hybride modellen, wordt gepresenteerd. Deze vergelijking onthult de betekenis van het niet-Hermitisch zijn van het model en de periodieke modulatie van de koppeling.

De experimentele waarneming van sterke multifractale golffuncties in de buurt van de Anderson lokalisatie overgang in open drie-dimensionale elastische netwerken wordt beschreven in hoofdstuk 5. De experimentele observatie van lokalisatie in deze samples werd gerapporteerd in een voorafgaande publicatie. Onze hernieuwde blik op de metingen, toonde voor het eerst aan dat er experimentele aanwijzingen zijn dat golven in de buurt van de lokalisatiedrempel een multifractale structuur bezitten. Eveneens bevestigde onze observaties de niet-triviale symmetrie van de multifractale exponenten.

Bibliography

[1] E. Abrahams, P. W. Anderson, D. C. Licciardello, and T. V. Ramakrishnan, *Scaling theory of localization: absence of quantum diffusion in two dimensions*, Phys. Rev. Lett. **42**, 673 (1979) — p.3 and 30.

[2] V. M. Agranovich and V. E. Kravtsov, *Nonlinear backscattering from opaque media*, Phys. Rev. B **43**, 13691 (1991) — p.20.

[3] A. Altland and M. R. Zirnbauer, *Nonstandard symmetry classes in mesoscopic normal-superconducting hybrid structures*, Phys. Rev. B **55**, 1142 (1997) — p.29.

[4] B. L. Al'tshuler, V. E. Kravtsov, and I. V. Lerner, *Statistics of mesoscopic fluctuations and instability of one-parameter scaling*, JETP **64**, 1352 (1986) — p.37.

[5] B. L. Al'tshuler and L. S. Levitov, *Weak chaos in a quantum Kepler problem*, Phys. Rep. **288**, 487 (1997) — p.30.

[6] A. Alù and N. Engheta, *Theory of linear chains of metamaterial: Plasmonic particles as subdiffraction optical nanotransmission lines*, Phys. Rev. B **74**, 205436 (2006) — p.31 and 43.

[7] P. W. Anderson, *Absence of diffusion in certain random lattices*, Phys. Rev. **109**, 1492 (1958) — p.3 and 30.

[8] P. W. Anderson, *Thoughts on localization*, Int. J. Mod. Phys. B **24**, 1501 (2010) — p.3 and 5.

[9] W. R. Anderson, J. R. Veale, and T. F. Gallagher, *Resonant dipole-dipole energy transfer in a nearly frozen Rydberg gas*, Phys. Rev. Lett. **80**, 249 (1998) — p.31.

[10] H. Aoki, *Critical behaviour of extended states in disordered systems*, J. Phys. C: Solid State Phys. **16**, L205 (1983) — p.36 and 37.

[11] A. Aspect and M. Inguscio, *Anderson localization of ultracold atoms*, Physics Today **62**, 30 (2009) — p.3 and 43.

[12] M. Baudrier-Raybaut, R. Haidar, P. Kupecek, P. Lemasson, and E. Rosencher, *Random quasi-phase-matching in bulk polycrystalline isotropic nonlinear materials*, Nature **432**, 374 (2004) — p.20.

[13] C. W. J. Beenakker, *Random-matrix theory course, Delta Institute for Theoretical Physics, Leiden.*, http://ilorentz.org/RMT/ — p.25.

[14] C. W. J. Beenakker, *Random-matrix theory of quantum transport*, Rev. Mod. Phys. **69**, 731 (1997) — p.34.

[15] C. W. J. Beenakker, *Thermal radiation and amplified spontaneous emission from a random medium*, Phys. Rev. Lett. **81**, 1829 (1998) — p.26.

[16] C. W. J. Beenakker and B. Rejaei, *Nonlogarithmic repulsion of transmission eigenvalues in a disordered wire*, Phys. Rev. Lett. **71**, 3689 (1993) — p.35.

[17] J. Beermann and S. I. Bozhevolnyi, *Microscopy of localized second-harmonic enhancement in random metal nanostructures*, Phys. Rev. B **69**, 155429 (2004) — p.20.

[18] G. Bergmann, *Quantitative analysis of weak localization in thin Mg films by magnetoresistance measurements*, Phys. Rev. B **25**, 2937 (1982) — p.68.

[19] J. Bertolotti, S. Gottardo, D. S. Wiersma, M. Ghulinyan, and L. Pavesi, *Optical necklace states in anderson localized 1d systems*, Phys. Rev. Lett. **94**, 113903 (2005) — p.51.

[20] M. D. Birowosuto, S. E. Skipetrov, W. L. Vos, and A. P. Mosk, *Observation of spatial fluctuations of the local density of states in random photonic media*, Phys. Rev. Lett. **105**, 013904 (2010) — p.19 and 79.

[21] E. Bogomolny and O. Giraud, *Eigenfunction entropy and spectral compressibility for critical random matrix ensembles*, Phys. Rev. Lett. **106**, 044101 (2011) — p.29.

[22] D. C. F. Bohren and D. R. Huffman, *Absorption and scattering of light by small particles* — p.74 and 75.

[23] K. Busch and C. M. Soukoulis, *Transport properties of random media: a new effective medium theory*, Phys. Rev. Lett. **75**, 3442 (1995) — p.74 and 75.

[24] W. Cai, B. B. Das, F. Liu, M. Zevallos, M. Lax, and R. R. Alfano, *Time-resolved optical diffusion tomographic image reconstruction in highly scattering turbid media*, PNAS **93**, 13561 (1996) — p.67.

[25] P. J. Campagnola and L. M. Loew, *Second-harmonic imaging microscopy for visualizing biomolecular arrays in cells, tissues and organisms*, Nat. Biotech. **21**, 1356 (2003) — p.21.

[26] C. Castellani and L. Peliti, *Multifractal wavefunction at the localisation threshold*, J. Phys. A: Math. and Gen. **19**, 429 (1986) — p.37.

[27] A. Cazè, R. Pierrat, and R. Carminati, *Near-field interactions and nonuniversality in speckle patterns produced by a point source in a disordered medium*, Phys. Rev. A **82**, 043823 (2010) — p.3 and 19.

[28] A. A. Chabanov, M. Stoytchev, and A. Z. Genack, *Statistical signatures of photon localization*, Nature **404**, 850 (2000) — p.35.

[29] A. A. Chabanov, N. P. Trégourès, B. A. van Tiggelen, and A. Z. Genack, *Mesoscopic correlation with polarization rotation of electromagnetic waves*, Phys. Rev. Lett. **92**, 173901 (2004) — p.16 and 19.

[30] J. Chabe, G. Lemarie, B. Gremaud, D. Delande, P. Szriftgiser, and J. C. Garreau, *Experimental observation of the Anderson metal-insulator transition with atomic matter waves*, Phys. Rev. Lett. **101**, 255702 (2008) — p.3 and 61.

[31] A. Chhabra and R. V. Jensen, *Direct determination of the $f(\alpha)$ singularity spectrum*, Phys. Rev. Lett. **62**, 1327 (1989) — p.57 and 64.

[32] E. Cuevas and V. E. Kravtsov, *Two-eigenfunction correlation in a multifractal metal and insulator*, Phys. Rev. B **76**, 235119 (2007) — p.23, 37, 66, and 77.

[33] A. G. Curto, G. Volpe, T. H. Taminiau, M. P. Kreuzer, R. Quidant, and N. F. van Hulst, *Unidirectional emission of a quantum dot coupled to a nanoantenna*, Science **329**, 930 (2010) — p.43.

[34] J. F. de Boer, A. Lagendijk, R. Sprik, and S. Feng, *Transmission and reflection correlations of second harmonic waves in nonlinear random media*, Phys. Rev. Lett. **71**, 3947 (1993) — p.20.

[35] F. A. B. F. de Moura and M. L. Lyra, *Delocalization in the 1d Anderson model with long-range correlated disorder*, Phys. Rev. Lett. **81**, 3735 (1998) — p.65.

[36] P. de Vries, D. V. van Coevorden, and A. Lagendijk, *Point scatterers for classical waves*, Rev. Mod. Phys. **70**, 447 (1998) — p.3, 12, and 46.

[37] O. N. Dorokhov, *Transmission coefficient and the localization length of an electron in N bound disordered chains*, JETP Lett. **36**, 318 (1982) — p.34.

[38] B. Duplantier and A. W. W. Ludwig, *Multifractals, operator-product expansion, and field theory*, Phys. Rev. Lett. **66**, 247 (1991) — p.37.

[39] B. Edlen, *The Refractive Index of Air*, Metrologia **2**, 71 (1966) — p.72.

[40] K. Efetov, *Supersymmetry in disorder and chaos* (Cambridge University Press, 1999) — p.34.

[41] K. B. Efetov, *Supersymmetry and theory of disordered metals*, Adv. Phys. **32**, 53 (1983) — p.5 and 29.

[42] R. G. S. El-Dardiry, S. Faez, and A. Lagendijk, *Classification of light sources and their interaction with active and passive environments*, Phys. Rev. A **83**, 031801 (2011) — p.19.

[43] F. Evers and A. D. Mirlin, *Anderson transitions*, Rev. Mod. Phys. **80**, 1355 (2008) — p.5, 36, 43, 47, 61, and 63.

[44] S. Faez, P. M. Johnson, and A. Lagendijk, *Varying the Effective Refractive Index to Measure Optical Transport in Random Media*, Phys. Rev. Lett. **103**, 053903 (2009) — p.67.

[45] S. Faez, P. M. Johnson, D. A. Mazurenko, and A. Lagendijk, *Experimental observation of second-harmonic generation and diffusion inside random media*, J. Opt. Soc. Am. B: Opt. Phys. **26**, 235 (2009) — p.20.

[46] S. Faez, A. Lagendijk, and A. Ossipov, *Critical scaling of polarization waves on a heterogeneous chain of resonators*, Phys. Rev. B **83**, 075121 (2011) — p.43.

[47] S. Faez, A. Strybulevych, J. H. Page, A. Lagendijk, and B. A. van Tiggelen, *Observation of multifractality in anderson localization of ultrasound*, Phys. Rev. Lett. **103**, 155703 (2009) — p.5, 41, 58, and 61.

[48] V. I. Falko and K. B. Efetov, *Statistics of prelocalized states in disordered conductors*, Phys. Rev. B **52**, 17413 (1995) — p.37.

[49] S. Feng, C. Kane, P. A. Lee, and A. D. Stone, *Correlations and fluctuations of coherent wave transmission through disordered media*, Phys. Rev. Lett. **61**, 834 (1988) — p.15, 18, and 67.

[50] M. Flrsheimer, C. Brillert, and H. Fuchs, *Chemical imaging of interfaces by sum frequency microscopy*, Langmuir **15**, 5437 (1999) — p.77.

[51] C. Forestiere, G. Miano, G. Rubinacci, and L. D. Negro, *Role of aperiodic order in the spectral, localization, and scaling properties of plasmon modes for the design of nanoparticle arrays*, Phys. Rev. B **79**, 085404 (2009) — p.44.

[52] I. Freund and R. Berkovits, *Surface reflections and optical transport through random media: Coherent backscattering, optical memory effect, frequency, and dynamical correlations*, Phys. Rev. B **41**, 496 (1990) — p.16.

[53] Y. V. Fyodorov, A. Ossipov, and A. Rodriguez, *The Anderson localization transition and eigenfunction multifractality in an ensemble of ultrametric random matrices*, J. Stat. Mech: Theory Exp. **2009**, L12001 (2009) — p.30 and 48.

[54] N. Garcia and A. Z. Genack, *Crossover to strong intensity correlation for microwave radiation in random media*, Phys. Rev. Lett. **63**, 1678 (1989) — p.16.

[55] A. Z. Genack, *Optical transmission in disordered media*, Phys. Rev. Lett. **58**, 2043 (1987) — p.67 and 68.

[56] A. Z. Genack and J. M. Drake, *Relationship between Optical Intensity, Fluctuations and Pulse Propagation in Random Media*, Europhys. Lett. **11**, 331 (1990) — p.71.

[57] A. P. Gibson, J. C. Hebden, and S. R. Arridge, *Recent advances in diffuse optical imaging*, Phys. Med. Biol. **50**, R1 (2005) — p.68.

[58] A. Goetschy and S. E. Skipetrov, *Non-Hermitian Euclidean random matrix theory*, arXiv:1102.1850 (2011) — p.31.

[59] W. Götze, *A theory for the conductivity of a fermion gas moving in a strong three-dimensional random potential*, Journal of Physics C: Solid State Physics **12**, 1279 (1979) — p.3.

[60] H. Grussbach and M. Schreiber, *Determination of the mobility edge in the Anderson model of localization in three dimensions by multifractal analysis*, Phys. Rev. B **51**, 663 (1995) — p.61.

[61] A. Hartsuiker and W. L. Vos, *Structural Properties of Opals Grown with Vertical Controlled Drying*, Langmuir **24**, 4670 (2008) — p.70 and 74.

[62] N. Hatano and D. R. Nelson, *Localization transitions in non-Hermitian quantum mechanics*, Phys. Rev. Lett. **77**, 570 (1996) — p.29.

[63] A. Heiderich, R. Maynard, and B. A. van Tiggelen, *Coherent backscattering in non-linear media*, Opt. Commun. **115**, 392 (1995) — p.20.

[64] H. Hu, A. Strybulevych, J. H. Page, S. E. Skipetrov, and B. A. van Tiggelen, *Localization of ultrasound in a three-dimensional elastic network*, Nat. Phys. **4**, 945 (2008) — p.4, 5, 7, 61, and 62.

[65] T. Ito and M. Tomita, *Speckle correlation measurement in a disordered medium observed through second-harmonics generation*, Phys. Rev. E **69**, 036610 (2004) — p.20, 79, and 85.

[66] S. John, *Localization of Light*, Physics Today **44**, 32 (1991) — p.4.

[67] P. M. Johnson, A. Imhof, B. P. J. Bret, J. G. Rivas, and A. Lagendijk, *Time-resolved pulse propagation in a strongly scattering material*, Phys. Rev. E **68**, 016604 (2003) — p.72.

[68] D. E. K. K. B. Efetov, A. I. Larkin, *Interaction of diffusion modes in the theory of localization*, Sov. Phys. JETP **52**, 568 (1980) — p.3.

[69] B. C. Kaas, B. A. van Tiggelen, and A. Lagendijk, *Anisotropy and interference in wave transport: an analytic theory*, Phys. Rev. Lett. **100**, 123902 (2008) — p.10.

[70] A. F. Koenderink and A. Polman, *Complex response and polariton-like dispersion splitting in periodic metal nanoparticle chains*, Phys. Rev. B **74**, 033402 (2006) — p.3, 31, 44, and 49.

[71] V. Krachmalnicoff, E. Castanié, Y. De Wilde, and R. Carminati, *Fluctuations of the local density of states probe localized surface plasmons on disordered metal films*, Phys. Rev. Lett. **105**, 183901 (2010) — p.19 and 48.

[72] B. Kramer, A. MacKinnon, T. Ohtsuki, and K. Slevin, *Finite size scaling analysis of the anderson transition*, Int. J. Mod. Phys. B **24**, 1841 (2010) — p.29.

[73] V. E. Kravtsov, V. M. Agranovich, and K. I. Grigorishin, *Theory of second-harmonic generation in strongly scattering media*, Phys. Rev. B **44**, 4931 (1991) — p.19 and 78.

[74] V. E. Kravtsov, A. Ossipov, O. M. Yevtushenko, and E. Cuevas, *Dynamical scaling for critical states: Validity of Chalker's ansatz for strong fractality*, Phys. Rev. B **82**, 161102 (2010) — p.30.

[75] A. Lagendijk, *private communication* — p.16.

[76] A. Lagendijk, B. van Tiggelen, and D. S. Wiersma, *Fifty years of Anderson localization*, Physics Today **62**, 24 (2009) — p.3 and 43.

[77] E. Larose, J. de Rosny, L. Margerin, D. Anache, P. Gouedard, M. Campillo, and B. van Tiggelen, *Observation of multiple scattering of kHz vibrations in a concrete structure and application to monitoring weak changes*, Phys. Rev. E **73**, 016609 (2006) — p.68 and 76.

[78] G. Lemarié, H. Lignier, D. Delande, P. Szriftgiser, and J. C. Garreau, *Critical state of the anderson transition: between a metal and an insulator*, Phys. Rev. Lett. **105**, 090601 (2010) — p.3 and 4.

[79] L. S. Levitov, *Absence of localization of vibrational modes due to dipole-dipole interaction*, Europhys. Lett. **9**, 83 (1989) — p.30.

[80] O. I. Lobkis and R. L. Weaver, *Coda-wave interferometry in finite solids: recovery of p-to-s conversion rates in an elastodynamic billiard*, Phys. Rev. Lett. **90**, 254302 (2003) — p.68 and 76.

[81] J. J. Ludlam, S. N. Taraskin, and S. R. Elliott, *Disorder-induced vibrational localization*, Phys. Rev. B **67**, 132203 (2003) — p.65.

[82] A. MacKinnon and B. Kramer, *One-parameter scaling of localization length and conductance in disordered systems*, Phys. Rev. Lett. **47**, 1546 (1981) — p.3.

[83] E. V. Makeev and S. E. Skipetrov, *Second-harmonic generation in suspensions of spherical particles*, Opt. Commun. **224**, 139 (2003) — p.19, 22, and 78.

[84] A. G. Mal'shukov and G. D. Mahan, *Nonlinear forward scattering of light in opaque media*, Phys. Rev. B **57**, 7701 (1998) — p.20.

[85] G. Maret and P. E. Wolf, *Multiple light scattering from disordered media. The effect of brownian motion of scatterers*, Z. Phys. B **65**, 409 (1987) — p.17, 68, and 76.

[86] V. A. Markel, *Anderson localization of polar eigenmodes in random planar composites*, J. Phys. Cond. Matt. **18**, 11149 (2006) — p.44.

[87] V. A. Markel and A. K. Sarychev, *Propagation of surface plasmons in ordered and disordered chains of metal nanospheres*, Phys. Rev. B **75**, 085426 (2007) — p.44.

[88] M. L. Mehta, *Random matrices* (Academic Press, 2004) — p.26.

[89] P. A. Mello, P. Pereyra, and N. Kumar, *Macroscopic approach to multichannel disordered conductors*, Ann. Phys. **181**, 290 (1988) — p.34.

[90] V. Melnikov, L. Golovan, S. Konorov, D. Muzychenko, A. Fedotov, A. Zheltikov, V. Timoshenko, and P. Kashkarov, *Second-harmonic generation in strongly scattering porous gallium phosphide*, Appl. Phys. B **79**, 225 (2004) — p.20.

[91] A. Mildenberger and F. Evers, *Wave function statistics at the symplectic two-dimensional Anderson transition: Bulk properties*, Phys. Rev. B **75**, 041303 (2007) — p.61.

[92] A. D. Mirlin, *Statistics of energy levels and eigenfunctions in disordered systems*, Phys. Rep. **326**, 259 (2000) — p.34.

[93] A. D. Mirlin, Y. V. Fyodorov, F. Dittes, J. Quezada, and T. H. Seligman, *Transition from localized to extended eigenstates in the ensemble of power-law random banded matrices*, Phys. Rev. E **54**, 3221 (1996) — p.30.

[94] A. D. Mirlin, Y. V. Fyodorov, A. Mildenberger, and F. Evers, *Exact relations between multifractal exponents at the Anderson transition*, Phys. Rev. Lett. **97**, 046803 (2006) — p.37, 56, 58, 61, and 63.

[95] C. Monthus and T. Garel, *Anderson localization of phonons in dimension $d = 1, 2, 3$*

: Finite-size properties of the inverse participation ratios of eigenstates, Phys. Rev. B **81**, 224208 (2010) — p.65.

[96] C. Monthus and T. Garel, *A critical Dyson hierarchical model for the Anderson localization transition*, arXiv:1102.4701 (2011) — p.30.

[97] M. Morgenstern, J. Klijn, C. Meyer, and R. Wiesendanger, *Real-space observation of drift states in a two-dimensional electron system at high magnetic fields*, Phys. Rev. Lett. **90**, 056804 (2003) — p.61.

[98] C. Mudry, C. Chamon, and X.-G. Wen, *Two-dimensional conformal field theory for disordered systems at criticality*, Nucl. Phys. B **466**, 383 (1996) — p.37.

[99] O. L. Muskens and A. Lagendijk, *Broadband enhanced backscattering spectroscopy of strongly scatteringmedia*, Opt. Express **16**, 1222 (2008) — p.70 and 83.

[100] O. L. Muskens, J. G. Rivas, R. E. Algra, E. P. A. M. Bakkers, and A. Lagendijk, *Design of Light Scattering in Nanowire Materials for Photovoltaic Applications*, Nano Lett. **8**, 2638 (2008) — p.68.

[101] R. Oppermann and F. Wegner, *Disordered system withn orbitals per site: 1/n expansion*, Z. Phys. B **34**, 327 (1979) — p.3 and 30.

[102] F. J. P., Schuurmans, D. Vanmaekelbergh, J. van de Lagemaat, and A. Lagendijk, *Strongly photonic macroporous gallium phosphide networks*, Science **284**, 141 (1999) — p.82.

[103] J. B. Pendry, *Quasi-extended electron states in strongly disordered systems*, J. Phys. C: Solid State Phys. **20**, 733 (1987) — p.51.

[104] D. J. Pine, D. A. Weitz, P. M. Chaikin, and E. Herbolzheimer, *Diffusing wave spectroscopy*, Phys. Rev. Lett. **60**, 1134 (1988) — p.17, 68, and 76.

[105] A. Polman, *Plasmonics applied*, Science **322**, 868 (2008) — p.43.

[106] A. Richardella, P. Roushan, S. Mack, B. Zhou, D. A. Huse, D. D. Awschalom, and A. Yazdani, *Visualizing critical correlations near the metal-insulator transition in* $Ga_{1-x}Mn_xAs$, Science **327**, 665 (2010) — p.5, 58, and 62.

[107] A. Rodriguez, L. J. Vasquez, and R. A. Römer, *Multifractal analysis with the probability density function at the three-dimensional Anderson transition*, Phys. Rev. Lett. **102**, 106406 (2009) — p.48, 52, 62, and 65.

[108] A. Rodriguez, L. J. Vasquez, K. Slevin, and R. A. Römer, *Critical parameters from a generalized multifractal analysis at the Anderson transition*, Phys. Rev. Lett. **105**, 046403 (2010) — p.48 and 52.

[109] F. Scheffold and G. Maret, *Universal conductance fluctuations of light*, Phys. Rev. Lett. **81**, 5800 (1998) — p.16.

[110] A. P. Schnyder, S. Ryu, A. Furusaki, and A. W. W. Ludwig, *Classification of topological insulators and superconductors in three spatial dimensions*, Phys. Rev. B **78**, 195125 (2008) — p.29.

[111] G. Schubert, J. Schleede, K. Byczuk, H. Fehske, and D. Vollhardt, *Distribution of the local density of states as a criterion for Anderson localization: Numerically exact results for various lattices in two and three dimensions*, Phys. Rev. B **81**, 155106 (2010) — p.52.

[112] B. Shapiro, *Large intensity fluctuations for wave propagation in random media*, Phys. Rev. Lett. **57**, 2168 (1986) — p.24.

[113] B. Shapiro, *New type of intensity correlation in random media*, Phys. Rev. Lett. **83**, 4733 (1999) — p.18 and 23.

[114] Y. R. Shen, *Surface properties probed by second-harmonic and sum-frequency gener-*

ation, Nature **337**, 519 (1989) — p.77.

[115] P. Sheng, *Scattering and localization of classical waves in random media* (World Scientific, 1990) — p.16.

[116] P. Sheng, *Introduction to wave Scattering, localization and mesoscopic phenomena* (Academic Press, 1995) — p.15.

[117] P. Sheng and Z. Zhang, *Scalar-wave localization in a two-component composite*, Phys. Rev. Lett. **57**, 1879 (1986) — p.74.

[118] S. E. Skipetrov and A. Goetschy, *Eigenvalue distributions of large Euclidean random matrices for waves in random media*, J. Phys. A: Math. and Theor. **44**, 065102 (2011) — p.31.

[119] S. E. Skipetrov and R. Maynard, *Nonuniversal correlations in multiple scattering*, Phys. Rev. B **62**, 886 (2000) — p.16 and 24.

[120] D. R. Smith, J. B. Pendry, and M. C. K. Wiltshire, *Metamaterials and Negative Refractive Index*, Science **305**, 788 (2004) — p.68.

[121] R. Snieder and J. H. Page, *Multiple Scattering in Evolving Media*, Physics Today **60**, 49 (2007) — p.68 and 76.

[122] M. I. Stockman, *Giant fluctuations of second harmonic generation on nanostructured surfaces*, Chem. Phys. **318**, 156 (2005) — p.77.

[123] M. I. Stockman, *Nanoplasmonics: The physics behind the applications*, Physics Today **64**, 39 (2011) — p.31.

[124] M. I. Stockman, D. J. Bergman, C. Anceau, S. Brasselet, and J. Zyss, *Enhanced second-harmonic generation by metal surfaces with nanoscale roughness: nanoscale dephasing, depolarization, and correlations*, Phys. Rev. Lett. **92**, 057402 (2004) — p.20.

[125] M. I. Stockman, S. V. Faleev, and D. J. Bergman, *Localization versus delocalization of surface plasmons in nanosystems: Can one state have both characteristics?*, Phys. Rev. Lett. **87**, 167401 (2001) — p.51.

[126] A. R. Subramaniam, I. A. Gruzberg, A. W. W. Ludwig, F. Evers, A. Mildenberger, and A. D. Mirlin, *Surface criticality and multifractality at localization transitions*, Phys. Rev. Lett. **96**, 126802 (2006) — p.37.

[127] T. Terao, T. Nakayama, and H. Aoki, *Multifractality of the quantum Hall wave functions in higher Landau levels*, Phys. Rev. B **54**, 10350 (1996) — p.65.

[128] I. M. Tiginyanu, I. V. Kravetsky, J. Monecke, W. Cordts, G. Marowsky, and H. L. Hartnagel, *Semiconductor sieves as nonlinear optical materials*, Appl. Phys. Lett. **77**, 2415 (2000) — p.20.

[129] M. P. van Albada, J. F. de Boer, and A. Lagendijk, *Observation of long-range intensity correlation in the transport of coherent light through a random medium*, Phys. Rev. Lett. **64**, 2787 (1990) — p.16.

[130] B. van den Broek, T. H. Oosterkamp, and J. van Noort, *A multifocal two-photon microscopy setup for parallel 3d tracking of gold nanorods*, Biophys. J. **98**, 178a (2010) — p.21.

[131] E. van Putten, *The information age in optics: Measuring the transmission matrix*, Physics **3**, 22 (2010) — p.26.

[132] M. C. W. van Rossum and T. M. Nieuwenhuizen, *Multiple scattering of classical waves: microscopy, mesoscopy, and diffusion*, Rev. Mod. Phys. **71**, 313 (1999) — p.15 and 16.

[133] B. A. van Tiggelen and S. E. Skipetrov, *Fluctuations of local density of states and*

C_0 *speckle correlations are equal*, Phys. Rev. E **73**, 045601 (2006) — p.19.

[134] L. J. Vasquez, A. Rodriguez, and R. A. Römer, *Multifractal analysis of the metal-insulator transition in the three-dimensional Anderson model. I. Symmetry relation under typical averaging*, Phys. Rev. B **78**, 195106 (2008) — p.48.

[135] I. M. Vellekoop, *Controlling the propagation of light in disordered scattering media*, http://doc.utwente.nl/58928/ (2008), Doctoral thesis — p.26.

[136] I. M. Vellekoop and A. P. Mosk, *Universal optimal transmission of light through disordered materials*, Phys. Rev. Lett. **101**, 120601 (2008) — p.5 and 34.

[137] R. Vincent and R. Carminati, *Magneto-optical control of Förster energy transfer*, Phys. Rev. B **83**, 165426 (2011) — p.2.

[138] D. Vollhardt and P. Wölfle, *Diagrammatic, self-consistent treatment of the Anderson localization problem in* $d \leq 2$ *dimensions*, Phys. Rev. B **22**, 4666 (1980) — p.3.

[139] W. Wan, Y. Chong, L. Ge, H. Noh, A. D. Stone, and H. Cao, *Time-reversed lasing and interferometric control of absorption*, Science **331**, 889 (2011) — p.2.

[140] J. Wang and A. Z. Genack, *Transport through modes in random media*, Nature **471**, 345 (2011) — p.5.

[141] W. H. Weber and G. W. Ford, *Propagation of optical excitations by dipolar interactions in metal nanoparticle chains*, Phys. Rev. B **70**, 125429 (2004) — p.31, 44, and 49.

[142] F. Wegner, *Inverse participation ratio in 2+e dimensions*, Z. Phys. B **36**, 209 (1980) — p.5, 36, and 37.

[143] T. Wellens, B. Grmaud, D. Delande, and C. Miniatura, *Coherent backscattering of light by nonlinear scatterers*, Phys. Rev. E **71**, 055603 (2005) — p.20.

[144] I. M. White and X. Fan, *On the performance quantification of resonant refractive index sensors*, Opt. Express **16**, 1020 (2008) — p.71 and 76.

[145] E. P. Wigner, *On the distribution of the roots of certain symmetric matrices*, The Annals of Mathematics **67**, 325 (1958) — p.26.

[146] E. P. Wigner, *Random Matrices in Physics*, SIAM Review **9**, 1 (1967) — p.26.

[147] N. Yang, W. E. Angerer, and A. G. Yodh, *Angle-resolved second-harmonic light scattering from colloidal particles*, Phys. Rev. Lett. **87**, 103902 (2001) — p.20.

[148] P. Zijlstra, J. W. M. Chon, and M. Gu, *Five-dimensional optical recording mediated by surface plasmons in gold nanorods*, Nature **459**, 410 (2009) — p.21.

[149] M. R. Zirnbauer, *Riemannian symmetric superspaces and their origin in random-matrix theory*, J. Math. Phys. **37**, 4986 (1996) — p.29.